



Paula Kozlowski Pitombeira Reis

**Development and applications of a
compositional pore-network model for
gas-condensate flow**

Tese de Doutorado

Thesis presented to the Programa de Pós-graduação em Engenharia Mecânica, do Departamento de Engenharia Mecânica da PUC-Rio in partial fulfillment of the requirements for the degree of Doutor em Engenharia Mecânica.

Advisor: Prof. Marcio da Silveira Carvalho

Rio de Janeiro
May 2021



Paula Kozlowski Pitombeira Reis

**Development and applications of a
compositional pore-network model for
gas-condensate flow**

Thesis presented to the Programa de Pós-graduação em Engenharia Mecânica da PUC-Rio in partial fulfillment of the requirements for the degree of Doutor em Engenharia Mecânica. Approved by the Examination Committee:

Prof. Marcio da Silveira Carvalho

Advisor

Departamento de Engenharia Mecânica – PUC-Rio

Prof. Frederico Wanderley Tavares

UFRJ

Prof. Ian Gates

Universidade de Calgary

Prof. Marcio Arab Murad

Laboratório Nacional de Computação Científica

Dr. Marcos Vitor Barbosa Machado

Petrobras

Rio de Janeiro, May the 4th, 2021

All rights reserved.

Paula Kozlowski Pitombeira Reis

Paula Reis received a bachelor's degree in Petroleum Engineering from the Federal University of Rio de Janeiro, in 2013, and a master's degree in Ocean Engineering from the same university, in 2014. Currently she works as a researcher at the Laboratory of Microhydrodynamics and Flow in Porous Media at PUC-Rio, while pursuing a PhD degree at the same institution, in the Mechanical Engineering Department.

Bibliographic data

Reis, Paula

Development and applications of a compositional pore-network model for gas-condensate flow / Paula Kozlowski Pitombeira Reis; advisor: Marcio da Silveira Carvalho. – 2021.

145 f: il. color. ; 30 cm

Tese (doutorado) - Pontifícia Universidade Católica do Rio de Janeiro, Departamento de Engenharia Mecânica, 2021.

Inclui bibliografia

1. Engenharia Mecânica – Teses. 2. Reservatórios de gás retrógrado;. 3. Modelo de rede de poros;. 4. Modelagem em escala de poro;. 5. Modelagem composicional.. I. Carvalho, Marcio. II. Pontifícia Universidade Católica do Rio de Janeiro. Departamento de Engenharia Mecânica. III. Título.

CDD: 621

I dedicate this thesis to everyone who, directly or indirectly, contributed to its completion.

Acknowledgments

To Leonardo Malouf, for driving me forward through the most genuine belief in my competence.

To my advisor, Prof. Marcio Carvalho, for the trust, excellent technical guidance, and inspiration to pursue an academic career.

To my friends and family for the overall support during the, sometimes arduous, path to conclude this work.

To PUC-Rio and to Repsol-Sinopec Brasil for the funding without which this research could not be accomplished.

This study was financed in part by the Coordenação de Aperfeiçoamento de Pessoal de Nível Superior - Brasil (CAPES) - Finance Code 001.

Abstract

Reis, Paula; Carvalho, Marcio (Advisor). **Development and applications of a compositional pore-network model for gas-condensate flow**. Rio de Janeiro, 2021. 145p. Tese de Doutorado – Departamento de Engenharia Mecânica, Pontifícia Universidade Católica do Rio de Janeiro.

Liquid dropout and accumulation in gas-condensate reservoirs, especially in the near wellbore region, hinder gas flow and affect negatively the produced fluid composition. Yet, condensate banking forecasting is commonly inaccurate, as experiments seldom reproduce reservoir extreme conditions and complex fluid composition, while most pore-scale models oversimplify the physical phenomena associated with phase transitions between gas and condensate. To address this gap, a fully implicit isothermal compositional pore-network model for gas and condensate flow is presented. The proposed pore-networks consist of 3D structures of constricted circular capillaries. Condensation modes and flow patterns are attributed to the capillaries according to the medium's wettability, local saturations and influence of viscous and capillary forces. At the network nodes, pressure and molar contents are determined via the coupled solution of molar balance and volume consistency equations. Concomitantly, a PT-flash based on the Peng-Robinson equation of state is performed for each node, updating the local phases saturations and compositions. For the proposed model validation, flow analyses were carried out based on coreflooding experiments reported in the literature, with matching fluid composition and flow conditions, and approximated pore-space geometry. Predicted and measured relative permeability curves showed good quantitative agreement, for two values of interfacial tension and three values of gas flow velocity. Following the validation, the model was used to evaluate wettability alteration and gas injection as prospect enhanced recovery methods for gas-condensate reservoirs. Results exhibited similar trends observed in coreflooding experiments and conditions for optimal flow enhancement were identified.

Keywords

Gas-condensate reservoirs;; Pore-network model;; Pore-scale modeling;; Compositional modeling.

Resumo

Reis, Paula; Carvalho, Marcio. **Desenvolvimento e aplicações de um modelo de rede de poros para o escoamento de gás e condensado**. Rio de Janeiro, 2021. 145p. Tese de Doutorado – Departamento de Engenharia Mecânica, Pontifícia Universidade Católica do Rio de Janeiro.

A formação e o acúmulo de condensado em reservatórios de gás retrógrado, especialmente na vizinhança de poços de produção, obstruem parcialmente o fluxo de gás e afetam negativamente a composição dos fluidos produzidos. Entretanto, a previsão de bloqueio por condensado é comumente imprecisa, visto que experimentos raramente reproduzem as condições extremas e composições complexas dos fluidos dos reservatórios, enquanto a maioria dos modelos em escala de poros simplificam demasiadamente os fenômenos físicos associados à transição de fases entre gás e condensado. Para corrigir essa lacuna, um modelo de rede de poros isotérmico composicional e totalmente implícito é apresentado. As redes de poros propostas consistem em estruturas tridimensionais de capilares constritos circulares. Modos de condensação e padrões de escoamento são atribuídos aos capilares de acordo com a molhabilidade do meio, as saturações locais e a influência de forças viscosas e capilares. Nos nós da rede, pressão e conteúdo molar são determinados através da solução acoplada de equações de balanço molar e consistência de volumes. Concomitantemente, um cálculo de *flash* à pressão e à temperatura constantes, baseado na equação de estado de Peng e Robinson, é realizado em cada nó, atualizando as saturações e composições das fases. Para a validação do modelo proposto, análises de escoamento foram executadas baseadas em experimentos de escoamento em testemunho reportados na literatura, usando composição dos fluidos e condições de escoamento correspondentes, e geometria do meio poroso aproximada. Curvas de permeabilidade relativa medidas nos experimentos e previstas pelo modelo mostraram boa concordância quantitativa, para dois valores de tensão interfacial e três valores de velocidade de escoamento de gás. Após a validação, o modelo foi usado para avaliar alteração de molhabilidade e injeção de gás como possíveis métodos de recuperação avançada para reservatórios de gás retrógrado. Os resultados exibiram tendências similares àquelas observadas em experimentos de escoamento em testemunhos, e condições ótimas para melhoramento do escoamento foram identificadas.

Palavras-chave

Reservatórios de gás retrógrado;; Modelo de rede de poros;; Modelagem em escala de poro;; Modelagem composicional..

Table of contents

1	Introduction	15
1.1	Objective	16
1.2	Chapters overview	16
2	Gas-condensate reservoirs	18
2.1	Petroleum reservoir fluids characterization	18
2.2	Gas-condensate fluids properties	19
2.2.1	Liquid dropout	20
2.2.2	Compositional differences between the phases	22
2.2.3	Viscosity and density	23
2.2.4	Interfacial tension	24
2.3	Gas-condensate flow in porous media	25
2.3.1	Condensation and flow visualization at the pore-scale	25
2.3.2	Macro-scale modeling of gas-condensate flow in porous media	28
2.3.3	Relative permeabilities	32
3	Pore-network modeling	39
3.1	Pore-scale modeling	39
3.2	Pore-network structure	40
3.2.1	Network topology	40
3.2.1.1	Synthetic networks	41
3.2.1.2	Image based networks	42
3.2.2	Pore body and throat geometry	42
3.2.2.1	Phase configuration in pores and throats	44
3.3	Pore-network modeling categories	46
3.3.1	Quasi-static	46
3.3.2	Dynamic	46
3.4	Pore-network modeling of gas-condensate flow	47
4	Proposed pore-network model	63
4.1	Model Assumptions	63
4.2	Pore-network description	63
4.3	Two-phase flow in capillaries	65
4.3.1	Flow Patterns Overview	65
4.3.2	Gas and Condensate Annular Flow Conductances	66
4.3.3	Capillary Blocking Conditions	67
4.4	Equations governing the flow	68
4.4.1	Molar Balance Equation	69
4.4.1.1	Functions H and H^{int}	69
4.4.2	Volume Consistency Equation	71
4.4.3	Boundary Conditions	71
4.4.4	Solution via Newton-Raphson Method	72
4.5	Phase equilibrium calculations	72
4.5.1	Flash calculation	73

4.5.2	Stability Test	76
5	Results	78
5.1	Pore-network model validation	78
5.1.1	Pore-network construction	79
5.1.2	Injected fluid	80
5.1.3	Flow conditions	81
5.1.4	Relative permeability curves	81
5.1.5	Visualization of blocked capillaries	85
5.1.6	Compositional shift during gas-condensate flow	86
5.1.7	Discussion	87
5.2	Pore-network model applications	88
5.2.1	Wettability alteration in gas-condensate reservoirs	88
5.2.1.1	Condensation and gas-liquid flow in gas-wet microchannels	90
5.2.1.2	Conductances for flow in gas-wet media	90
5.2.1.3	Pore-network description	92
5.2.1.4	Injected fluid	94
5.2.1.5	Flow conditions	95
5.2.1.6	Relative permeability curves	96
5.2.1.7	Improvement factor	99
5.2.1.8	Liquid accumulation and compositional shift	101
5.2.1.9	Discussion	102
5.2.2	Gas injection in gas-condensate reservoirs	103
5.2.2.1	Pore-network description	106
5.2.2.2	Injected fluids	106
5.2.2.3	Flow conditions	109
5.2.2.4	Condensate saturation reduction	110
5.2.2.5	Recovery of heavy components	121
5.2.2.6	Gas relative permeability improvement	124
5.2.2.7	Discussion	126
6	Conclusions	129
6.1	Pore-network model for gas-condensate flow	129
6.2	Pore-scale analysis of wettability alteration in gas-condensate reservoirs	130
6.3	Pore-scale analysis of gas injection in gas-condensate reservoirs	131
6.4	Future work	132
	Bibliography	133

List of figures

Figure 1.1	Phase diagram of a gas-condensate fluid	15
Figure 2.1	Petroleum reservoir fluid types. Adapted from [1]	18
Figure 2.2	Phase envelope the mixture presented in Table 2.1. In this figure, obtained with the CMG software Winprop, the saturation lines represent the volumetric fraction of the liquid or gaseous phases.	20
Figure 2.3	Liquid dropout of Mixture A at $80^{\circ}C$	21
Figure 2.4	Molar percentages of C_1 and C_7 in the gas and liquid phases of Mixture A	22
Figure 2.5	Viscosities of the gas and liquid phases of Mixture A, at $80^{\circ}C$	23
Figure 2.6	Densities of the gas and liquid phases of Mixture A, at $80^{\circ}C$	24
Figure 2.7	Interfacial tension between the phases of Mixture A, at $80^{\circ}C$	25
Figure 2.8	Condensation experiment in micromodel, conducted by Coşkuner [2]	26
Figure 2.9	Condensate bridges observed during gas-condensate flow in micromodel, conducted by Coşkuner [2]	27
Figure 2.10	Experiments of phase separation for wetting and non-wetting emerging phases, conducted by Dawe and Grattoni [3]	27
Figure 2.11	Points of cyclic condensate bridge opening and closing during the experiments performed by Jamiolahmady <i>et al.</i> [4]. Water is represented in dark gray, condensate in medium gray, gas in light gray and the porous medium grains in white.	28
Figure 2.12	Classification of reservoir zones according to condensate mobility and saturation	30
Figure 2.13	Relative permeability curves for gas and condensate in the absence of connate water.	31
Figure 3.1	Networks based on a regular cubic lattice.	41
Figure 3.2	Image based networks generated by Dong [5]	42
Figure 3.3	Pore body and pore throat geometries	43
Figure 3.4	Example of phases configuration in a water-wet triangular pore throat cross-section.	44
Figure 3.5	Example of phases configuration in a triangular pore throat cross-section, before and after wettability alteration from water to mixed-wet.	45
Figure 3.6	Bethe tree porous medium representation used by Mohammadi <i>et al.</i> [6]	48
Figure 3.7	Advancing and receding interfaces of a condensate bridge accommodated at a circular capillary. Adapted from Fang <i>et al.</i> [7]	49

Figure 3.8	Cubic pore bodies connected by converging-diverging pore throats with square cross-section used to represent porous media. Adapted from Wang and Mohanty[8]	50
Figure 3.9	Pore-throat connectivity in the sphere-pack model used by Wang and Mohanty[8]. The gray pore throat is connected by its corners to the pore throats depicted in black, plus eight pore throats in the planes outside the figure, indicated by the arrows.	51
Figure 3.10	Mechanisms of condensate droplet formation during low liquid saturation high capillary number flow, proposed by Wang and Mohanty[9]	53
Figure 3.11	Open and closed half cycles used to model the coupled flow of gas and condensate through pores, proposed by Jamio-lahmady <i>et al.</i> [4].	55
Figure 3.12	Sequence of condensation in a square vertical capillary, proposed by Bustos and Toledo [10]	58
Figure 3.13	Partition of capillary regions suggested by Bustos and Toledo [10] for conductance calculation	59
Figure 3.14	Control volumes used to calculate the variables in the model proposed by Santos and Carvalho [11]	62
Figure 4.1	Definition of nodes and edges in the proposed model	64
Figure 4.2	Converging-diverging capillary profile	64
Figure 4.3	Evolution of condensate configuration in a capillary	66
Figure 4.4	Condensate bridge radii, R_1 and R_2 , used to calculate ΔP_{crit}	68
Figure 5.1	Normalized probability distribution function for R_{min}	79
Figure 5.2	Aspect ratio of pore-networks extracted from a 3D image of a berea sandstone sample	80
Figure 5.3	k_{rg} and k_{rc} , at $\sigma = 0.037mN/m$ and $v_g = 18md^{-1}$	82
Figure 5.4	k_{rg} and k_{rc} , at $\sigma = 0.037mN/m$ and $v_g = 9md^{-1}$	83
Figure 5.5	k_{rg} and k_{rc} , at $\sigma = 0.037mN/m$ and $v_g = 36md^{-1}$	83
Figure 5.6	k_{rg} and k_{rc} , at $\sigma = 0.015mN/m$ and $v_g = 9md^{-1}$	84
Figure 5.7	k_{rg} and k_{rc} , at $\sigma = 0.015mN/m$ and $v_g = 18md^{-1}$	84
Figure 5.8	k_{rg} and k_{rc} , at $\sigma = 0.015mN/m$ and $v_g = 36md^{-1}$	84
Figure 5.9	Blocked Capillaries, at $\sigma = 0.037mN/m$ and $v_g = 18md^{-1}$	85
Figure 5.10	Phase Envelopes of C1-nC4 binary mixtures, obtained with the CMG software Winprop	87
Figure 5.11	Stages of condensation and flow in a gas-wet capillary	91
Figure 5.12	(a) Pore body and throat dimensions following the pore-network extraction method proposed by Dong [5]. (b) Pore throat dimensions for the adapted pore-network, based on pore body and throat radii in (a)	93
Figure 5.13	(a) Sandstone sample and micro-CT image used to extract the pore-network. Images available on [12]. (b) Pore-network generated with data extracted from the sandstone sample on(a), with used subsection delineated. Data available on [12].(c) Subsection of the pore-network in (b), adapted for the proposed model.	93

Figure 5.14 Histograms for the radii used in the adapted network. (a) R_{min} . (b) R_{max} .	94
Figure 5.15 Fluid mixture used during the wettability alteration analyses.	95
Figure 5.16 Relative permeability curves for $v_g = 7.5m/day$	96
Figure 5.17 Relative permeability curves for $v_g = 45m/day$	97
Figure 5.18 Relative permeability curves for $v_g = 150m/day$	97
Figure 5.19 Improvement factors for all tested flowing conditions	100
Figure 5.20 Phase envelope shift due to liquid accumulation	102
Figure 5.21 Fluid mixture phase envelope	107
Figure 5.22 Liquid dropout at 60°C, with 75% of the gas-condensate mixture and 25% of the injected gases, in moles	108
Figure 5.23 Liquid dropout at 60°C, with 50% of the gas-condensate mixture and 50% of the injected gases, in moles	108
Figure 5.24 Liquid dropout at 60°C, with 25% of the gas-condensate mixture and 75% of the injected gases, in moles	109
Figure 5.25 Condensate saturation during the injection of gases with 99% molar concentration, at P=22 MPa	111
Figure 5.26 Condensate saturation during the injection of gases with 99% molar concentration, at P=21.5 MPa	111
Figure 5.27 Condensate saturation during the injection at of gases with 99% molar concentration, P=21 MPa	111
Figure 5.28 Condensate saturation during the injection at of gases with 99% molar concentration, P=19.5 MPa	112
Figure 5.29 Condensate saturation during the injection at of gases with 99% molar concentration, P=17.75 MPa	112
Figure 5.30 Condensate saturation during the injection at of gases with 99% molar concentration, P=14.75 MPa	112
Figure 5.31 Molar content of C_1 in the pore-network after injection of the mixture containing 99% of C_1 .	114
Figure 5.32 Molar content of C_2 in the pore-network after injection of the mixture containing 99% of C_2 .	115
Figure 5.33 Molar content of CO_2 in the pore-network after injection of the mixture containing 99% of CO_2 .	116
Figure 5.34 Molar content of N_2 in the pore-network after injection of the mixture containing 99% of N_2 .	117
Figure 5.35 Condensate saturation during the injection of gases with 50% molar concentration, at P=22 MPa	117
Figure 5.36 Condensate saturation during the injection of gases with 50% molar concentration, at P=21.5 MPa	118
Figure 5.37 Condensate saturation during the injection at of gases with 50% molar concentration, P=21 MPa	118
Figure 5.38 Condensate saturation during the injection at of gases with 50% molar concentration, P=19.5 MPa	118
Figure 5.39 Condensate saturation during the injection at of gases with 50% molar concentration, P=17.75 MPa	119
Figure 5.40 Condensate saturation during the injection at of gases with 50% molar concentration, P=14.75 MPa	119

Figure 5.41	Condensate saturation reductions, for the different injected gases with molar concentrations of 50% (yellow) and 99% (blue).	120
Figure 5.42	Hexane recovery after the injection of gases with 99% molar fraction of C_1 , C_2 , CO_2 or N_2 .	121
Figure 5.43	Decane recovery after the injection of gases with 99% molar fraction of C_1 , C_2 , CO_2 or N_2 .	121
Figure 5.44	Hexadecane recovery after the injection of gases with 99% molar fraction of C_1 , C_2 , CO_2 or N_2 .	122
Figure 5.45	Hexane recovery after the injection of gases with 50% molar fraction of C_1 , C_2 , CO_2 or N_2 .	122
Figure 5.46	Decane recovery after the injection of gases with 50% molar fraction of C_1 , C_2 , CO_2 or N_2 .	123
Figure 5.47	Hexadecane recovery after the injection of gases with 50% molar fraction of C_1 , C_2 , CO_2 or N_2 .	123
Figure 5.48	Calculated interfacial tension for mixtures of the reservoir fluid with C_1 , C_2 , CO_2 or N_2 .	125
Figure 5.49	Gas relative permeabilities before and after the injection of the gas mixtures containing 99% of C_1 , C_2 , CO_2 or N_2 .	126
Figure 5.50	Gas relative permeabilities before and after the injection of the gas mixtures containing 50% of C_1 , C_2 , CO_2 or N_2 .	126

List of tables

Table 2.1	Gas-condensate mixture composition	20
Table 5.1	Pressure and viscosities of gas and condensate at 37°C and interfacial tension values of 0.015 and 0.037mN/m	80
Table 5.2	Compositional shift in the network at $\sigma = 0.037mN/m$ and $v_g = 18md^{-1}$. The values presented in this table represent molar percentages.	86
Table 5.3	Fluid mixture composition	94
Table 5.4	Fluid properties at the chosen flowing conditions	95
Table 5.5	Gas-condensate mixture composition.	107

1 Introduction

Gas-condensate reservoirs comprise gas systems that experience condensation under isothermal pressure depletion. This particular behavior is observed in reservoirs with temperatures lying between the critical point and cricondentherm, and initial pressures above the dew-point line, as illustrated in Figure 1.1. Submitted to these thermodynamic conditions, regions in the reservoir that undergo enough pressure reduction, as the vicinity of producing wells, enter the fluid mixture two-phase region, where condensate dropout takes place.

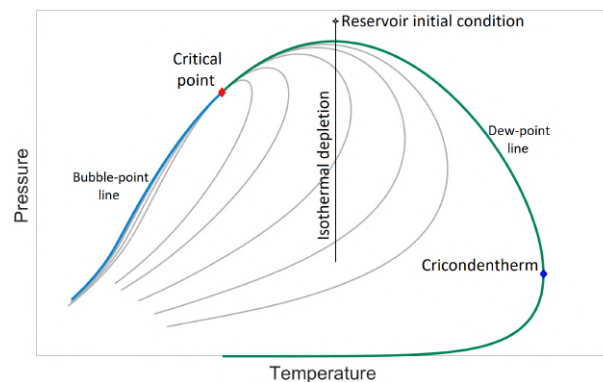


Figure 1.1: Phase diagram of a gas-condensate fluid

The newly formed liquid phase exhibits a relatively low mobility when compared to the gas, and, for this reason, tends to accumulate in porous media. As a consequence, gas flowing paths are blocked by the liquid and the wells productivity is significantly reduced, in a phenomenon known as condensate blockage. Besides the losses in produced volume, liquid banking affects negatively the produced gas composition, as the condensate trapped in porous medium is rich in valuable heavy components.

In order to minimize the negative effects of liquid dropout, several production optimization schemes and EOR methods have been proposed in the literature for gas-condensate reservoirs [13, 14, 15]. An adequate development of such methods requires deep understanding of the coupled flow of gas and condensate in porous media, which has been proved to be fundamentally different from that observed in conventional two-phase flow systems [16].

Traditionally, data appertaining to gas-condensate fluids and their flow in reservoirs are obtained experimentally. PVT cell laboratory tests are commonly used to characterize the fluids, while core flooding experiments are used to provide macroscopic transport properties related to the flow of gas and condensate in porous media, such as critical condensate saturation (S_{cc}) and relative permeability curves [17, 18, 19, 20]. Additionally, visualization of gas and condensate flow in micromodels contribute with valuable qualitative data regarding flow patterns, phase change and phase trapping in pores [21, 2, 3]. However, due to experimental operation constraints, these experiments seldom reproduce extreme pressure and temperature conditions or use complex fluid compositions normally occurring in gas condensate reservoirs. This leads to significant uncertainties in results, since model fluids do not always accurately capture the flow characteristics of compositionally complex reservoir fluids and may not mimic the reservoir wettability [22].

As an alternative, similar data can be obtained via pore-scale modeling [23]. Pore-network models of multiphase flow could be particularly suitable for this purpose, as they have shown promising results for predictive purposes, while being computationally less demanding than direct models [24]. Although extensive research effort has been directed to the development of this class of simulation tools in the past decades, just a few studies regard specifically gas and condensate flow.

1.1 Objective

The objective of the present thesis is the development of a predictive compositional pore-network model for gas-condensate flow in porous media. With the developed model, we intent to produce tailored data to large-scale gas-condensate reservoir simulation, based on specific reservoir rock properties, fluid composition, and flow conditions. These data could lead to more realistic production estimations and benefit gas-condensate fields development planning.

1.2 Chapters overview

This thesis is organized in six chapters. Chapter 2 presents a literature review on gas-condensate reservoirs. This chapter includes important concepts related to gas-condensate fluids and central aspects pertaining to condensate formation and gas and condensate coupled flow in porous media, from quali-

tative descriptions of micro-scale physical phenomena to ways of quantifying the flow at the macro-scale.

Chapter 3 presents a literature review on pore-network modeling. This chapter begins by discussing the fundamentals of pore-network modeling, including the definition of the network topology, the geometry of the pore elements, different ways of representing multiphase flow and the two basic algorithm categories. Then, an extensive literature review of pore-network models specifically devised to represent gas-condensate flow is presented.

Chapter 4 presents the mathematical formulation of the proposed pore-network model for gas-condensate flow. This chapter describes the adopted geometric representation of porous media, the implemented condensation mode and two-phase flow pattern, the equations governing the flow and the enforced phase equilibrium calculations.

Chapter 5 contains the results obtained with the proposed model, and is divided into two main sections. First, the model validation is presented, by reproducing experimental relative permeability data from the literature. Then, the evaluation of two prospect enhanced recovery methods for gas-condensate reservoirs, namely wettability alteration and gas injection, are carried out using the validated model.

Chapter 6 presents this thesis' concluding remarks and future work suggestions.

2

Gas-condensate reservoirs

2.1

Petroleum reservoir fluids characterization

Petroleum reservoir fluids are normally divided into four categories: black oil, volatile oil, gas-condensate and natural gas [1]. Their classification derives from the location of the mixture critical temperature and cricondentherm in relation to the reservoir temperature, as illustrated in Figure 2.1.

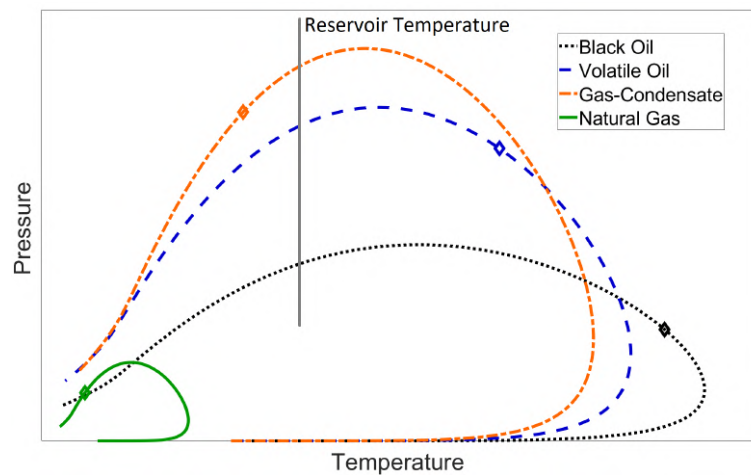


Figure 2.1: Petroleum reservoir fluid types. Adapted from [1]

The different types of fluids exhibit very distinct phase behaviors during the producing life of the reservoir, as their pressure is progressively reduced at relatively constant temperatures. For a black oil reservoir, the hydrocarbon mixture is liquid at the initial reservoir conditions and, during advanced stages of the isothermal depletion, a gas phase may be formed. This takes place when the pressure in the reservoir is lowered below the bubble point. Volatile oil reservoirs undergo a similar process, but their composition contains significantly higher fraction of lighter components, leading to earlier and more substantial gas formation in the reservoir during production. Gas-condensate and natural gas mixtures, on the other hand, find themselves as a single gas phase at initial reservoir conditions. During production, the pressure in a gas-condensate reservoir can be lowered below the mixture dew point pressure,

leading to the formation of a liquid phase in the reservoir. As condensation of gas mixtures ordinarily occurs at constant temperature as their pressure is increased, this phenomenon is also called retrograde condensation. For natural gas mixtures, pressure depletion does not affect the number of phases in the reservoir. For this case, the reservoir temperature is higher than the cricondenthem - the maximum temperature at which gas and liquid coexist - and the mixture two-phase region is not achieved. The formation of liquid in natural gas mixtures, therefore, may only occur granted that their temperature is reduced - for instance, upon reaching the surface during the production.

Starting in Section 2.2, the literature review focuses on gas-condensate fluids and their flow in porous media.

2.2

Gas-condensate fluids properties

Gas-condensate fluids go through substantial property variations during the reservoir pressure depletion. Once split into two phases, parameters that affect fundamentally flow in porous media – as saturations, interfacial tension, viscosity and density – become a strong function of the reservoir pressure. In the following sections, the phase behavior of gas-condensate fluids is discussed.

To assist with the analyses, an example of a gas-condensate fluid, presented in Table 2.1, is used. The phase envelope of the mixture, illustrated in Figure 2.2 and obtained with the CMG software Winprop, as well as all phase equilibrium calculations presented in this section, were computed using the Peng and Robinson equation of state [25] (discussed in Section 4.5). For this mixture to behave as a gas-condensate fluid, a reservoir temperature of 80°C , between the critical temperature (43.7°C) and cricondenthem (134°C), was selected. For simplicity, this mixture is labeled Mixture A.

Table 2.1: Gas-condensate mixture composition

Component	Molar Percentage
CO ₂	5
N ₂	2
C ₁	70
C ₂	5
C ₃	4
nC ₄	3
nC ₅	2
nC ₆	2
nC ₇	7

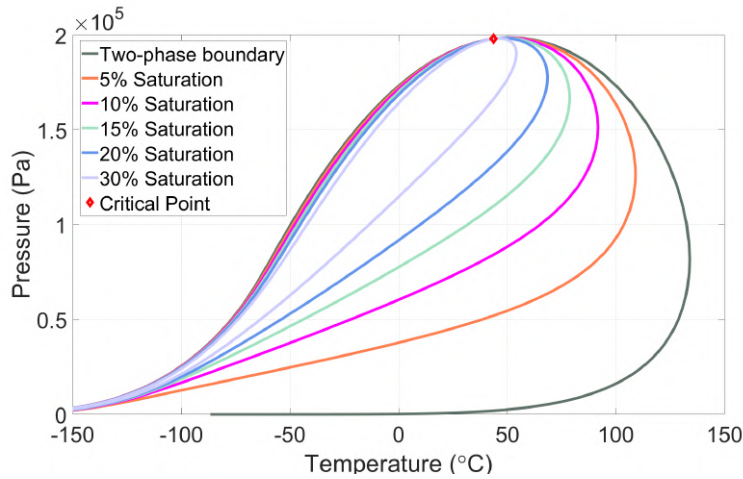


Figure 2.2: Phase envelope the mixture presented in Table 2.1. In this figure, obtained with the CMG software Winprop, the saturation lines represent the volumetric fraction of the liquid or gaseous phases.

2.2.1 Liquid dropout

Liquid dropout measurements quantify the liquid saturation in a gas-condensate mixture as a function of pressure, at constant temperature. These measurements are important for the determination of the mixture dew point pressure and for estimating the volume and rate of condensate deposition in porous media, as the pressure in the reservoir is depleted. Commonly, two different experiments are performed for liquid dropout quantification: constant composition expansion and constant volume depletion.

In constant composition expansion, a certain amount of the gas-condensate fluid is initially held in a cell at the reservoir temperature and

above the dew point pressure. The volume of the cell is then progressively increased, leading to a decrease in the mixture pressure. During the expansion, the content of the cell is not altered, and the formed liquid volume is quantified. Figure 2.3 presents the liquid dropout obtained at constant composition (solid line) for Mixture A, at 80°C . The dew point pressure was found at 18.39MPa , and the liquid saturation increased rapidly as the pressure was depleted beyond this value. A maximum liquid dropout of 14.44% was obtained at a pressure of 16.3MPa , and further pressure reduction led to the re-vaporization of the liquid phase. This increase and decrease in liquid saturation at a fixed composition can also be understood by looking at the constant saturation lines crossed by the 80°C isotherm, in the phase envelope shown in Figure 2.2.

Alternatively, in constant volume depletion, the composition of the mixture held in the cell varies, so that the volume can be kept constant during depletion. In this case, as the mixture is depleted below the dew point pressure, the volume occupied by the gas and the liquid phases is maintained by constantly removing material from the gas phase. With this procedure, the composition in the measuring cell becomes richer in heavier components at lower pressures. The liquid dropout of Mixture 1 obtained at constant volume expansion is also presented in Figure 2.3.

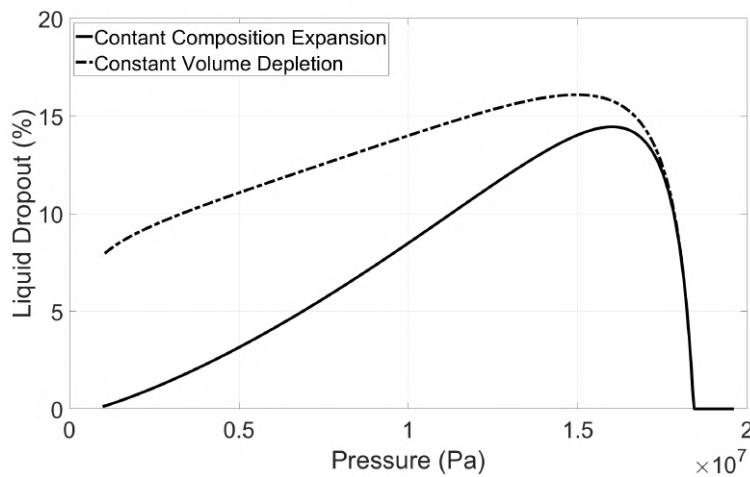


Figure 2.3: Liquid dropout of Mixture A at 80°C

Constant volume depletion measurements are particularly useful for reservoir engineering purposes, as the experiment resembles the depletion process in a reservoir. Taking into account the facts that the gas phase has higher mobility in porous media than the liquid, and that the reservoir volume is relatively constant during depletion, it is reasonable to consider that the reservoir will go through a similar compositional change during production [26, 27]. These measurements provide, therefore, important insights into the

produced gas composition and the in situ liquid saturations of a gas-condensate reservoir as the pressure is depleted during production.

2.2.2

Compositional differences between the phases

Complementary to the liquid dropout analysis presented in section 2.2.1, an important characteristic of gas-condensate fluids is related to the differences in composition between gas and liquid phases. As the mixture enters the two-phase region, the formed liquid phase is richer in heavier components, leaving the remaining gas lighter. This difference, associated with the phases different abilities to flow in porous media, can lead to significant compositional variations in gas-condensate reservoirs.

As an illustration of the compositional differences between gas and condensate, Figure 2.4 presents the molar percentages of C_1 and C_7 in the phases produced by Mixture A, at $80^\circ C$. The contents of methane and heptane in the phases are evaluated, as they represent the lightest and heaviest hydrocarbon components of the example mixture. For the analyzed gas-condensate mixture, it is noticeable that the gas composition changes marginally with pressure, while the condensate composition varies significantly. Starting at pressures near the dew point, both phases exhibit similar compositions to that presented in Table 2.1, with C_1 and C_7 contents around 70% and 7%, respectively. As the pressure is lowered, the heavy component fraction rises rapidly in the condensate, making liquid and gas phases very distinct.

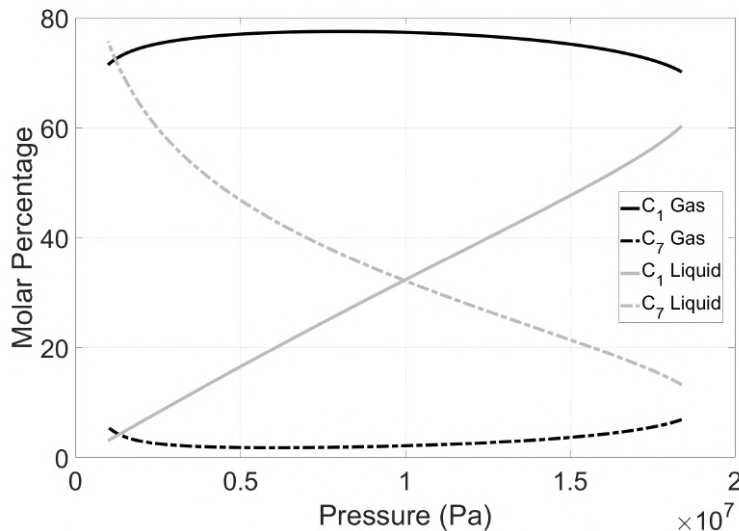


Figure 2.4: Molar percentages of C_1 and C_7 in the gas and liquid phases of Mixture A

2.2.3

Viscosity and density

The viscosity and density of gas and condensate phases can also be significantly affected by changes in the system pressure. Following the phase split, the liquid phase tends to become denser and more viscous with pressure depletion. The opposite is verified in the gas phase. The effects of pressure in the viscosity and density of the phases generated by Mixture A at 80°C are presented in Figures 2.5 and 2.6. For the viscosity calculations, the Lohrenz-Bray-Clark (LBC) [28] correlation was used.

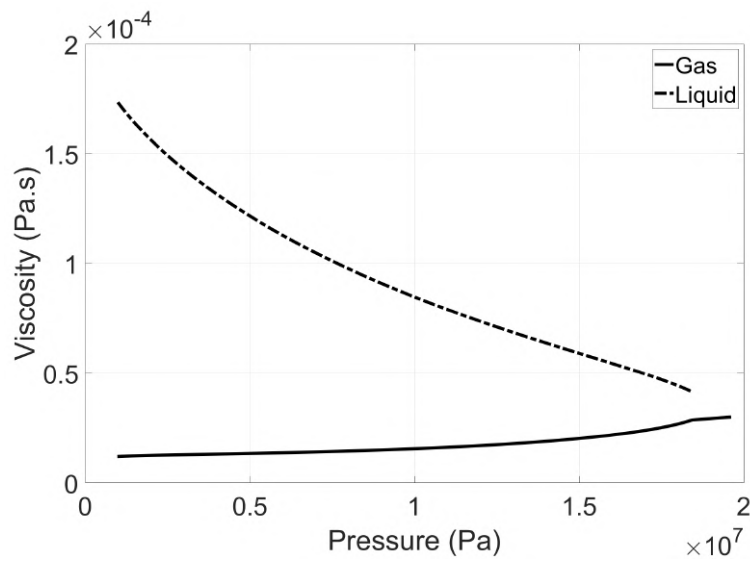


Figure 2.5: Viscosities of the gas and liquid phases of Mixture A, at 80°C

For the analyzed example, the viscosity ratio between liquid and gas undergoes a tenfold increase as the pressure is reduced. Using the LBC correlation, a slight decrease in the gas viscosity was estimated during depletion, while the condensate viscosity augmented considerably, as the heavier hydrocarbons fraction in the liquid phase becomes much larger at low pressures.

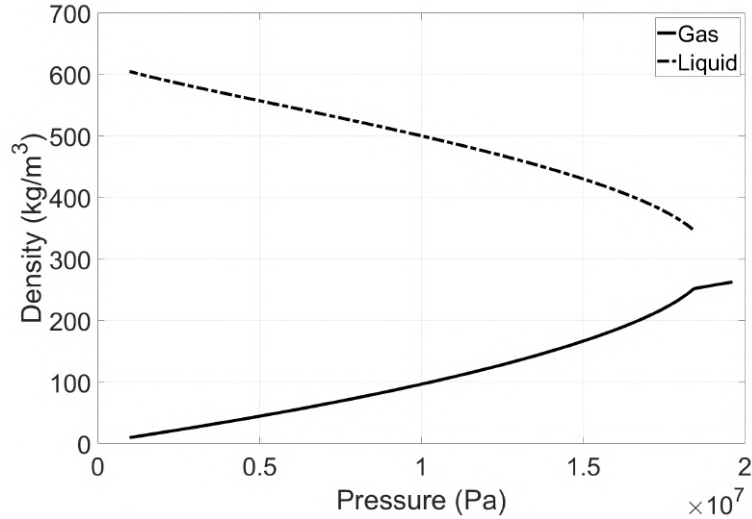


Figure 2.6: Densities of the gas and liquid phases of Mixture A, at 80°C

A similar effect is observed in the density of the phases during depletion. In the evaluated pressure interval, the density ratio between liquid and gas rose from 1.4 to 62.8. Unlike the viscosity, the density of both phases are significantly affected by pressure. In this case, the variation in condensate density can be attributed mainly to the increase in heavier components content, while the gas density decreases mostly due to the phase large compressibility.

2.2.4 Interfacial tension

The interfacial tension between the gas and liquid phases in a gas-condensate fluid is also a strong function of pressure. Just below the dew point pressure, the similarity between the phases composition and properties lead to very low values of interfacial tension. As the pressure is lowered further within the two-phase region, however, interfacial tension values become significantly higher. Figure 2.7 presents the interfacial tension of Mixture A as a function of the pressure, calculated with the correlation proposed by Weinaug and Katz [29].

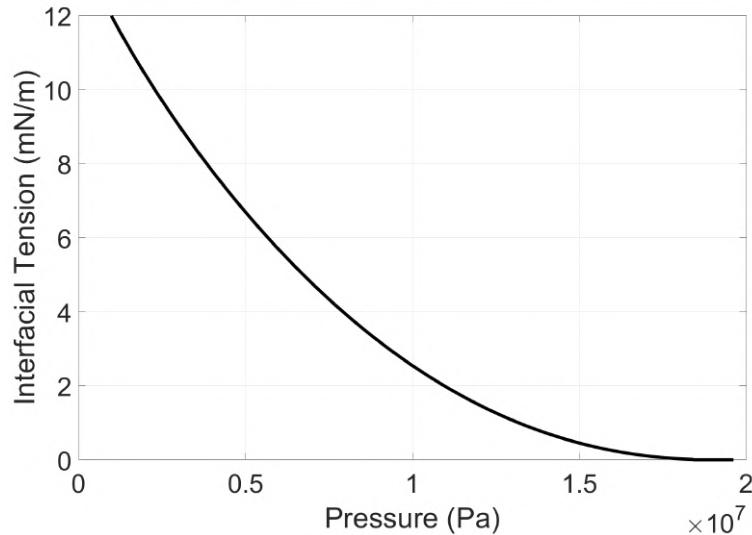


Figure 2.7: Interfacial tension between the phases of Mixture A, at 80°C

In the pressure interval used for the analysis, the interfacial tension between gas and condensate varied from $0.0085\text{mN}/\text{m}$, just below the dew point pressure, to $12\text{mN}/\text{m}$.

2.3

Gas-condensate flow in porous media

Once the most relevant physical and transport properties of gas-condensate fluids were presented in Section 2.2, their flow in porous-media can be better understood. In this section, the flow of gas-condensate fluids in porous media is explored, from observations of condensate formation and flow at the pore-scale, to ways of representing gas-condensate flow at the macro-scale.

2.3.1

Condensation and flow visualization at the pore-scale

Macro transport properties for geological porous media derive from events taking place at the pore-scale. Therefore, identifying the physical phenomena occurring at the micro-scale during multi-phase flow in porous media contributes decisively to flow understanding and modeling.

Unlike in conventional immiscible two-phase systems, gas and condensate flow originates from condensation in situ. The phases distribution in porous media is, therefore, expected to be different from that generated through imbibition or drainage processes. Moreover, the low interfacial tension between gas and condensate (Section 2.2.4) can lead to flow characteristics unlike those observed in immiscible fluids. For these reasons, micro-scale visualization

experiments comprising phase change and condensing flows in porous media can provide relevant information for gas-condensate production estimation.

Coşkuner [2] performed condensation and flow experiments in glass micromodels with a gas-condensate reservoir fluid under reservoir conditions. During the condensation experiments, the micromodel was first loaded with the mixture above the dew point pressure and then depleted from both sides. Figure 2.8 (a) shows the micromodel above the dew point pressure, while Figures 2.8 (b) and (c) represent two stages of depletion within the two-phase region. It is clear from the images that the liquid phase forms wetting films deposited on the pore walls, while the gas occupies the pore centers. The formation of wetting films upon condensation is also expected to take place in gas-condensate reservoirs, as the reservoir rocks tend to be strongly wetted by liquid [30].

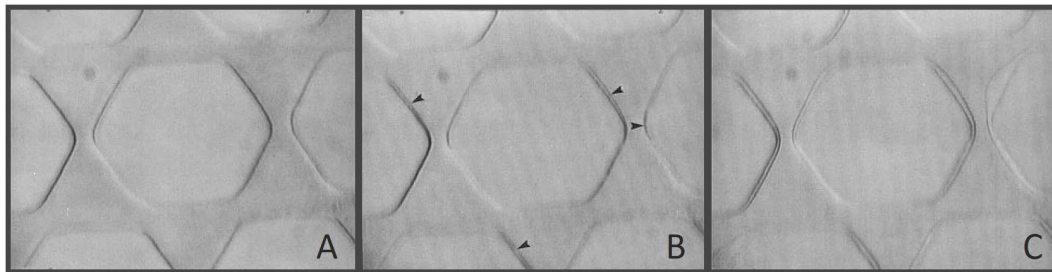


Figure 2.8: Condensation experiment in micromodel, conducted by Coşkuner [2]

Gas-condensate flow visualization experiments were performed by the same author at different levels of imposed pressure in the micromodel. Just below the dew point pressure, Coşkuner observed that the flow of gas was not affected significantly by the presence of condensate, as the interfacial tension in the region is very low. Under this condition, gas/condensate interfaces were easily deformed and the viscous pressure difference required for the flow was not high. It was also observed that, in the vicinity of the dew point pressure, the density contrast between the phases grew more significantly than the interfacial tension. Therefore, in the absence of significant viscous forces, the phases tended to segregate due to the relatively high gravity forces. This behavior is expected to happen in the reservoir, in regions far from wellbores. Finally, the author remarked that the condensate presented a high tendency to be collected in lenses spanning the entire cross section of flowing channels. In this case, part of the condensate was free to flow in the form of a film, while the rest was immobile in lenses. As the interfacial tension between the phases

increases during depletion, these lenses start to impose a substantial blockage for the gas flow. Such lenses can be observed in Figure 2.9. By perceiving very distinct flow regimes as the pressure – and pressure gradients – varied in the micromodel, Coşkuner suggested that different relative permeability curves should be devised for gas-condensate flow, according to flow rates and interfacial tension values.

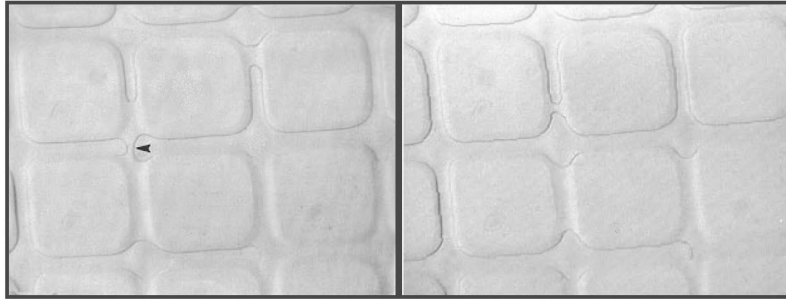


Figure 2.9: Condensate bridges observed during gas-condensate flow in micromodel, conducted by Coşkuner [2]

Similar visualization experiments were performed by Dawe and Grattoni [3], in which a partially miscible binary fluid system was used to evaluate phase change and low interfacial tension flow in porous media. In this study, the fluid mixture was composed by water and lutidine, so both evaluated phases were liquid. Complementarily to the observations presented by Coşkuner, the authors were interested in the pore-scale mechanisms of both wetting and non-wetting phase dropout. Figures 2.10 (a) and (b) illustrate the cases in which the emergent phase is the non-wetting and the wetting phase in the porous medium, respectively. While in Figure 2.10 (a) the formed phase nucleated in the bulk of the solution, in (b) the separation occurred with the formation of a wetting layer. These findings substantiate the idea that condensate dropout in reservoirs is followed by the formation and flow in wetting films at pore walls.

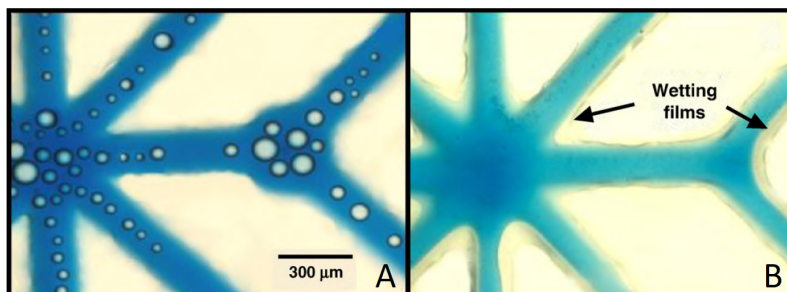


Figure 2.10: Experiments of phase separation for wetting and non-wetting emerging phases, conducted by Dawe and Grattoni [3]

The flow of gas-condensate fluids in glass micromodels was also investigated by Jamiolahmady *et al.* [4]. They used micromodels with heterogeneous pore patterns reproduced from real rock micrographs and a mixture of C_1 and nC_4 to represent the gas-condensate fluid. Connate water saturation was established in the micromodels by flooding water followed by the C_1/nC_4 mixture above the dew point pressure. Then, for the gas-condensate flow analysis, the micromodel pressure was lowered below the dew point, and equilibrated gas and condensate were injected simultaneously. During the experiments, the authors observed that while condensate filled some pores, gas and condensate flowed together through most of pores. The condensate bridges reported by Coşkuner [2] were also observed, blocking the gas flow. After the liquid bridge formation, an apparent local pressure build up behind the bridge was reported, which could eventually overcome the bridge capillary forces and reestablish the gas flow. This closing and opening of flowing channels repeated itself in a cyclic manner at some parts in the porous medium. Figure 2.11 shows snapshots of the experiment, in ascending temporal order from left to right. Points A, B and C highlight regions in which cyclic condensate bridge formation and removal occurred.

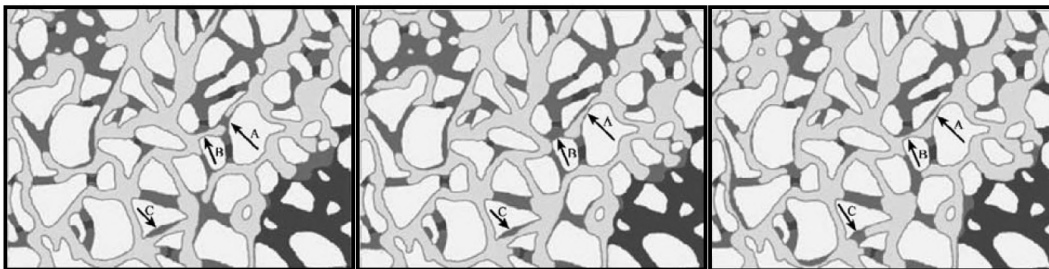


Figure 2.11: Points of cyclic condensate bridge opening and closing during the experiments performed by Jamiolahmady *et al.* [4]. Water is represented in dark gray, condensate in medium gray, gas in light gray and the porous medium grains in white.

The works mentioned in this section highlighted important characteristics of condensate dropout and gas-condensate flow at the pore-scale which should be taken into consideration in macro-scale flow modeling. In the next section, approaches to model gas-condensate flow at reservoir-scale will be assessed.

2.3.2

Macro-scale modeling of gas-condensate flow in porous media

Liquid dropout and accumulation in the vicinity of wellbores restrict considerably gas productivity. Several cases of substantial production decrease

in gas-condensate reservoirs at pressures below the dew point pressure have been described in the literature. Afidick *et al.* [31] reported losses in well productivity in the order of 50% in a gas-condensate field with a fairly lean fluid. In a constant composition test, a condensate dropout of only 1.1% was measured for the field mixture. The authors attributed the large productivity decrease to liquid accumulation in the near wellbore region due to low liquid mobility. Barnum *et al.* [32] presented an example of a moderately rich gas-condensate reservoir in which wells ceased to produce right after the flowing bottom-hole pressure reached the dew point. In the occasion, data from surrounding wells indicated that the average reservoir pressure was still over 2000 psi above the mixture dew point. El-Banbi *et al.* [33] also reported severe liquid accumulation in the vicinity of wellbores of a moderately rich gas-condensate reservoir after pressure reduction below the dew point. A maximum condensate saturation of 68% was identified in the near wellbore region, which was considerable above the maximum liquid dropout obtained with the fluid at constant volume depletion experiments. At an irreducible water saturation of 20%, this drastic condensate accumulation reduced the gas productivity in more than 90%.

Accurately modeling liquid accumulation and well productivity decline manifested in gas-condensate reservoirs is essential for field development planning. With this purpose, three distinct regions are commonly delineated in the reservoir. These regions, characterized by the liquid phase content and mobility, are illustrated in Figure 2.12. Region III is the farthest region from the producing wells, where the pressure is above the dew point pressure and the hydrocarbon mixture is in the gaseous state. Moving closer to the well, region II is reached, where the pressures become lower than the dew point pressure and condensate is formed. In this region, however, the liquid saturations are below the threshold for liquid mobility, known as condensate critical saturation (S_{cc}), and only the gas phase flows. For this reason, liquid accumulates and local condensate contents above the liquid dropout saturation are observed. Finally, in region I, closest to the producing wells, the liquid content is high enough for the condensate to flow with the gas phase. Yet, liquid accumulation also takes place during the two-phase gas-condensate flow, as the condensate mobility tends to be low even at substantial liquid saturations.

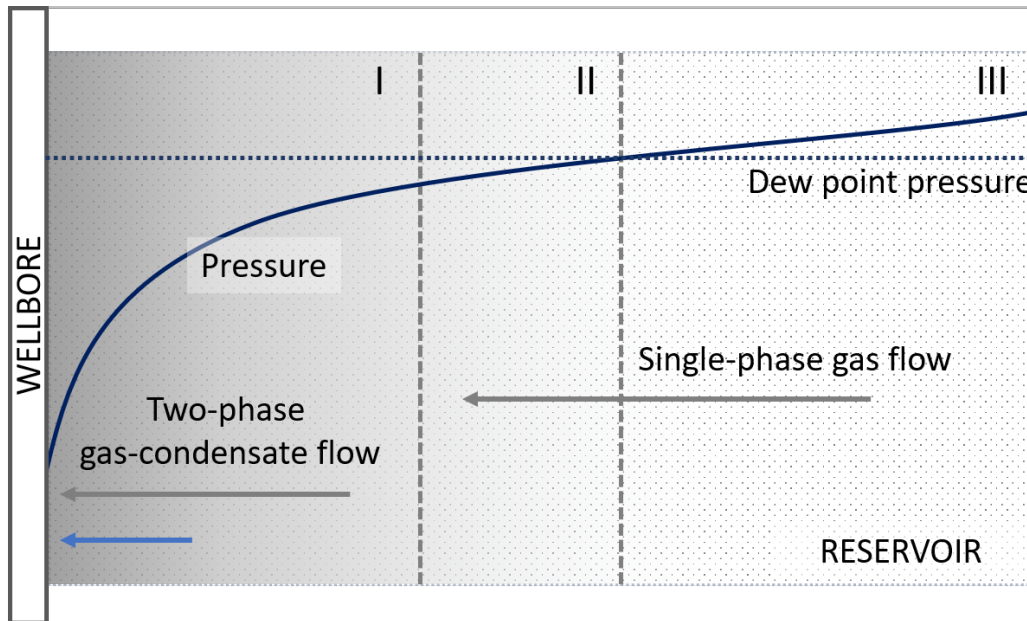


Figure 2.12: Classification of reservoir zones according to condensate mobility and saturation

Gas-condensate fluid flow in the three regions is modeled at the macro-scale using the Darcy's law adapted for multiphase flow (Eq. 2-1). In this equation, \mathbf{u}_a is the vector containing the superficial velocities of phase a , \mathbf{K} is the the tensor containing the porous medium permeability, k_{ra} is the the relative permeability of phase a , P is the pressure, ρ_a is the density of phase a , \mathbf{g} is the gravitational acceleration vector and μ_a is the viscosity of phase a .

$$\mathbf{u}_a = \frac{\mathbf{K}k_{ra} \cdot (\nabla P + \rho_a \mathbf{g})}{\mu_a} \quad (2-1)$$

Expressed as a function of the phases saturations in porous media, the relative permeabilities quantify the ability of a phase to flow in the presence of another. The relative permeability curves contain, therefore, fundamental information to model gas and condensate flow in reservoirs. Using the gas and condensate relative permeability curves illustrated in Figure 2.13 as an example, the fractional flows of gas and liquid in the three regions of Figure 2.12 can be predicted. In region III, the condensate saturation is zero, meaning that the gas relative permeability (k_{rg}) is one and the condensate relative permeability (k_{rl}) is zero. Within the mixture two-phase envelope, in region II, the condensate saturation is below the mobility threshold, which for the example curve is $S_{cc} = 15\%$. Then, the gas flowing from region III to II will lose heavier components in the immobile liquid phase and advance towards the well leaner. Also in this region, while only gas flows, the gas relative permeabilities are reduced by the presence of liquid. When the local

liquid saturation accumulates above the S_{cc} , the region I is accessed and the condensate relative permeability is no longer zero. For the example curve, two-phase gas-condensate flow would take place in region I for condensate saturations between the S_{cc} and approximately 55%, when the gas relative permeability becomes zero.

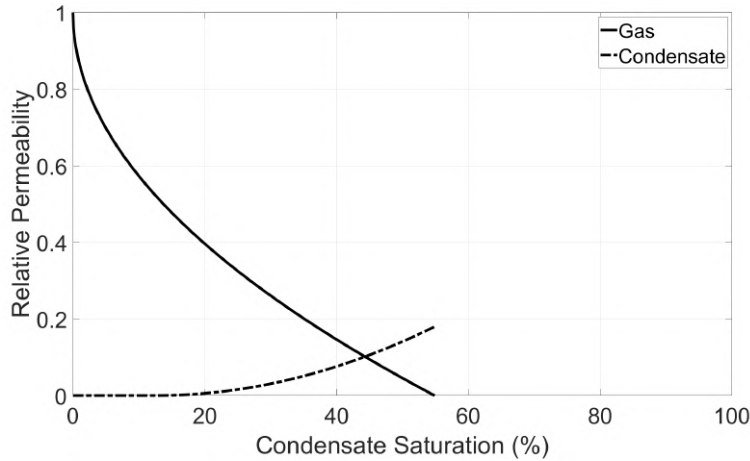


Figure 2.13: Relative permeability curves for gas and condensate in the absence of connate water.

It is clear, therefore, how predictive modeling of gas-condensate flow relies on adequately determined relative permeability curves. Devising these curves for gas-condensate fluids, in its turn, is not a trivial task. The particular phase topology of gas and condensate in porous media, associated with the phases unique properties, produces relative permeability for gas and condensate that are rate and interfacial tension dependent [34, 16]. While increasing the flow rate produces a positive impact on relative permeability curves for gas and condensate, increasing the interfacial tension has the opposite effect. As flow rate and interfacial tension vary significantly in the path from far to near wellbore regions in gas-condensate reservoirs, their effects on the relative permeabilities must be well characterized.

As discussed in section 2.3.1, condensate dropout in porous media is initiated in wetting layers that spread over pore walls, as a result of the rocks strong liquid wettability. With liquid saturation increase, these wetting layers swell and tend to form bridges that close and open intermittently, blocking the gas flow. With this, the gas becomes disconnected in porous media, taking the form of isolated ganglia rather than a continuously connected gas pathway. Armstrong *et al.* [35] evaluated the role of phase topology and ganglion dynamics in two-phase flow. Using fast x-ray microtomography of water-oil flow at the pore-scale, they concluded that ganglion dynamics is an

important transport mechanism behind the rate effect on relative permeability. At constant saturations, they observed that the phase topology evolved with flow conditions and affected the fractional flow of oil and water. Following the same logic, the flow of gas in ganglia in gas-condensate reservoirs leads to the rate dependency of relative permeability curves. According to the local flow rate – and consequently the relative influence of viscous forces over capillary forces –, gas ganglia may be trapped or flow in porous media, affecting, in this manner, gas relative permeability. As for the interfacial tension effect, it comes from the fact that gas-condensate systems, unlike water-oil systems, undergo substantial interfacial tension variation during pressure depletion. In the same manner as the local flow rate affects viscous forces, the acting interfacial tension affects capillary forces, playing an important role in ganglion trapping, and, consequently, in relative permeabilities.

For these reasons, substantial research effort has been directed to determining gas-condensate relative permeability curves. In the next section, a review of methods of devising such curves is presented.

2.3.3 Relative permeabilities

Henderson *et al.* [34] were the first to report the effect of velocity and interfacial tension on relative permeability curves of gas-condensate fluids. The authors performed coreflooding experiments in a long sandstone core using a six component gas-condensate mixture. The tests were conducted at two-different low interfacial tension values – 0.05 and 0.4mN/m – and three gas flowing velocities – 0.88, 8.8 and 35.2m/day. The highest tested velocity corresponded to the flow at a distance of 3 – 5m from the wellbore of a typical North Sea gas-condensate reservoir. It was found that the positive flow rate effect on relative permeability was more pronounced at the interfacial tension of 0.05mN/m than at 0.4mN/m. It was also noticed that increasing the interfacial tension to 0.4mN/m reduced, on average, the relative permeabilities of the gas and condensate in 75% and 20%, respectively. In general, the observed effects were much more significant on the curves related to the gas phase than on the condensate curves. In order to determine whether the positive rate effects occurred only in gas-condensate systems, conventional gas-oil flow through the same sandstone core at the interfacial tension value of 0.14mN/m was evaluated. At different tested flow rates, a negligible positive effect on relative permeability was observed for the conventional system. These findings support the idea that the dependency of gas-condensate relative permeabilities on flow rate and interfacial tension are related to the phase topology and flow regimes

stemmed from condensation in porous media.

Similar results were also obtained by Henderson *et al.* [36] using a binary mixture of C_1 and nC_4 as the gas-condensate fluid. In this study, a correlation between the gas relative permeabilities and capillary number was identified. The capillary number, expressed in Equation 2-2 for the gas phase, is a dimensionless number used to compare the effects of viscous and capillary forces. It compares, therefore, the forces which affect the relative permeability in a positive and negative manner.

$$N_c = \frac{v_g \mu_g}{\sigma} \quad (2-2)$$

where v_g is the gas flowing velocity and σ is the interfacial tension between gas and condensate.

For example, during the performed coreflooding experiments, the authors measured the same gas relative permeability for the lowest tested rate, $9.25m/day$, with $\sigma = 0.14mN/m$ and for the highest tested rate, $74m/day$, with $\sigma = 0.9mN/m$. For both cases, the value of N_c was approximately 1.4×10^{-5} . In these cases, the negative effect of increasing the interfacial tension was canceled out by the positive effect of increasing the flow rate.

Following the idea of correlating relative permeabilities with capillary number, Blom and Hagoort [37] evaluated several methods of devising relative permeability curves using N_c as a parameter. All investigated methods adopted an approach of interpolating between relative permeability curves of immiscible and miscible flows, using weighting functions dependent on capillary number. This approach is based on the widely used relative permeability correlation proposed by Coats in 1980 [38], in which the curves are interpolated using a weighting parameter dependent on the interfacial tension. Immiscible flow curves were obtained at very low N_c , when the interfacial tension between the phases is high and the flow characteristics are akin to conventional two-phase flow in porous media. Miscible flows, occurring at vanishing interfacial tensions (very high N_c), were modeled using straight relative permeability curves. In this case, one flowing phase is unable to trap the other, and the fractional flows are equivalent to the phases saturations. For the evaluated methods, Corey relative permeability functions [39] were used, both by interpolating the Corey coefficients and generating a curve, or by interpolating the generated curves for immiscible and miscible cases. The effectiveness of each method was evaluated by comparing the predicted results with four sets of experimental relative permeability data, obtained at varying interfacial tension and flow velocity. After comparing predicted and measured curves, the authors indicated the weighting function proposed by Whitson and Fevang [40] as the best

among the evaluated methods. Nonetheless, the results indicated that no tested correlation could adequately match, at the same time, both gas and condensate relative permeability values.

The idea of interpolating between miscible and immiscible relative permeability curves continued popular among researchers seeking to model gas-condensate relative permeabilities. Pope *et al.* [41] developed an interpolation model based on a trapping number, instead of capillary number, so that the effects of buoyancy were also taken into account. The authors claimed that gas and condensate relative permeabilities depended on the ratio of forces on the trapped phase, which can be calculated with the capillary number, in the case where viscous and capillary forces predominate, or with the Bond number (Eq. 2-3), when buoyancy and capillary forces prevail. Based on this premise, a trapping number, N_T , obtained by the vector sum of capillary and Bond numbers, was used to model gas and condensate relative permeabilities. Their model produced reasonable predictions for the relative permeabilities of both phases, when tested against experimental data, but required as inputs N_T , two trapping parameters – not defined in the publication– and the measured relative permeability curves at low trapping number (high interfacial tension).

$$N_B = \frac{\Delta\rho g L^2}{\sigma} \quad (2-3)$$

where $\Delta\rho$ is the density difference between gas and condensate, g is the gravity acceleration, and L is a characteristic length.

The effects of inertia on the relative permeabilities of gas and condensate were also investigated by some authors. Contrary to buoyancy effects, that tend to be relevant only far from the wellbore, inertial effects take place in the vicinity of flowing wells, where very high gas flowing velocities occur. In this case, conflicting effects would influence gas and condensate production, since inertial effects reduce relative permeabilities. Mott *et al.* [20] conducted flooding tests with a low permeability sandstone core using a five components gas-condensate fluid. Relative permeabilities were measured at capillary numbers between 4×10^{-6} and 4×10^{-4} . Within all this range, the net effect of velocity on the relative permeabilities was positive, even though measurements using only gas indicated that negative inertial effects were present at the tested flowing velocities. The authors also used the measured data to fit a correlation for the relative permeabilities, and found that the best approach was to interpolate between miscible and immiscible curves using a function of the capillary number, while modeling the inertial flow effects separately, through a non-Darcy factor. Henderson *et al.* [42] conducted core tests to evaluate the effect of inertia using a mixture of C_1 and nC_4 at interfacial tension

values between 0.015 to 0.78mN/m and flowing velocities ranging from 7 to 700m/day. Unlike in the study presented by Mott *et al.* [20], here the authors could identify a reduction in the gas relative permeabilities as the flowing velocity increased, given that the liquid saturation in the cores was low. For the measurements at an interfacial tension of 0.78mN/m, they observed that, for condensate saturations below 25%, inertial effects were substantial and the maximum gas relative permeabilities were found at gas flowing velocities between 58.1 and 116.2m/day. At high condensate saturations, however, the effect of inertia was balanced out by the positive coupling effect, and the maximum relative permeabilities were measured for the highest flowing velocities. For the measurements conducted at an interfacial tension of 0.037mN/m, a similar behavior for the curves was found. For both cases, even when inertia was the dominant effect, the reduction in gas relative permeability was milder with the presence of condensate, when compared to the cases where gas was the only phase in porous media.

A very systematic procedure was presented by Whitson *et al.* [43] to model gas and condensate relative permeabilities for well calculations, taking into account the effects of capillary number, high velocity flow, and heterogeneities in the reservoir. In their model, they make use of the fact that the relative permeability ratio between gas and condensate, k_{rg}/k_{ro} , is a purely thermodynamic variable at steady-state flow. Determining the relative permeabilities as a function of saturation becomes, therefore, unnecessary, and the authors present special steady-state experimental procedures to measure k_{rg} as a function of k_{rg}/k_{ro} and N_c . With the model, which also uses the approach of interpolating between immiscible and miscible curves, once the $k_{rg} = f(k_{rg}/k_{ro})$ relationship is established and correlated with N_c , accurate modeling of condensate blockage is possible. To take the effects of high velocity flow into consideration, a β factor, used in the Forchheimer equation (Eq. 2-4), was calculated with a formulation from the literature. To conclude the study, the authors presented results of their model applied to calculate well performance in a rich gas-condensate reservoir with two well configurations, namely radial and a vertically-fractured wells. For both configurations, the results obtained with three modeling options were compared: k_{rg} modeling including capillary number and high velocity flow effects, k_{rg} modeling including only capillary number effects, or k_{rg} modeled with immiscible flow curves. For the studied case, capillary number effects impacted significantly gas flowing rates, while high velocity flow effects had a second-order influence on gas flow.

$$\frac{\partial P}{\partial x} = \frac{\mu}{k}v + \beta\rho v^2 \quad (2-4)$$

where k is the porous medium permeability and β is the non-Darcy, or Forchheimer, coefficient.

Jamiolahmady *et al.* [44] also proposed a correlation for relative permeabilities of gas and condensate, which included the effects of positive coupling and inertia. In the development of the correlation, a large data bank of measured gas and condensate relative permeabilities was used to ensure generalizability of the predictions. Relative permeabilities were expressed in terms of fractional flow, and not saturation. The authors claimed that, by following this approach, measured k_{rg} and k_{rc} in different cores become more similar, lowering the required number of curves in reservoir studies. The correlation proposed an interpolation between low velocity/high interfacial tension relative permeability curves – labeled as base curves – and miscible curves, which in turn had already been corrected for the effects of inertia. The interpolation weighting parameter, Y_g , fitted with the available data bank, was a function of both N_c and interfacial tension between the phases, but not rock parameters. Therefore, the only required experimental rock data is related to the base curves. Error analysis for the general correlation predictions, using experimental k_r measurements on both carbonate and sandstone cores (not used to fit Y_g) demonstrated satisfactory accuracy. As a disadvantage for this correlation, by expressing the relative permeabilities in terms of fractional flow, it generates k_r dependent not only on capillary number, but also on viscosities. This dependence was implicitly accounted for in the values of interfacial tension, and, therefore, limits the applicability of the correlation to the same values of interfacial tension used to fit Y_g ($\sigma \leq 0.85mN/m$). This draw back was then eliminated from the correlation by Jamiolahmady *et al.* [45], by expressing the relative permeabilities in terms of the relative permeability ratio – similar to the approach proposed by Whitson *et al.* [43] – instead of fractional flow.

In order to support the generability of the proposed correlation, Jamiolahmady *et al.* [46] investigated experimentally the relative permeabilities of gas and condensate in propped-fracture porous media, and compared measured results with predictions. In the experiments, steady-stated gas-condensate flow was enforced through highly permeable fractures filled with proppant ($k = 146D$) and sand ($k = 15D$). At the experimental conditions, the fluids presented interfacial tensions between 0.15 and 0.85mN/m, and velocities between 250 and 3000m/day. It was verified that, for both highly permeable fractures, inertial effects were quite dominant, especially at lower interfacial tension values and low condensate-to-gas flow rates. For the most permeable fracture, at the same flowing velocities, relative permeabilities at low interfacial tension lower than those at high interfacial tension were observed. The

generalized correlation could express reasonably well the unique combined effect of positive coupling and inertia for the flow through the two fractures, considering that they have very different characteristics than the data used to fit the correlation.

The research effort to produce appropriate gas-condensate relative permeability correlations as a function of flowing velocity and fluid properties is still present in recent published studies. As examples, in 2019, Gholampour and Mahdiyar [47] proposed a correlation using an interpolation weighting parameter as a function of an inertial number – ratio between inertial and capillary forces. This was done as the authors suggested that the positive coupling effect observed with increasing gas-condensate flow rates stemmed from inertial and not viscous effects. After fitting the correlation parameters with a large data bank, in an approach similar to the study by Jamiolahmady *et al.*, [45], predictions could match experimental data obtained using varied cores and gas-condensate fluids properties within a reasonable margin of error. In 2020, Mahdaviara *et al.* [48] employed numerous smart computer aided algorithms to model gas and condensate relative permeabilities. More than a thousand data points from eight sets of experiments were used in the training and testing steps of the modeling process. Models with two (saturation and capillary number) and three (saturation, capillary number and interfacial tension) input parameters were generated and compared. Among the several tested modeling strategies, the model using three parameters generated by the Multilayer Perceptron (MLP) predictive method and optimized with the Levenberg-Marquardt Algorithm (LMA) generated the most reliable results. The MLP-LMA models, using both two or three inputs, demonstrated more accuracy when compared to traditional literature models.

Additionally to interfacial tension and flowing velocity, the dependency of relative permeabilities to the composition of gas-condensate fluids has also been investigated. This is particularly relevant considering that most experimentally measured relative permeabilities are obtained with core floodings using model fluids. Nagarajan *et al.* [22] conducted relative permeability measurements in both sandstone and carbonate cores, using three different model fluids and two live reservoir fluids. At the testing conditions, model and reservoir fluids displayed matching viscosities and interfacial tension values. The authors found that both gas and condensate relative permeabilities obtained using reservoir fluids were lower than those obtained with the tested model fluids, at any measured saturation. The relative permeabilities were also compared when expressed as a function of k_{rg}/k_{rc} , instead of saturation, since this procedure is supposed to generate more similar results when using different ex-

perimental parameters [43]. The comparison, indicated lower $k_{rg} = f(k_{rg}/k_{rc})$ for the reservoir fluid, for all range of evaluated k_{rg}/k_{rc} , than for the model fluids. This means that, at a given gas relative permeability, condensate relative permeabilities are lower for the reservoir fluids than for the model fluids, which indicates higher liquid accumulation in porous media. Kalla *et al.* [49] also compared the use of reservoir and model fluids during the experimental measurements of relative permeabilities of gas and condensate. In their findings, both k_{rg} and k_{rc} were higher for reservoir fluids than for model fluids, at a given saturation and interfacial tension. Although the observed trend was the opposite as in the one presented by Nagarajan *et al.*, both studies indicate that model fluids may not produce appropriate relative permeability curves for reservoir modeling.

Generating, therefore, gas and condensate relative permeability curves for reservoir-scale modeling is a rather challenging task. Additionally to the difficulty related to modeling the curves sensitivity to flow rate and interfacial tension, obtaining the curves experimentally can be quite complicated. Gas-condensate reservoir fluids normally present complex compositions which display retrograde condensation behavior at high pressures and high temperatures. Since using model fluids may influence the generated curves, even when interfacial values are matched, the extreme reservoir conditions should be reproduced experimentally, as a way to ensure representative results. As an alternative to experiments, relative permeability curves can be obtained using pore-network models. These models, which represent flow through a simplified morphological representation of porous media, have been used extensively in the past decades to generate predictive macro-scale transport properties for reservoir modeling. In the next chapter, a literature review about pore-network modeling is presented. In special, pore-network models representing gas-condensate flow in porous media are analyzed.

3

Pore-network modeling

3.1

Pore-scale modeling

Flow through porous media is commonly modeled using either continuum-scale or pore-scale models. Continuum-scale models, used to predict reservoir performance, do not directly capture physical processes at the pore-scale [24], and rely on averaged macro-scale transport properties to perform flow predictions. Pore-scale models, on the other hand, focus on evaluating the effects of flowing parameters on the micro-scale flow performance in porous media. Among the usually evaluated parameters are the fluids viscosity and density, fluid-fluid and fluid-solid interactions, e.g. interfacial tension and wettability, the porous space heterogeneity, and the flowing rate. With that, the sensitivity of flow in porous media to capillary, viscous, gravitational and inertial forces can be mapped, and macro-scale transport properties devised.

Pore-scale modeling methods fall into two categories: direct modeling and network modeling. In direct modeling, the equations governing the flow are solved directly in three-dimensional representations of porous media. Therefore, the first step in a direct modeling approach workflow is the creation of a continuous flowing domain representing the porous space of interest. Due to the significant advances in pore scale imaging occurred in the past decade [23, 50], the porous space of geological porous media can be accurately reconstructed, at least for pores larger than the imaging technique resolution, making the evaluation of complex morphology effects on flow possible. As a consequence of the resulting detailed representation of flow, however, direct modeling can be highly computationally demanding, especially when capillary dominated flows are modeled. Multiphase flow phenomena in porous medium, e.g. flow through thin wetting films, require the use of a refined mesh in the space discretization [51]. Additionally, dealing with fluid-fluid and fluid-solid interfaces can be numerically difficult [50]. For these reasons, modeling multiphase flow in a representative volume, particularly for heterogeneous porous media, can be prohibitive. Thus, as of now, direct modeling is the preferred modeling approach only for single-phase flow analysis. The most popular methods for direct

modeling are the Lattice Boltzmann method and traditional CFD (computational fluid dynamics) methods, as finite differences, finite volumes and finite elements. Descriptions of advantages and disadvantages of these methods, as well as a survey on the current state of pore-scale imaging technology, can be found in the review publications by Blunt *et al.* [23] and Bultreys *et al.* [50].

Alternatively to direct modeling, in pore-network modeling the flow is solved through simplified representations of the porous space. In this approach, a pore-network, normally constituted by pore bodies – larger voids – connected by pore throats – smaller void constrictions – , is constructed to represent porous media. The network elements have simplified shapes, e.g. spherical, cubic, cylindrical, for which analytical or semi-analytical hydraulic conductances are devised and used to calculate the flow. As a consequence, this approach leads to significantly less computationally demanding models for multiphase flow. The central question in pore-network modeling is how simplified the representation of the porous space can be, for the obtained results to be predictive of flow through complex porous media. As of today, pore-network models are the most successful models for estimations of two-phase and three-phase flows in the geological field [50]. Although numerous studies have been published in the area in the past two decades, improving the predictability of pore-network models remains an active research topic [51].

In the next sections, a literature review of the most important aspects related to pore-network modeling is presented. Additionally, the works in the area focused on the representation of gas-condensate flow are discussed.

3.2

Pore-network structure

3.2.1

Network topology

Network topology refers to the spatial disposition of pore bodies in the porous space, both in two and three-dimensional configurations, and how they are connected by pore throats. There are two main categories of pore-networks, when it comes to defining the network topology: synthetic networks, with pore bodies arbitrarily disposed and connected by throats, and image based networks, which are created to match spatially an specific porous medium mapped through pore-scale imaging. Next, both types of network construction are be briefly discussed.

3.2.1.1 Synthetic networks

Synthetic networks commonly use cubic (3D) or square (2D) regular lattices as a base for pore body and pore throat positioning. Pore bodies are situated at the grid vertices, while pore throats are distributed along the edges. Figure 3.1 (a) illustrates a regular network, with pore bodies in red and pore throats in blue. This example contains the utmost regular cubic network, with pore and throats populating all vertices and edges of the grid. Starting from such a topology, many adaptations can be implemented in order to improve the ability of synthetic networks to reproduce real porous media topology. One simple way to do so involves the random elimination of pore throats so that the coordination number – number of throats connected to each body – of the targeted porous medium is respected. Figure 3.1 (b) illustrates a synthetic pore network with randomly eliminated pore throats to reduce the coordination number from six – average of the cubic grid – to three – average for imaged Berea sandstone samples [5]. Additionally to topological adaptations, pore body and pore throat volumes in synthetic networks are also usually assigned following pore size distributions obtained from real porous media.

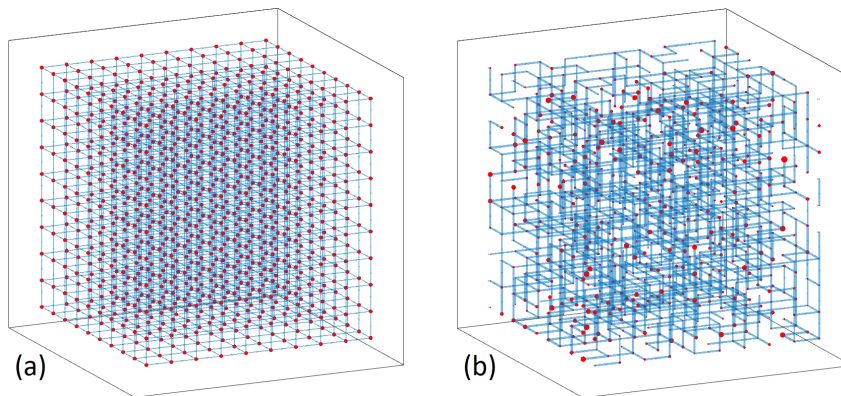


Figure 3.1: Networks based on a regular cubic lattice.

It is very difficult, however, to generate a network based on a regular lattice that honors complex geological porous media [50]. For this reason, alternatively to the construction of synthetic networks based in regular grids, some authors propose stochastic pore-network generation algorithms. As a result, networks with irregular topology are created, which could potentially represent more appropriately granular porous media. Examples of stochastic irregular pore-network generation methods are presented by Jiang *et al.* [52], Hyman and Winter [53], and Wang and Sheng [54].

3.2.1.2

Image based networks

Contrarily to the artificially created topology from synthetic networks, image based networks embody a topology extracted directly from images of the porous space. Due to recent growth in pore-scale imaging, this is the most popular approach to pore-network generation to date. Figure 3.2 illustrates pore-networks extracted from Micro-CT of a sandstone (A) and a carbonate (B) images by Dong [5].

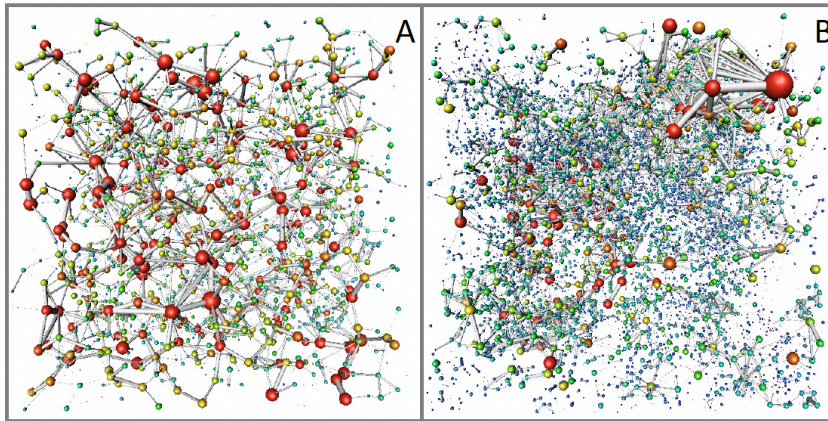


Figure 3.2: Image based networks generated by Dong [5]

The use of image based networks allowed a more reliable representation of porous media topological and morphological aspects and led, consequently, to a significant increase in pore-network modeling predictions. The use of networks extracted from images is especially important for the representation of flow through heterogeneous porous media, e.g. carbonate rocks, which are difficult to recreate using synthetic networks. There are several image based network extraction algorithm methods, focused on maintaining both the original pore space topology and morphology. Blunt *et al.* [23], Bultreys *et al.* [50] and Baychev *et al.* [55] provide comprehensive reviews of pore-network extraction methods, which are beyond the scope of this thesis.

3.2.2

Pore body and throat geometry

Pore-networks representing granular porous media have normally two different constitutive elements: pore bodies, which represent larger voids in porous space, and pore throats, which represent relatively constricted channels connecting larger voids. These elements should have simple enough geometries so that analytical and semi-analytical hydraulic conductances can be formulated. Commonly, cubes or spheres assume the role of pore bodies,

while straight capillaries with geometric cross-section substitute pore throats [24], as illustrated in Figure 3.3.

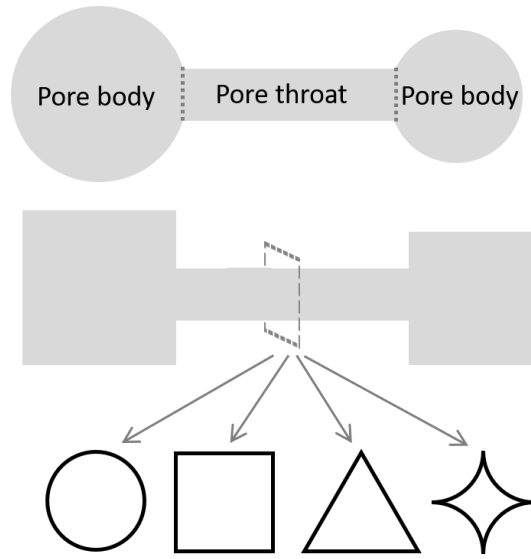


Figure 3.3: Pore body and pore throat geometries

The shapes chosen to represent pore bodies and throats impact significantly flow analysis conducted with pore-network models. The use of appropriate geometries for the flowing channels is fundamental even for the production of qualitative data pertaining to multiphase flow [24]. As an example, during simulations of conventional imbibition and drainage processes, e.g. water flooding in water-wet or oil-wet media, using circular cross-sections allow only one phase to flow in parallel in each element, while angular cross sections allow the reproduction of wetting phase corner flow, with the non-wetting phase flowing at the channel center. With that, the flow through wetting films can be accounted for and phase connectivity is more realistically modeled.

When pore-scale imaging of the studied porous medium is available, one generally used method for assigning shapes to pore bodies and throats involves the calculation of a shape parameter, G , expressed in Equation 3-1 [50]. According to the method, the shape parameter of the actual flowing channel and the geometric form chosen for its representation should be as close as possible.

$$G = \frac{A}{p^2} \quad (3-1)$$

where A is the channel cross-sectional area and p is the channel cross-sectional perimeter.

As a result of the impact of the geometric representation of pore bodies and throats, several models in the literature propose particular shape treatments for network construction. As examples, Ryazanov *et al.* [56] used pore

throats with n-cornered star shape cross section, while Joekar-Niasar and Hasanizadeh [57] considered pore bodies as truncated octahedrons. Alternatively, some models do not explicitly consider separate pore bodies and pore throats, and adopt pore elements with variable cross-section, as proposed by Valvanides *et al.* [58] and Al-Gharbi and Blunt [59]. As discussed in Chapter 4, the presented model for gas-condensate flow also adopts elements with variable cross-section, in order to benefit condensate blockage analysis.

3.2.2.1

Phase configuration in pores and throats

Once the network geometric aspects have been defined, the rules for phases distribution during multiphase flow can be stipulated. When two or more phases occupy a pore body or throat, several aspects, including saturation, wettability, flow channel shape and flow history, define phase spatial disposition. Figure 3.4 illustrates an example of two and three phase occupancy in a water-wet triangular pore throat cross-section. The leftmost triangle represents the pore throat filled with water, while the center triangle represents water and oil distributions, once oil invaded the water filled throat. Since the oil does not preferentially wet the channel walls, it can occupy most of the channel volume, but not displace water from the corners. Then, in case gas invades the pore throat, a configuration similar to the one illustrated in the rightmost triangle can take place. Compared to oil and water, gas tends to be the least wetting phase in a preferentially water-wet solid, and therefore, occupy the most central region in the throat. In this configuration, water flows in the corners, gas in the center and oil flows in films lodged between the most and least wetting phases [60].

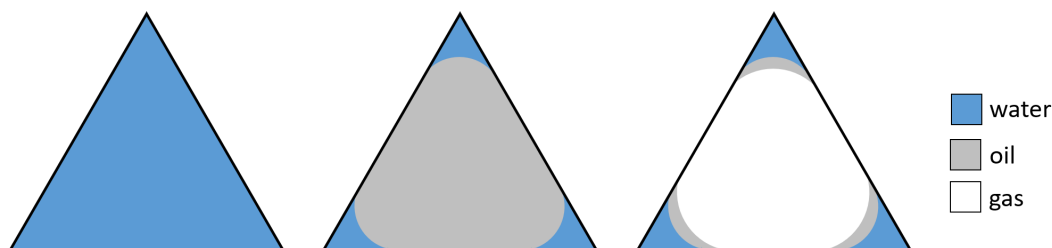


Figure 3.4: Example of phases configuration in a water-wet triangular pore throat cross-section.

Similarly complex phase distributions can also arise during two-phase flow, in case wettability alteration effects are taken into consideration. One of the key challenges with predictive modeling of flow through reservoir rocks is an

accurate characterization of wettability [60]. These effects, therefore, should be carefully implement in a pore-network model. Figure 3.5 illustrates an example of water and oil configurations, during a sequence of oil and water floodings, considering that prolonged contact with oil can alter the wettability from water to oil-wet. Figure 3.5 (a) and (b) depict the throat initially filled with water, and then filled with water and oil, following oil invasion in the reservoir. If configuration (b) is preserved long enough, the wettability of the oil touching walls can be altered, as indicated in Figure 3.5 (c), and the throat may develop a mixed wettability. Then, if water flooding is implemented to dislodge this oil, a configuration similar to the one depicted in Figure 3.5 (d) may arise, with oil flowing in films surrounded by water [60].

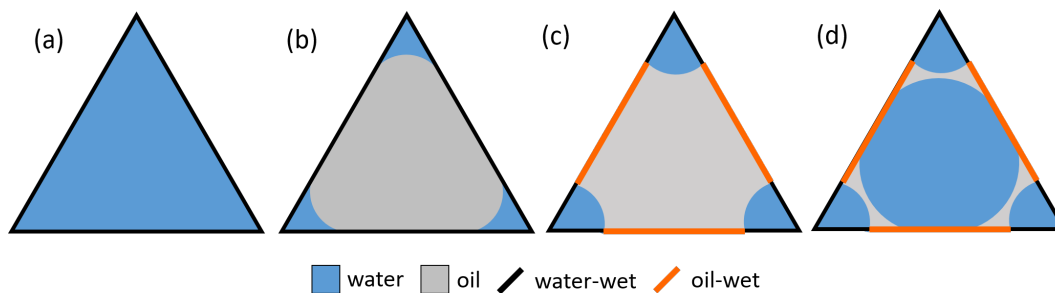


Figure 3.5: Example of phases configuration in a triangular pore throat cross-section, before and after wettability alteration from water to mixed-wet.

These two examples illustrate how complex gas/oil/water configurations can be represented in pore-network models, according to the porous medium wettability, morphology and sequence of phase invasions. Most of these phase distribution rules, however, do not apply to gas-condensate flow in reservoirs, as will be discussed in section 3.4. As a general rule, condensate wets completely the pore walls when compared to the gas phase (contact angle $\theta_{gc} \approx 0$), and emerges in the reservoir through filmwise condensation. In the absence of connate water, this leads to the formation of condensate wetting films directly on the pore walls. In the presence of irreducible water saturation, however, water tends to preferentially wet the rock, and condensate can form films deposited over the immobile aqueous phase [2]. Due to this particular phase formation and distribution, at pressures below the dew point pressure, both gas and condensate tend to be distributed and flowing concurrently at all pores [4]. As a consequence, wetting film formation and flow may not be driven mainly by capillary forces at pore corners. Thus, different rules for liquid phase distribution and flow must be devised for pore-network modeling of gas-condensate flow.

3.3

Pore-network modeling categories

Pore-network modeling algorithms can be divided into two main categories: quasi-static and dynamic [24]. Quasi-static models serve the purpose of representing capillary dominated flows, i.e. flows at low capillary number (eq. 2-2), while dynamic models are useful to analyze flow when viscous forces become significant. Brief explanations about the two pore-network modeling classes are presented in the next sections.

3.3.1

Quasi-static

In quasi-static modeling, the sequence of fluid invasion in the network is governed by the entry capillary pressure of pore throats connecting the pore bodies. During imbibition, smaller pore throats are invaded first, while in drainage bigger pore throats establish the preferential path for fluid invasion.

Since viscous forces are not taken into consideration in quasi-static models, the fluid motion is driven by discrete capillary pressure increments in the porous medium. During each increment, a single value of capillary pressure is assigned to all fluid-fluid interfaces contained in the network. As the capillary pressure is increased, given the current phase distribution in the space, quasi-static algorithms search for the available pore throats with low enough entry capillary pressure and move the invading fluid front past it. Pore bodies and throats filled with disconnected phases are not considered as available for fluid invasion, and these phases become trapped. For this reason, in the course of capillary pressure increase, it is important to move the invading fluid front one pore at a time, in ascending entry pressure order, as this affects the topology of trapped phases [50].

With this concept, quasi-static models provide predictive modeling of a variety of processes involving multiphase flow in porous media. By neglecting the influence of viscous forces on flow, however, this modeling approach becomes ill-suited to represent gas-condensate flow, as the important rate effects could not be predicted. For further information about quasi-static models and their applicability, a comprehensive review was published by Blunt [60].

3.3.2

Dynamic

When both viscous and capillary forces affect flow in porous media, dynamic pore network models become suitable for flow simulation. In this

case, fluid invasion at the pore-scale is controlled by the pore throats entry capillary pressure, while the time rate of invasion is a function of local viscous and capillary forces [24].

Instead of updating phase configurations based in increments of capillary pressure, dynamic model algorithms solve system of equations relating the pressure and the saturations at each pore, while pressure and/or flow rate are imposed at the network boundaries. Therefore, more complex coding and robust solution methods are required for dynamic models, when compared to quasi-static models [24].

With dynamic models, several interesting rate dependent effects on flow through porous media can be modeled, e.g. mobilization of trapped ganglia and capillary number influence on relative permeability curves. For this reason, predictive pore-network models for gas condensate flow usually fall within this category. In the next section, a review of pore-network models developed specifically to represent gas-condensate flow is presented. For other applications of dynamic models, as well as details of commonly implemented algorithms, Joekar-Niasar and Hassanizadeh [24] presented an extensive review on two-phase flow dynamic pore-network modeling.

3.4

Pore-network modeling of gas-condensate flow

A few pore-network models have been proposed in the literature addressing the representation of gas and condensate flow. Both quasi-static and dynamic models have been developed aiming primarily the prediction of condensate critical saturation and relative permeability curves. An overview of these models is presented next.

Mohammadi *et al.* [6] developed in 1990 the first pore-network model specifically designed to represent gas-condensate flow. In their model, which belonged to the quasi-static category, Bethe trees (Fig. 3.6) were used to reproduce porous media, where only the tree bonds contributed to the flow and the junctions were volumeless. These bonds had convex polyhedral cross-sections and their size was defined using a Rayleigh probability density function calibrated to represent a rock sample pore size distribution.

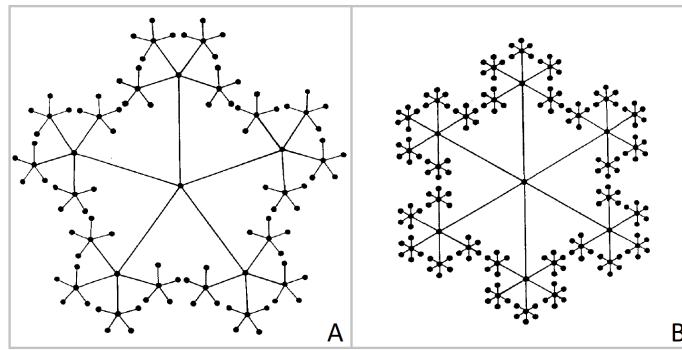


Figure 3.6: Bethe tree porous medium representation used by Mohammadi *et al.* [6]

Using the liquid dropout curve of a gas-condensate mixture as reference, Mohammadi *et al.* simulated condensation in their model by progressively lowering the pressure in the networks and changing liquid saturation so that the liquid dropout as a function of pressure was satisfied. Therefore, condensate saturation in the network increased until the pressure of maximum liquid dropout was reached, and further depletion led to re-vaporization in the network. Gas and condensate menisci had the same radius everywhere in the network, and this radius defined whether a bond would be completely filled with liquid – meniscus radius lower than bond radius – or just the bond corners would be filled with liquid – meniscus radius greater than bond radius. During condensation, the condensate critical saturation was achieved when the liquid reached the percolation threshold. When the process of re-vaporization began, only the liquid accessible to the gas could vaporize. In the whole process, the phases properties were considered constant.

Relative permeabilities were calculated using percolation theory, and the effects of rate could not be appraised. The gas relative permeability curves predicted by the model resembled closely those of the non-wetting phase during conventional imbibition processes, while the condensate relative permeability curves were similar to the wetting phase curves during imbibition, only shifted in the direction of greater liquid saturation. A series of sensibility evaluations of the relative permeability curves to geometric aspects, e.g. coordination number, geometric shape of bonds cross-sections and pore size distribution, were also performed by the authors. However, while the model was innovative for its time, since a way to represent condensate formation in situ was presented, major modeling simplifications make its relative permeability predictions unreliable.

Six years later, Fang *et al.* [7] devised a pore-network model for condensate critical saturation under gravitational effects. In their model, porous media

was represented by a regular two-dimensional network of cylindrical capillaries with constant cross-section, constructed based on a square grid. All capillaries had the same length, $6000\mu m$, and a radius according to a log-normal size distribution, with average radius equal to $23.06\mu m$ and standard deviation of 5.74. Condensation was modeled by adding, to each capillary with radius below the threshold radius $r_t = 20\mu m$, a volume of $200\mu m^3$ of liquid at each time step. The liquid appeared in the form of a slug, as illustrated in Figure 3.7.

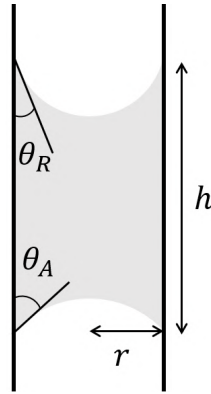


Figure 3.7: Advancing and receding interfaces of a condensate bridge accommodated at a circular capillary. Adapted from Fang *et al.* [7]

In vertical capillaries, the slug weight could be equilibrated by capillary forces considering that advancing and receding contact angles were different. In the absence of viscous forces, the maximum height of a condensate slug equilibrated in each capillary was calculated with Equation 3-2.

$$h_{max} = \frac{2\sigma}{\Delta\rho gr} (\cos\theta_R - \cos\theta_A) \quad (3-2)$$

where h_{max} is the maximum liquid slug height, θ_A is the advancing contact angle, θ_R is the receding contact angle, $\Delta\rho$ is the density difference between condensate and gas, σ is the interfacial tension, r is the capillary radius and g is the gravitational acceleration.

As the amount of liquid in a capillary produced a slug which exceeded h_{max} , the condensate flowed down and a series of rules were devised by the authors to redistribute the condensate once the it met the capillaries intersections. In horizontal capillaries, the condensate slug could grow until the capillary was completely filled.

With the increments of liquid volume at each step in the small enough capillaries, the critical condensate saturation was achieved once condensate started being produced from the network lower boundary. With the model, the sensibilities of S_{cc} to interfacial tension and contact angle hysteresis were evaluated. The authors found that S_{cc} increases with surface tension, and that

contact angle hysteresis between 0° and 10° affect significantly the S_{cc} , while values between 10° and 30° only affected the critical condensate saturation marginally.

In 1999, Wang and Mohanty [8] also devised a model for condensate critical saturation. They represented the porous media as three dimensional networks of pore bodies connected by converging-diverging pore throats. Two different geometries for the networks were tested: the first based on the void space of a sphere-pack, and the second based on a cubic regular grid of cubic pore bodies connected by bi-pyramidal pore throats with square cross-section (labeled cubic model). Figure 3.8 illustrates the longitudinal cut of two pore bodies connected by a pore-throat, in the cubic model.

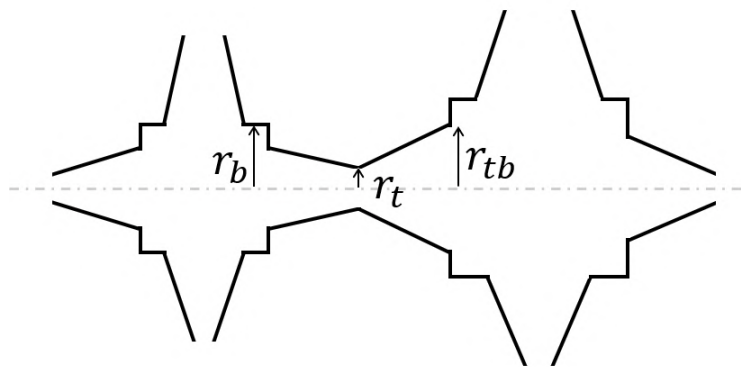


Figure 3.8: Cubic pore bodies connected by converging-diverging pore throats with square cross-section used to represent porous media. Adapted from Wang and Mohanty[8]

The model proposed by Wang and Mohanty was based on phase trapping and accumulation of liquid at pore corners, without considering contact angle hysteresis. Condensate slugs could be accommodated at vertical pore throats by capillary forces given their converging-diverging profile. In the sphere-pack model, each pore body was connected to six pore throats, while each pore throat had four corners, each of which connected to three other pore throats. This connectivity between pore throats, unconventional in pore network modeling, is illustrated in Figure 3.9. As for the cubic model, each pore body was connected to six pore throats, each of which communicated only to pore-bodies at its extremities. For both models, the pore body sizes were assigned using a Weibull probability density function representing the pore size distribution of a Berea sample.

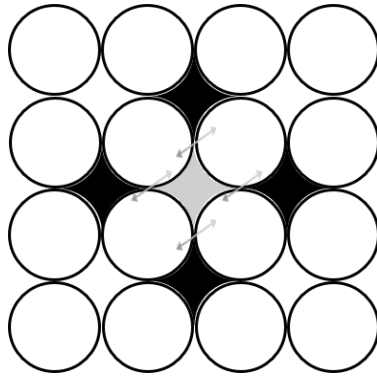


Figure 3.9: Pore-throat connectivity in the sphere-pack model used by Wang and Mohanty[8]. The gray pore throat is connected by its corners to the pore throats depicted in black, plus eight pore throats in the planes outside the figure, indicated by the arrows.

Condensation was modeled with a procedure similar to that used by Mohammadi *et al.* [6], by adding liquid at pore corners or the entire pore body/throat, according to a threshold radius. As the pressure in the network was depleted, this threshold radius increased and more pores could be filled with condensate. During condensate accumulation, the condensate slugs at adjacent pore bodies and throats could form ganglia equilibrated between capillary and gravitational forces, similar to the proposed by Fang *et al.* [7]. When the maximum ganglion size that could be equilibrated by capillary forces was formed in the network, the S_{cc} was achieved. Connate water could also be present in their model, and it was considered that the pores would be preferentially water-wet. In this case, water would fill the smaller pores and pore corners and condensate would be formed on top of the immobile aqueous phase.

With both cubic and sphere-pack models, the authors calculated the sensitivity of S_{cc} to interfacial tension, initial water content and geometric aspects, as the coordination number, pore sizes and the parameter defining the radius connecting pore bodies to pore throats (r_{tb} in Fig. 3.8). With the sphere-pack model, critical condensate saturations below 10% were calculated, while in the cubic model this value could be as high as 45%. This difference is attributed to the high connectivity between pore elements in the sphere pack model, which facilitated the formation of a big enough ganglion to flow. By comparing these results to usual S_{cc} values obtained experimentally with rock samples, the authors considered that the sphere-pack model enhanced connectivity could not be adequate to represent geological porous media, while the cubic-model was more realistic.

In the following year, Wang and Mohanty [9] expanded their model to include viscous and inertial effects. With the new model, non-Darcy flow coefficients and relative permeability curves for gas and condensate were predicted. The authors considered that condensate could flow in porous media due to three mechanisms: pressure gradient within a continuous condensate phase, movement of condensate slugs and condensate droplets carried by the gas. The first mechanism would take place at low capillary numbers, where capillary forces dominate. The second would take place when viscous become more significant and disconnected condensate ganglia become able to move. The third would happen at high Reynolds numbers and low condensate saturations, when condensate droplets could be carried by the gas. In their new dynamic model, Wang and Mohanty modeled only the first and third mechanisms, in separate models, leaving a gap of flowing conditions in gas-condensate reservoirs uncovered in the study.

The porous media was represented by the cubic model described in their previous work [8] and the condensation mechanism was also replicated from it. During the first regime, labeled as "low N_c flow regime", the condensate saturation increased at each time step by lowering the pressure in the network and increasing the threshold radius for condensate occupancy. Then, a small pressure drop was applied in the gas phase across the network and the continuity equation was solved for each pore body, giving the pressure field in the network and flow rate. With these data, gas relative permeability was calculated using the Darcy's law and the absolute permeability of the network. A similar procedure was repeated for the condensate phase, but considering only the mobile liquid ganglia. During the second analyzed regime, labeled as "low condensate saturation / high pressure gradient flow regime", the initial liquid distribution was also determined based on the network pressure and associated threshold radius for condensate occupancy. Then, a large pressure drop was applied in the gas phase and the pressure distribution in the network was calculated, taking into consideration the inertial flow in converging diverging and bending flow sections. With this pressure distribution, some condensate slugs in the network could not be equilibrated by capillary forces, and were converted into small droplets carried by the gas, as illustrated in Figure 3.10, in the Type II droplet formation. Condensate droplets could also be formed in pore throats without a condensate slug, as illustrated in Figure 3.10, in the Type I droplet formation. In this case, if the gas velocity was high enough, condensate droplets could be ripped apart from the condensate accumulated at the throat corners. For both cases, a series of rules for condensate droplet radius, flow rate and interception at pore walls

was devised in the model. In this flow regime, the relative permeabilities of both phases and the non-Darcy coefficients were calculated.

It was found that, at the low N_c flow regime, relative permeabilities depended strongly on pore structure, as it affects directly the paths through which sample spanning phases flow under their own pressure gradients. At the low condensate saturation / high pressure gradient flow regime, which considered only condensate saturations below 20%, with initial water saturation of 8%, relative permeabilities of both phases increased with the pressure gradient, showing that, for the evaluated flow conditions, the positive coupling influence on flow exceeded the negative non-Darcy effects.

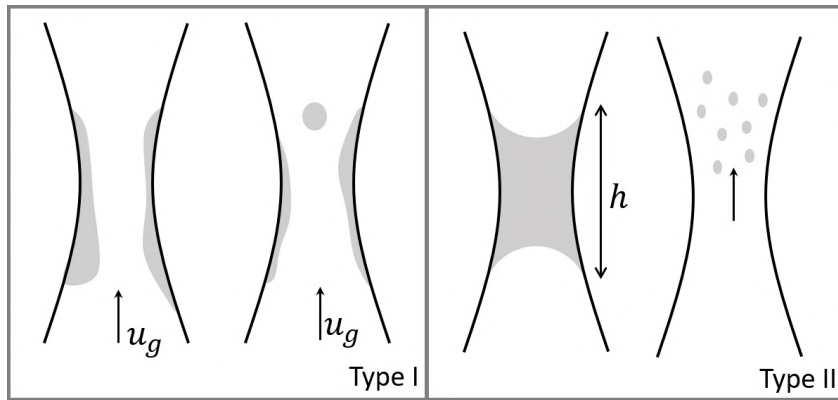


Figure 3.10: Mechanisms of condensate droplet formation during low liquid saturation high capillary number flow, proposed by Wang and Mohanty[9]

Also in 2000, Li and Firoozabadi [61] extended the model presented by Fang *et al.* [7] to include viscous effects. They kept the original model's network, with circular capillaries in a square grid, and the condensation mode, with slugs of condensate created at each time step in the capillaries with radius inferior than $20\mu m$. The maximum slug height in a vertical capillary was adapted from Equation 3-2 to the Equation 3-3, by including the pressures acting in the receding and advancing meniscii, P_R and P_A , respectively.

$$h_{max} = \frac{2\sigma}{\Delta\rho gr} (\cos\theta_R - \cos\theta_A) - \frac{P_R - P_A}{\Delta\rho g} \quad (3-3)$$

In order to calculate the relative permeabilities, the authors defined conditions for gas and condensate flow in the circular capillaries. Gas could flow in gas filled capillaries and in capillaries with a condensate slug, when h_{max} was exceeded. Condensate flowed only as a result of a slug reaching h_{max} . Capillaries holding a slug with height lower than h_{max} were blocked to flow. Based on these conditions, conductances for both phases were calculated for each capillary in the network, and updated at every time step, according to local saturations. Once the conductances were calculated, the relative

permeabilities were estimated using the renormalization method. The effects of gravity, viscous forces, interfacial tension and wettability on the curves were analyzed. The results indicated that gravity effects are significant only at low interfacial tension and under small viscous forces. The estimated effects of viscous forces and interfacial tension on relative permeabilities were in line, qualitatively, with experimental data. The findings also suggested that altering the porous medium wettability towards a preferentially gas-wet state could improve the gas relative permeabilities significantly.

A pore-scale model for the coupled flow of gas and condensate in a single pore was also developed in 2000 by Jamiolahmady *et al.* [4]. Based on micromodel visualizations of gas and condensate flow in porous media, presented in the same study (discussed on Section 2.3.1), the authors developed a model for flow in a converging diverging conical pore including two flow regimes. The two regimes, labeled as "open half cycle" and "closed half cycle", characterized the opening and closing of condensate bridges that cyclically obstructed the movement of gas through flowing channels. The two cycles are illustrated in Figure 3.11. In the proposed model, both gas and condensate were injected in the pore at constant flow rate, while the outlet condensate pressure was fixed, and the outlet gas pressure was calculated using the local capillary pressure. In the open half cycle, the model main feature was the evolution equation that predicted the thickness of the condensate film, bounded by R_i – the interface radius – shown in Figure 3.11. During this cycle, an imbalance in the capillary pressure along the liquid film leads to the accumulation of condensate around the pore constriction which eventually causes the closing of the gas passage. This marks the beginning of the closed half cycle, in which gas pressure builds up until gas can open its way through the liquid. In this cycle, an equation determines the position of the hemispherical gas front, x^{he} , pushing the condensate out of the constriction. By coupling the solution of the two cycles, the authors determined an pseudo steady-state two-phase flow, in which both cycles repeated themselves periodically. The solution depended on the pore geometry, injection rates, phases properties and interfacial tension.

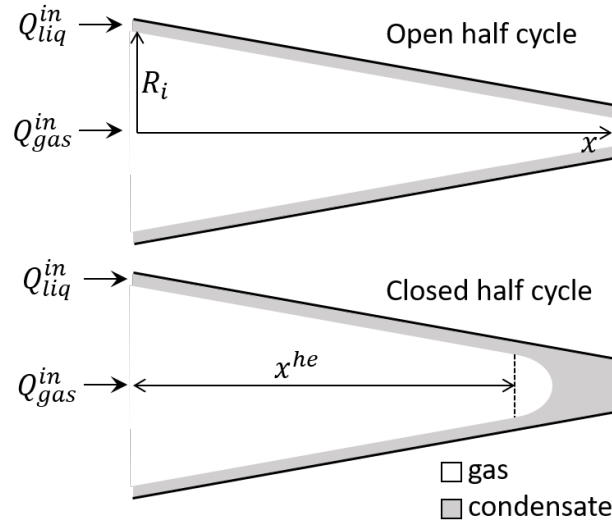


Figure 3.11: Open and closed half cycles used to model the coupled flow of gas and condensate through pores, proposed by Jamiolahmady *et al.* [4].

This single pore model was then used, in 2003, to calibrate a 3D pore-network for gas-condensate flow, by the same authors [16]. In the pore-network model, a regular cubic lattice of pore elements with converging diverging shape was created. There was no distinction between pore bodies and pore throats, as the pore elements accounted for both. The regular pore lattice was adapted to represent the pore space of a Berea sample used in the same study in gas-condensate core flooding experiments. To achieve this objective, the radius of the pore constrictions was defined based on a Weibull probability density function of pore sizes of a Berea sample. Then, to generate an average coordination number of three, appropriate to represent the sample, pore elements were randomly removed from the cubic lattice. Using the generated network, a quasi-static algorithm was implemented and a capillary pressure vs. saturation curve was generated, for comparison with the curve obtained experimentally. In order to match experimental and numerical curves, the authors had to define the pore element lengths with the correlation presented in Equation 3-4, where L_0 is a constant. This correlation leads to longer pores with small radii and vice-versa, which is unlikely to be realistic.

$$L_{pore} = L_0 R^{-1.5} \quad (3-4)$$

where L_{pore} is the pore element length, L_0 is an arbitrary constant and R is the pore element radius.

With the pore-network geometry defined, a dynamic algorithm for gas-condensate flow was implemented. In this algorithm, the condensate film evolution equation used in the single pore model [4] could not be used, as

the resulting computational effort would be excessive. For this reason, two correlations, one for the condensate initial thickness in a pore, h_{ini}^{ss} , and the other for the time required for the condensate lens formation t_{ev} , were fitted based on the results obtained with the single pore model, using a broad range of parameters. These correlations are expressed in Equations 3-5 and 3-6, respectively.

$$\frac{h_{ini}^{ss}}{R^{in}} = 0.675C_m \left(\frac{R^{out}}{R^{in}} \right)^{0.488} \left(\frac{L}{R^{in}} \right)^{0.208} \left(\frac{\mu_l v_T^{in}}{\sigma} \right)^{0.234} CGR^{0.237} \quad (3-5)$$

$$t_{ev} = 0.387 \left(\frac{R^{out}}{R^{in}} \right)^{5.632} \left(\frac{L}{R^{in}} \right)^{0.410} \left(\frac{\mu_l R^{in}}{\sigma} \right) \left(\frac{h_{ini}}{R^{in}} \right)^{-4.538} \quad (3-6)$$

where h_{ini}^{ss} is the initial condensate thickness in a pore, C_m is a multiple pore coefficient, used to correct the correlation developed using a single pore, to a pore-network, R^{in} is the radius at the pore inlet, R^{out} is the radius at the pore constriction, L is the pore length, μ_l is the liquid viscosity, v_T^{in} is the total velocity of the fluids entering the pore, σ is the interfacial tension, CGR is the condensate gas ratio injected in the pore, t_{ev} is the time required for a condensate bridge to be formed in the pore.

With the equations for the thickness of condensate film and time required for condensate lens formation, it is possible to define, at each simulation time step, which pores are opened and which have achieved the temporal requisite to close. After the lens formation, the pore remained closed to the gas flow until the pressure drop in the pore exceeded the pore entry capillary pressure. To obtain the pressure distribution in the network, viscous pressure drop equations for the gas in open pores and the condensate in both open and condensate filled pores are solved, enforcing mass conservation at the pore intersections in the network. These equations, shown in Eq. 3-7 and 3-8, were based on the Poiseuille law, using the concept of equivalent length to account for extra energy loss in real porous media due to irregular pore shapes, tortuosity and pore wall roughness, which are not represented in the pore-network. The parameters C_b and C_f are adjusted by matching experimental and numerical pressure gradients, given a fixed flow rate for gas and condensate.

$$Q_{bulk} = \frac{\pi}{8\mu} \left(\frac{-\Delta P}{L + C_b D/64} \right) R^4 \quad (3-7)$$

$$Q_{film} = \frac{2\pi}{3\mu} \left(\frac{-\Delta P}{L + C_f h/6} \right) R h^3 \quad (3-8)$$

where Q_{bulk} is the volumetric flow rate at the fluid bulk, Q_{film} is the volumetric flow rate at the fluid film, C_b is the minor loss coefficient for the laminar flow of the fluid bulk, C_f is the minor loss coefficient for the laminar flow of the

fluid film, R is the pore radius, D is the pore diameter, L is the pore length, μ is the viscosity, h is the condensate film thickness and ΔP is the pressure drop in the pore element.

The validation of the model was carried out by trying to match relative permeability curves obtained experimentally, using a Berea sample and a methane n-butane mixture, at two values of interfacial tension – 0.015 and 0.037mN/m – and three values of gas flowing velocity – 9, 18 and 37m/day. During the validation, the coefficients C_b and C_f were adjusted based on the curves for the lowest flowing velocity and interfacial tension, and kept constant for the other cases. The model could predict reasonably well the curves obtained at 0.015mN/m for all flowing velocities, but did not lead to quantitatively good results for the curves at 0.037mN/m. In all cases, the effects of velocity and interfacial tension on the relative permeability curves were well represented qualitatively.

In 2003, Bustos and Toledo [10] developed a model for gas-condensate flow under gravitational forces, using two and three dimensional pore networks. Their model was constructed based on the model presented by Fang *et al.* [7], with the main implemented improvements being the use of polygonal capillary cross-sections, expansion from 2D to 3D networks, and the calculation of relative permeabilities. In their model, porous media could be represented by regular 2D square lattices or regular 3D cubic lattices of capillaries with square cross-section. The use of a polygonal cross section allowed the representation of condensate accumulation in pore corners and, consequently, different two-phase flow regimes. The condensation was still represented by discrete additions of liquid at the capillaries, and all pore segments in the network received the same volume of liquid, at each time step, as illustrated in Figure 3.12.

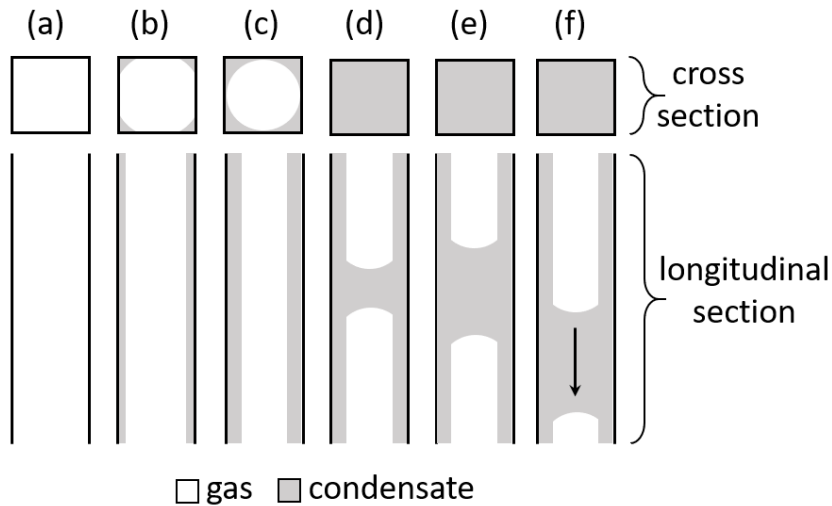


Figure 3.12: Sequence of condensation in a square vertical capillary, proposed by Bustos and Toledo [10]

Figure 3.12(a) represents a capillary filled with gas, and Figure 3.12(b) represents the same capillary, at an early stage of condensate formation. The liquid is contained at pore corners and the center of the pore remains open to gas flow. This two-phase distribution lasts until the configuration shown in Figure 3.12(c) is reached. In this case, the condensate menisci become contiguous and the gas loses contact with the capillary walls. Under this configuration the phases achieved the snap-off capillary pressure and a bridge of condensate is formed in, as shown in Figure 3.12(d). Similarly to the work of Fang *et al.* [7], in a vertical capillary, the condensate bridge can be equilibrated between capillary and gravitational forces, by assuming contact angle hysteresis. Then the bridge can grow, as shown in Figure 3.12(e), until the maximum height is achieved (Eq. 3-2) and the condensate flows down (Fig. 3.12(f)). In horizontal capillaries, the formed condensate bridge grows until the whole capillary is filled.

With the possible phase distributions in the square capillaries characterized, the authors defined the corresponding hydraulic conductances for gas and condensate. The conductances of gas and condensate for gas filled capillaries with condensate at corners (as in Figures 3.12 (b) and (c)) were calculated following the works of Blunt [62] and Hughes and Blunt [63]. The work of Blunt [62] was also used to define the condensate conductance for capillaries fully saturated with liquid. For the capillaries with a moving condensate bridge, i.e. for capillaries in which gravitational forces overcame capillary forces and the condensate bridge flows down, as in Figure 3.12 (f), the conductances were estimated by dividing the capillary in regions and calculating

the total flow resistance as a series of these regions' resistances. Figure 3.13 illustrates the capillary partition into two lengths containing condensate in wedges, l_{w1} and l_{w2} , and a length containing condensate as the bulk phase, l_b . For the gas conductance calculation, separate conductances were calculated for the lengths l_{w1} and l_{w2} , and the total gas conductance was defined as $g_{gas} = (g_{gas}^{w1} \times g_{gas}^{w2}) / (g_{gas}^{w1} + g_{gas}^{w2})$. As for the condensate conductance calculation, first conductances were calculated for the three lengths. Then, the conductances for the lengths l_{w1} and l_{w2} were added ($g_{liq}^w = g_{liq}^{w1} + g_{liq}^{w2}$) and the total condensate conductance was defined as $g_{liq} = (g_{liq}^w \times g_{liq}^b) / (g_{liq}^w + g_{liq}^b)$.

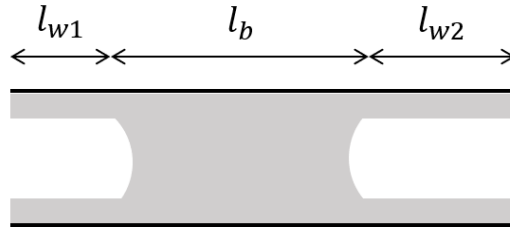


Figure 3.13: Partition of capillary regions suggested by Bustos and Toledo [10] for conductance calculation

Once the fluids conductances are determined, the pressure distribution and flow rates in the network are calculated by performing a material balance at each capillary intersection in the network. Then, relative permeabilities are predicted with the Darcy's law. Comparison between results obtained with 2D and 3D networks indicated that relative permeabilities for gas are much higher in 3D than in 2D networks. The same effect was observed on condensate relative permeabilities, but to a lower degree. This suggests that gas-condensate flow predictions based on two-dimensional pore-network models may be underestimated. Relative permeability curves obtained with 3D networks with different pore size distributions were also compared. For networks with the same average pore radius, broader pore size distributions led to lower relative permeabilities for gas and condensate, using both uniform and normal distributions. The authors also remarked that the gas relative permeability curves, for all cases analyzed, displayed overall the same inverted-S shape. At low condensate saturations, gas relative permeabilities were reduced gradually, as the condensate was mostly held at pore corners, thus not obstructing significantly the gas flow. At intermediate condensate saturations, gas relative permeabilities decreased abruptly, as a result of the formation of condensate bridges and the consequent blockage of gas flow. Then, at high condensate saturations, near the percolation threshold of sample-spanning gas paths, the pace of gas relative permeability decrease diminished.

In 2017, Momeni *et al.* [64] developed a pore-network model for gas-condensate flow in which gas and condensate saturations were determined using phase equilibrium calculations. Regular three dimensional cubic lattices of square capillaries were used to represent porous media, similarly to the proposed by Bustos and Toledo [10]. Gas and condensate could assume, however, only two different configurations in each capillary. At capillary pressures below the snap-off capillary pressure (Figure 3.12(c)), condensate was accumulated in wedges located at capillary corners. Then, further increase in condensate saturation would lead to the snap-off of the gas phase, and the capillary would become fully saturated with liquid. Therefore, unlike the work of Bustos and Toledo [10], in which the liquid saturation still increased gradually after the snap-off, in the model proposed by Momeni *et al.*, a shift from the liquid snap-off saturation, ($S_l^{so} \approx 21.46\%$, calculated with the area occupied by condensate in the capillary cross-section, at the snap-off capillary pressure) to a liquid saturation of 100% occurs. At the two possible phase configurations, the conductances were calculated with the same equations adopted by Bustos and Toledo [10].

During the flow simulations, volumetric flow rates for both phases were imposed at the network inlet, and pressure was imposed at the network outlet. Separate pressure distributions were calculated for the gas and the condensate, but the pressure boundary condition at the outlet was equivalent for both phases. In order to determine the pressure distributions at each simulation time step, first, the phases compositions and saturations were defined by performing a flash calculation at each capillary. With the saturations, the phases configurations were updated and conductances calculated. Then, mass balance for each phase at each capillary intersection was enforced, and the pressure distributions determined. Finally, relative permeabilities were estimated by applying the Darcy's law for each phase.

Although the idea of performing flash calculations to determine the phases properties is appropriate for gas-condensate flow numerical analyses, as mass transfer between the phases is ubiquitous in this type of reservoir, the pore-network model proposed by Momeni *et al.* has several shortcomings. First, the phase equilibrium calculations are performed completely decoupled from the equations to determine the pressure fields. Second, the equations used to determine the pressure distributions involve mass balance, not molar balance. Hence, if the phases compositions shift during the flow, this procedure does not ensure molar conservation. Third, the system of equations used to determine gas and condensate pressure distributions do not include the restriction $P_{gas} = P_{liq} + P_c$ at each throat. Finally, it is not clear how the

procedure to fill the capillaries with condensate after the snap-off takes place, since the local phases saturations are defined with flash calculations.

An inconsistency was also identified in the model validation presented by Momeni *et al.*. They compared the relative permeability curves obtained with their model with the experimental curves presented by Jamiolahmady *et al.* [16], for gas-condensate flow through a Berea sample, at an interfacial tension of 0.037mN/m and a gas flowing velocity of 18m/day . In the experimental work, the curves were generated at steady-state flow, meaning that each point ($k_r(S_g)$) of the curves was obtained with different ratios between injected condensate and injected gas flow rates (CGR). The numerical curves, however, were obtained at unsteady-flow, during the accumulation of condensate in the porous medium with an imposed CGR of 0.1. As for the effects of flow rate and interfacial tension in the curves, they were observed in the results obtained with the model, but not compared to experimental data.

In 2020, Santos and Carvalho [11] developed a fully implicit compositional pore-network model for gas-condensate flow. In this model, a robust compositional formulation, based on the model for reservoir-scale simulation proposed by Collins *et al.* [65], was used. Therefore, the inconsistencies between phase equilibrium calculations and transport equations present in the model proposed by Momeni *et al.* [64] were avoided.

In this model, the porous medium was represented by two dimensional networks of cylindrical capillaries. At pressure above the dew point pressure, only gas occupied the capillaries and the single-phase flow conductances were calculated with the Poiseuille law. At pressures below the dew point pressure, the formed condensate was accommodated at films flowing at the capillary walls. In this case, conductances for both gas and condensate were formulated based on the solution of the Navier Stokes equations for steady-state laminar core-annular flow, as shown in Equations 3-9 and 3-10. This allows the shear stress tie and the velocity continuity at the phases interfaces, which is not honored in the previously mentioned pore-network models for gas-condensate flow, except for the single pore model presented by Jamiolahmady *et al.* [4].

$$g_g = \frac{\pi}{8\mu_g L} R_{int}^4 + \frac{\pi}{4\mu_l L} R_{int}^2 (R^2 - R_{int}^2) \quad (3-9)$$

$$g_l = \frac{\pi}{8\mu_l L} (R^2 - R_{int}^2)^2 \quad (3-10)$$

where g_g is the conductance of the gas phase, μ_g is the gas viscosity, L is the capillary length, R is the capillary radius, R_{int} is the radius of the interface between gas and liquid, g_l is the conductance of the liquid phase and μ_l is the liquid viscosity.

With the conductances defined, the number of moles of each component in the flowing mixture and the pressure at the pores, defined as the control volumes involving the half the volume of the capillaries at each capillary intersection (Fig. 3.14) could be calculated. For the pores at the network inlet and outlet, source/sink terms were also included in the model variables. The system of non linear equations relating the model variables comprises molar balance equations and volume consistency equations for all pores, and equations to enforce the boundary conditions. This system was solved with the Newton-Raphson method, while the phase-equilibrium calculations used the Peng-Robinson [25] equation of state.

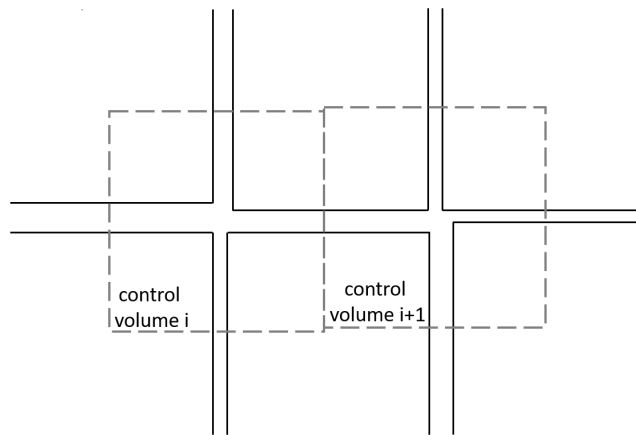


Figure 3.14: Control volumes used to calculate the variables in the model proposed by Santos and Carvalho [11]

While the compositional formulation of the model proposed by Santos and Carvalho was properly developed, the two-phase flow regimes lack representativeness for gas-condensate flow in porous media. The occurrence of the snap-off of the gas phase, which leads to condensate bridge formation and hindrance of gas flow, was not included in the formulation. For this reason, condensate blockage and the effects of flow rate and interfacial tension could not be represented in the model results.

As presented in this section, although several pore-network models for gas-condensate flow were developed in the past 25 years, no model represents accurately both the condensation process and the two-phase flow patterns developed by gas and condensate in porous media. In this context, the goal of this thesis is the advancement in predictivity of pore-network modeling of gas-condensate flows. The model proposed here, discussed in the next chapter, is built upon the work of Santos and Carvalho [11]. The robust compositional formulation presented in the base model was kept, while more realistic flow patterns and porous media representation were implemented.

4

Proposed pore-network model

In this chapter, the mathematical formulation of the proposed pore-network model for gas-condensate flow is presented. First, a list of the model general assumptions is presented in Section 4.1. Then, the adopted pore-networks are discussed in Section 4.2. Section 4.3 presents the phases configurations and flow patterns in the porous space. The equations governing the flow of gas and condensate through the networks are described in Section 4.4. Finally, the phase equilibrium calculations are explained in Section 4.5.

4.1

Model Assumptions

For the development of the pore-network model for gas condensate flow described in this chapter, the following list of assumptions was adopted:

- Constant temperature
- Local thermodynamic equilibrium
- Slightly compressible porous medium
- Absence of water
- Negligible gravitational effects
- Negligible inertial effects

4.2

Pore-network description

The pore-networks used in the proposed model consist of three-dimensional structures of circular converging-diverging capillaries. As an extension to the model presented by Santos and Carvalho [11], in which the pore-networks were composed by straight circular capillaries, constricted capillaries were adopted to incorporate the physical phenomena associated with condensate bridge formation and removal into the model. By employing flow channels with variable cross-section, more precise estimates of the geometrical conditions leading to the snap-off of the gas can be made. Moreover, it improves the calculation of the capillary pressure threshold to reestablish gas

flow after the snap-off. Descriptions of the pore-space as a bundle of converging-diverging flow channels were also adopted by Wang and Mohanty, [8, 9] and Jamiolahmady *et al.* [4, 16] to model gas-condensate flow.

As mentioned in Chapter 3, by constructing a pore-network using elements with variable cross-section, the necessity to define separate pore bodies and pore throats is exempt. In our case, the constricted portion of the capillaries serve as the pore throats, while the unconstricted regions serve as pore bodies. For the mathematical formulation, however, the networks were partitioned into nodes, identified by the index i , and edges, identified by the index j , as illustrated in Figure 4.1.

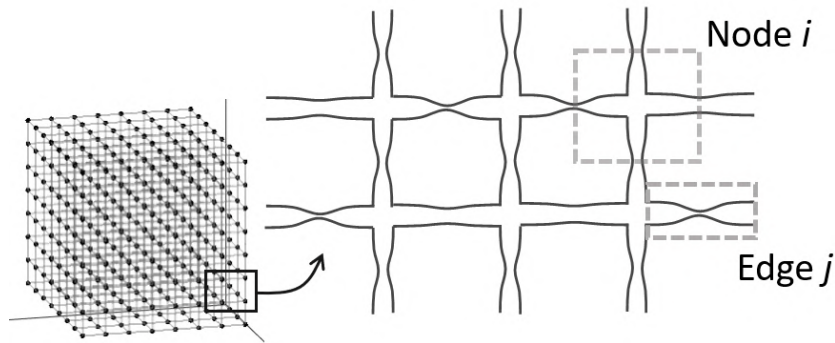


Figure 4.1: Definition of nodes and edges in the proposed model

Each edge corresponds to one of the converging-diverging capillaries composing the network. They are characterized by the hyperbolic profile presented in Equation 4-1, in which L_j is the capillary length, $R_{max,j}$ is the capillary unconstricted radius and $R_{min,j}$ is the constricted radius. This profile is illustrated in Figure 4.2.

$$r_j(x) = \sqrt{a_j + b_j x^2} \quad (4-1a)$$

$$a_j = R_{min,j}^2 \quad (4-1b)$$

$$b_j = \left(\frac{2}{L_j}\right)^2 (R_{max,j}^2 - R_{min,j}^2) \quad (4-1c)$$

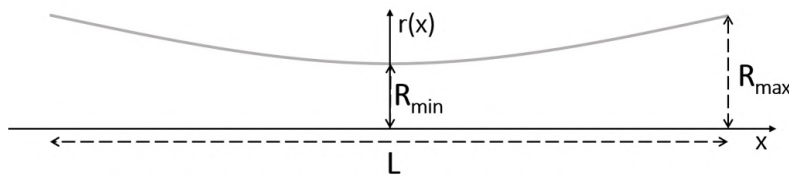


Figure 4.2: Converging-diverging capillary profile

The nodes are centered at the capillaries intersections. A control volume is defined for each node, enclosing the intersection volume plus half the volume of the capillaries connected to it. As further discussed in Section 4.4, the control volumes of the nodes define the points at which the model variables are calculated, while the geometry associated with each edge define the transport between the nodes. The connectivity between nodes and edges is mapped by an incidence matrix, \mathbf{C} , with elements defined as follows:

$$c_{ij} = \begin{cases} 0 & , \text{ if the edge } j \text{ is not connected to the node } i \\ -1 & , \text{ if the edge } j \text{ enters the node } i \\ +1 & , \text{ if the edge } j \text{ exits the node } i \end{cases}$$

In the proposed model, there are no restrictions related to the network topology. Therefore, networks can be defined based on 3D pore-scale imaging of real rock samples, or be constructed on regular lattices, using appropriate pore size distributions and coordination numbers.

4.3

Two-phase flow in capillaries

In order to quantify the transport between the nodes, gas and condensate flow patterns in the capillaries must be characterized and modeled. In the next section, a qualitative description of the condensate dropout and gas-condensate flow mechanisms implemented in the model is presented. In the subsequent section, the equations used to quantify the transport of the two phases between nodes are explained.

4.3.1

Flow Patterns Overview

For a gas condensate reservoir, the flow at pressures above the dew point pressure (P_{dp}) contains only the gas phase (Fig.4.3a). If the pressure level is lowered below the P_{dp} , however, a liquid phase emerges. It is considered in the model that the condensate wets completely the capillary walls (contact angle $\theta \approx 0$) and tends to form a film adjacent to them, developing an annular flow pattern (Fig.4.3b).

The annular flow in the capillary may be interrupted, nonetheless, if the condensate film thickness (e) reaches a critical value (e_{crit}) above which the annular configuration becomes unstable. In this case, the liquid tends to evolve into a bridge accommodated at the capillary mid-section, in a phenomenon known as snap-off (Fig.4.3c). While the capillary accommodates a condensate bridge, the flow of gas and condensate is obstructed. After the snap-off, the

flow can be reestablished if the pressure drop between the capillary extremities exceeds a critical capillary pressure value, and the liquid bridge is removed (Fig.4.3d).

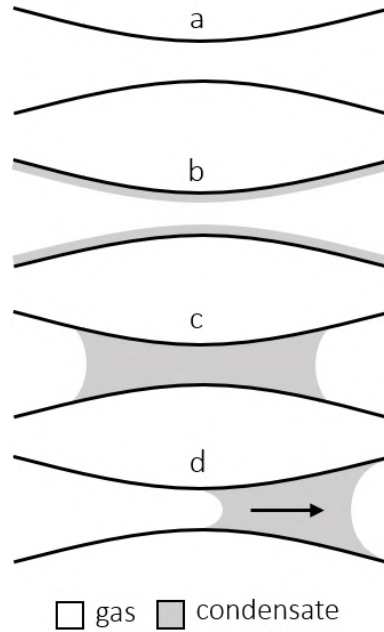


Figure 4.3: Evolution of condensate configuration in a capillary

4.3.2 Gas and Condensate Annular Flow Conductances

The volumetric flow rate of gas and condensate in a capillary can be determined using the concept of fluid conductance: $g = q/\Delta P$, where ΔP is the pressure difference in the capillary. The conductance calculations in this model are based on the steady-state solution of the Navier-Stokes equation for a laminar two-phase annular flow in a straight capillary, given by equations 4-2.

$$g_g = \frac{\pi}{8\mu_g L} (S_g R^2)^2 + \frac{\pi}{4\mu_l L} (R^2 - S_g R^2) S_g R^2 \quad (4-2a)$$

$$g_l = \frac{\pi}{8\mu_l L} (R^2 - S_g R^2)^2 \quad (4-2b)$$

In equations 4-2, μ_g and μ_l are the viscosities of the gas and liquid phases, S_g is the gas saturation and R and L are, respectively, the equivalent radius and length of the capillary. These conductances were developed by Santos and Carvalho [11], for straight circular capillaries. In order to adapt them for constricted capillaries, an equivalent constant radius R was calculated for

each capillary in the network. R represents the radius of a straight capillary that would yield the same volumetric flow rate as the constricted capillary, when subjected to the same pressure difference. The volumetric flow rate as a function of the pressure drop for a laminar, steady-state flow of a Newtonian fluid in an axisymmetric tube with hyperbolic profile [66] was used, leading to the Equation 4-3 for the equivalent radius.

$$R = \left[\frac{2R_{min}^3 R_{max}^2 \sqrt{R_{max}^2 - R_{min}^2}}{R_{min} \sqrt{R_{max}^2 - R_{min}^2} + R_{max}^2 \arctan \left(\sqrt{\frac{R_{max}^2 - R_{min}^2}{R_{min}^2}} \right)} \right]^{\frac{1}{4}} \quad (4-3)$$

For the calculation of the conductances, the fluids properties used in equations 4-2, namely the phases viscosities and saturations, had also to be defined. Since the pressures and fluid contents during the flow are calculated in the nodes, not the edges, a procedure had to be implemented in the model to determine the phases properties in each edge. Considering that the flow between two nodes connected by an edge comes from the node with the highest pressure to the node with the lowest pressure, we assumed that the fluid properties in the edges matched those of the nodes with the highest pressure. In the nodes, the phases saturations are determined via phase equilibrium calculations (Section 4.5) and the viscosities are estimated with the Lohrenz-Bray-Clark correlation [28].

4.3.3

Capillary Blocking Conditions

Several criteria for the formation of the condensate bridge in capillaries, in the context of pore-network modeling, have been suggested in the literature. These criteria are commonly highly simplified, so that the model computational effort is reduced. A condition based simply on a capillary radius threshold of $20\mu m$ was adopted by Fang *et al.* [7] and Li and Firoozabadi [61]. Bustos and Toledo [10] proposed a model containing square capillaries in which the condensate accumulation was initially contained in the capillary corners and the bridge of liquid was formed at condensate saturations greater than 21.46%. This value represents the condensate saturation at which the contact between the gas phase and the pore walls is lost. The same value was adopted by Momeni *et al.* [64]. Jamiolahmady *et al.* [16] suggested a criterion based on the time required for a bridge to be formed, as a function of the capillary geometry, fluid properties and initial condensate film thickness. In our model, it was considered that a condensate bridge is formed upon reaching a critical condensate film thickness, proportional to the constriction radius of each

capillary. Additionally, for the snap-off to happen, the geometry-controlled condition for the fluid break-up in constricted capillaries proposed by Beresnev *et al.* [67] had to be met. This criterion, shown in Equation 4-4, reduces to the condition for the occurrence of the Plateau-Rayleigh instability in the limiting case of cylindrical capillaries.

$$L > 2\pi\sqrt{(R_{min} - e)(R_{max} - e)} \quad (4-4)$$

For $e_{crit} = 0.25R_{min}$, (which will be adopted in the model validation presented in this dissertation) the condensate saturations at which the snap-off occurs vary from $\approx 1\%$, for capillaries with very high R_{max}/R_{min} ratio, to 43.75%, for unconstricted capillaries. This interval is consistent with the values presented in the literature.

Once blocked, the critical pressure drop value for a capillary to be unobstructed is given by Equation 4-5. It is a function of the interfacial tension, σ , between the phases and the radii of the condensate bridge meniscii, R_1 and R_2 , depicted in Figure 4.4. In the model, the interfacial tension is calculated with the correlation proposed by Weinaug and Katz [29], shown in Equation 4-6. In this equation, \mathcal{P} is the parachor value of each $k = 1..n_c$ component in the mixture, ρ_l and ρ_g are the densities, M_l and M_g are the molar masses and x and y are the molar fractions, of the liquid and gas phases, respectively.

$$\Delta P_{crit} = 2\sigma \left(\frac{1}{R_1} - \frac{1}{R_2} \right) \quad (4-5)$$

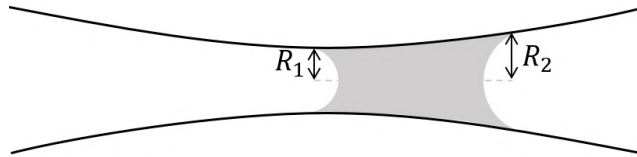


Figure 4.4: Condensate bridge radii, R_1 and R_2 , used to calculate ΔP_{crit}

$$\sigma^{\frac{1}{4}} = \sum_{k=1}^{n_c} \mathcal{P}(k) \left(x(k) \frac{\rho_l}{M_l} - y(k) \frac{\rho_g}{M_g} \right) \quad (4-6)$$

4.4 Equations governing the flow

Once the capillary conductances have been defined, the fluid content and pressure in the nodes can be calculated. This is done via the coupled solution of Molar Balance Equations (section 4.4.1) and Volume Consistency Equations (section 4.4.2), along with the appropriate boundary conditions (section 4.4.3). The resulting system of non linear equations, described in Section 4.4.4, relates the model variables, P_i , N_i^k and s_i , (respectively, the pressure and the number

of moles of each component k , for all nodes, and a source/sink term, for the nodes located at the inlet/outlet of the network) and is solved using the Newton-Raphson Method.

4.4.1

Molar Balance Equation

The fluid content in a node depends on the molar flow rates of the edges connected to it. Therefore, the molar balance equation (eq. 4-7) of each component k in a node i is written in terms of the molar flow rate, \dot{n}_j^k , through its adjacent edges. Also, the term s_i^k is used for the nodes located at the inlet and outlet of the network, to account for the molar flow through its boundaries. The molar flow in a edge, given by Equation 4-8, converts the volumetric flow, calculated with the conductances and the pressure drop, into the molar flow, using the molar fraction of each component in the gas and liquid phases, y^k and x^k , and their molar densities, ξ_g and ξ_l . The switch from opened to closed states in a edge was implemented in the model by multiplying Equation 4-8 by a continuous approximation of a unit step function H_j , explained in Section 4.4.1.1. H_j is equal to unity, when the conditions for annular flow are met at the edge j , and equal to zero, when the flow is blocked by a condensate bridge. Equation 4-9 represents the pressure that drives the flow through the edges. It amounts to the difference in the pressures of the pores connected by the capillary, minus the interfacial pressure difference, when a condensate bridge is formed. The inclusion of the interfacial pressure difference in Eq. 4-9 is controlled by the function H^{int} , also discussed in Section 4.4.1.1.

$$\frac{\partial N_i^k}{\partial t} = - \sum_{j=1}^{n_{edge}} c_{ij} \dot{n}_j^k + s_i^k \quad (4-7)$$

$$\dot{n}_j^k = H_j (y^k \xi_g g_g + x^k \xi_l g_l)_j \Delta P_j^{flow} \quad (4-8)$$

$$\Delta P_j^{flow} = \sum_{m=1}^{n_{node}} c_{mj} P_m - H_j^{int} \Delta P_j^{int} \quad (4-9)$$

4.4.1.1

Functions H and H^{int}

Predicting whether a capillary is opened or closed to flow, due to the formation and retention of condensate bridges, constitutes a central part in the proposed model formulation. The flow status of a capillary, as available or not for flow, can be written as a function of its gas saturation and pressure difference. For relatively high S_g and/or high ΔP , the capillary is opened to flow. The combination of low S_g and ΔP leads to a capillary that is

closed to flow. Including this transitions in the model would, therefore, make the conductances discontinuous function of S_g and ΔP . Another instance of discontinuity in the model formulation involves the inclusion the interfacial pressure difference in the calculation of the capillary flow rate. This term only appears for low S_g and high ΔP , meaning that a condensate slug is moving through the capillary.

However, as a condition for convergence of the multivariate Newton-Raphson method, the system of equations should contain only continuously differentiable functions in the neighborhood of its roots. Therefore, in order to avoid convergence issues, those discontinuous functions of S_g and ΔP were substituted by the continuous approximations of unit step functions given by Equation 4-10.

$$h_1 = \frac{1}{2} \left\{ 1 - \tanh \left[\frac{1}{K_1} \left(\frac{S_g}{S_{g,crit}} - 1 \right) \right] \right\} \quad (4-10a)$$

$$h_2 = \frac{1}{2} \left\{ 1 - \tanh \left[\frac{1}{K_2} \left(\frac{\Delta P}{\Delta P_{crit}} - 1 \right) \right] \right\} \quad (4-10b)$$

In Equation 4-10, $S_{g,crit}$ is the gas saturation calculated at a condensate film thickness $e = e_{crit}$. Thus, $S_g < S_{g,crit}$ leads to the occurrence of snap-off. Function h_1 is equal to one for $S_g < S_{g,crit} - \epsilon$ and equal to zero for $S_g > S_{g,crit} + \epsilon$. 2ϵ is the thickness of the continuous representation region of the discontinuity of the step function. ΔP_{crit} is the critical capillary pressure difference for a capillary to be reopened to flow, once the snap-off happened, given by eq. 4-5. Function h_2 is equal to one for $\Delta P < \Delta P_{crit} - \epsilon$ and equal to zero for $\Delta P > \Delta P_{crit} + \epsilon$. K_1 and K_2 are shape factors that control the thickness 2ϵ on the transition region. Low values for K_1 and K_2 lead to smaller ϵ and better approximations of a discrete step function, and their values should be adjusted according to functions h_1 and h_2 domains.

Since the capillary flow is interrupted when both S_g and ΔP are below their critical values, the conductances were multiplied by H , given by equation 4-11, in the capillary molar flow calculation (eq. 4-8).

$$H = 1 - h_1 h_2 \quad (4-11)$$

As for the subtraction of the interfacial pressure drop in the capillary flow rate calculation, it was achieved by multiplying ΔP^{int} by H^{int} , shown in Equation 4-12.

$$H^{int} = h_1 - h_1 h_2 \quad (4-12)$$

For the results presented in Chapter 5, the adopted shape factors were

$K_1 = 0.1$ and $K_2 = 0.3$. These values were achieved upon successive trials of reducing the shape factors, and proved to be low enough to represent well a unit step function, but not so low as to cause convergence difficulties.

4.4.2

Volume Consistency Equation

In the proposed model, the porous medium contains only the gas and condensate phases. The volume of a node, therefore, can be written as the sum of the volumes of gas and condensate contained in it: $V_i = V_i^g + V_i^l$. Given that the network is slightly compressible, the node volume can also be written as a function of the node pressure and compressibility $\nu_i = \frac{1}{V_i} \frac{\partial V_i}{\partial P_i}$.

Considering \bar{V}_i the volume of a node at a reference pressure \bar{P}_i , its volume at any pressure can be approximated by Equation 4-13a. In regard to the node contents, $V_i^g + V_i^l$ can be determined by relating P_i and T with the fluid parameters \mathcal{L}_i , Z_i^g , Z_i^l , x_i^k , y_i^k and v_k (respectively: the fraction of the N_i moles in the liquid phase, the compressibility factors and the molar fractions of each component k in the gas and liquid, and the volume shift parameters of each component k) and the gas constant, R , as presented in Equation 4-13b.

$$V_i \approx \bar{V}_i [1 + \bar{\nu}_i (P_i - \bar{P})] \quad (4-13a)$$

$$V_i = N_i \left[\mathcal{L}_i \left(\frac{Z_i^l RT}{P_i} - \sum_{k=1}^{n_c} v_k x_i^k \right) + (1 - \mathcal{L}_i) \left(\frac{Z_i^g RT}{P_i} - \sum_{k=1}^{n_c} v_k y_i^k \right) \right] \quad (4-13b)$$

The combination of the equations above leads to the volume consistency equation, given by Equation 4-14.

$$N_i - \frac{\bar{V}_i [1 + \bar{\nu}_i (P_i - \bar{P})]}{\mathcal{L}_i \left(\frac{Z_i^l RT}{P_i} - \sum_{k=1}^{n_c} v_k x_i^k \right) + (1 - \mathcal{L}_i) \left(\frac{Z_i^g RT}{P_i} - \sum_{k=1}^{n_c} v_k y_i^k \right)} = 0 \quad (4-14)$$

4.4.3

Boundary Conditions

Two sets of boundary conditions can be chosen for a flow analysis conducted with the model. In the first, pressure is fixed at both inlet and outlet faces of the network, while in the second, molar flow rate is fixed at the inlet and pressure at the outlet. For all the analyses presented in this dissertation, the chosen boundary conditions were fixed molar flow rate at the inlet and pressure at the outlet. Other parameters that have to be imposed are the composition of the fluid injected in the network and the temperature.

4.4.4

Solution via Newton-Raphson Method

Equations 4-7 and 4-14, associated with the appropriated boundary conditions, were integrated over time using an implicit method and therefore led to a system of non-linear equations that relate the variables N_i^k , P_i and s_i at each time step. The solution is obtained using Newton-Raphson method, where the unknown vector is $\mathbf{u}=[N_i^k; P_i; s_i]$ and the residue vector is $\mathbf{R}=[(R_N)_i^k; (R_V)_i; (R_C)_i]$. The entries of the vector \mathbf{R} are presented in equations 4-15.

$$(R_N)_i^k = (N_i^k)^{t+1} - (N_i^k)^t + dt \left\{ \sum_{j=1}^{n_{edge}} c_{ij} [H_j^\tau (y^k \xi_g g_g + x^k \xi_l g_l)_j^\tau \left(\sum_{m=1}^{n_{node}} c_{mj} P_m^{t+1} - H_j^{int,\tau} \Delta P_j^{int,\tau} \right) - z_{si}^{k\tau} s_i^{t+1}] \right\} \quad (4-15a)$$

$$(R_V)_i = (N_i)^{t+1} - \frac{\bar{V}_i [1 + \bar{v}_i (P_i^{t+1} - \bar{P})]}{\mathcal{L}_i^\tau \left(\frac{(Z_i^l)^\tau RT}{P_i^{t+1}} - \sum_{k=1}^{n_c} v_k (x_i^k)^\tau \right) + (1 - \mathcal{L}_i^\tau) \left(\frac{(Z_i^g)^\tau RT}{P_i^{t+1}} - \sum_{k=1}^{n_c} v_k (y_i^k)^\tau \right)} \quad (4-15b)$$

$$(R_C)_i = \begin{cases} dt \frac{(s_i - s_i^{imp})}{RT}, & \text{for imposed molar flow at node } i \\ \frac{(P_i - P_i^{imp}) \bar{V}_i}{RT}, & \text{for imposed pressure at node } i \end{cases} \quad (4-15c)$$

In order to reduce the non-linearity of the system of equations, and consequently the computational effort, the phase equilibrium calculations are performed uncoupled from the system of equations 4-15. In a procedure first proposed by Collins *et al.* [65], the flash calculations are carried out at each iteration of the Newton-Raphson method, at each time step. Therefore, in equations 4-15, when solving for \mathbf{u}^{t+1} , all the fluid properties dependent on the phase equilibrium calculations ($x, y, \xi, g, \mathcal{L}, Z, H, \Delta P^{int}$) are computed with \mathbf{u}^τ , where τ corresponds to the preceding iteration of the Newton-Raphson method. Separating phase equilibrium calculations from the flow equations solution allows the implementation of robust methods for flash calculations and phase stability tests, which may be desirable for modeling gas-condensate systems. In the next section, the phase equilibrium calculations implemented in the model are presented.

4.5

Phase equilibrium calculations

4.5.1 Flash calculation

Flash calculations are used to quantify and characterize the phases in thermodynamic equilibrium in a system. In the proposed model, a flash calculation at fixed pressure and temperature is performed after each Newton-Raphson iteration at each node i , given its current set of P_i , N_i^k and temperature. As a result, the fraction of moles in the liquid state (\mathcal{L}_i) and the compositions of the gas and liquid phases (y_i^k and x_i^k , respectively) are obtained. In this section, an overview of the procedure adopted to perform flash calculations is presented. More details regarding the algorithm implementation can be found in the work of Santos and Carvalho [11].

The flash formulation is based on the fact that, for a system with gas and liquid phases at thermodynamic equilibrium, the fugacities (f) of each component (k) in both phases must be equal, as expressed in Equation 4-16.

$$f_{gas}^k(T, P, y^k) = f_{liq}^k(T, P, x^k) \quad (4-16)$$

By combining Equation 4-16 with the definition of coefficient of fugacity, expressed in Equations 4-17, the compositions of gas and liquid phases in a system at equilibrium can be related through the constants K^k , as shown in Equation 4-18.

$$\phi_{gas}^k = \frac{f_{gas}^k}{y^k P} \quad (4-17a)$$

$$\phi_{liq}^k = \frac{f_{liq}^k}{x^k P} \quad (4-17b)$$

$$K^k = \frac{y^k}{x^k} = \frac{\phi_{liq}^k}{\phi_{gas}^k} \quad (4-18)$$

Another way of relating the compositions of the gas and liquid phases at thermodynamic equilibrium is shown in Equation 4-19, using the composition of the mixture, $z^k = N^k / \sum^k(N^k)$, and the fraction of moles in the liquid phase, \mathcal{L} .

$$z^k = \mathcal{L}x^k + (1 - \mathcal{L})y^k \quad (4-19)$$

Using Equations 4-18 and 4-19, and the restrictions $\sum^k(x^k) = 1$ and $\sum^k(y^k) = 1$, we can write $\sum^k(x^k) - \sum^k(y^k) = 0$ as Equation 4-20, known as the Rachford-Rice equation. This equation constitutes a central part of the flash calculations, and is used to determine \mathcal{L} , and, consequently, x^k and y^k , given that the constants K^k are known.

$$\sum_{k=1}^{n_c} \frac{z^k(1 - K^k)}{\mathcal{L} + (1 - \mathcal{L})K^k} = 0 \quad (4-20)$$

Once Equations 4-16 to 4-20 have been defined, the lacking element in the phase-equilibrium calculations implemented in our model involves the calculation of the components fugacities, given the phases compositions. For this purpose, the Peng and Robinson of state [25], shown in Equation 4-21, was used. This equation relates the molar volume (V_{mol}) of a phase, with its pressure, temperature, and two parameters, a and b , defined in Equations 4-22 and 4-23, respectively. In these equations, z^k is the phase composition (x^k for liquid and y^k for gas), λ^{km} are the binary interaction coefficients between the components k and m , and a^k and b^k are the Peng and Robinson equation parameters for pure components, k .

$$P = \frac{RT}{V_{mol} - b} - \frac{a(T)}{V_{mol}(V_{mol} + b) + b(V_{mol} - b)} \quad (4-21)$$

$$a(T) = \sum_{k=1}^{n_c} \sum_{m=1}^{n_c} z^k z^m \sqrt{a^k a^m} (1 - \lambda^{km}) \quad (4-22)$$

$$b = \sum_{k=1}^{n_c} z^k b^k \quad (4-23)$$

The parameters a^k and b^k are calculated with Equations 4-24 and 4-25, where T_c^k , P_c^k and w^k are the critical temperature, critical pressure and acentric factor of the component k .

$$a^k = \frac{0.45724R^2 T_{ck}^2}{P_c^k} \alpha^k \quad (4-24a)$$

$$\alpha^k = (1 + (0.37464 + 1.54226w^k - 0.26992(w^k)^2)(1 - (T_r^k)^{0.5}))^2 \quad (4-24b)$$

$$T_r^k = \frac{T}{T_c^k} \quad (4-24c)$$

$$b^k = \frac{0.0778RT_c^k}{P_c^k} \quad (4-25)$$

Using the definition of the compressibility factor $Z = PV_{mol}/RT$, Equation 4-21 can be rewritten as a cubic equation of Z , as shown in Equation 4-26. This polynomial function may have three real roots, of which the largest is attributed to the gas phase, the lowest is attributed to the liquid phase and the intermediate is discarded. Alternatively, it can have just one real root, which is used for the analyzed phase, while the two imaginary roots are discarded.

$$0 = Z^3 - (1 - B)Z^2 + (A - 2B - 3B^2)Z - (AB - B^2 - B^3) \quad (4-26a)$$

$$A = \frac{aP}{R^2T^2} \quad (4-26b)$$

$$B = \frac{bP}{RT} \quad (4-26c)$$

Finally, once the compressibility factor Z is calculated with the Peng and Robinson equation, the fugacity coefficients of the phase components are calculated with Equation 4-27, and the fugacities can be found with Equations 4-17.

$$\ln(\phi^k) = \frac{b^k}{b}(Z - 1) - \ln(Z - B) - \frac{A}{2\sqrt{2}B}CD \quad (4-27a)$$

$$C^k = \left(\frac{2}{a} \sum_{m=1}^{n_c} (z^m \sqrt{a^k a^m} (1 - \lambda^{km})) - \frac{b^k}{b} \right) \quad (4-27b)$$

$$D = \ln \left(\frac{Z + (1 + \sqrt{2})B}{Z + (1 - \sqrt{2})B} \right) \quad (4-27c)$$

With the presented equations (4-16 to 4-27), the following iterative process was implemented in the model, for the flash calculations:

1. Determine an initial guess for K . This can be done using the equation proposed by Wilson [68] (Eq. 4-28) or by using the ratio y^k/x^k from the solution of the previous time step.

$$\ln(K^k) = 5.37(1 + w^k) \left(1 - \frac{T_c^k}{T^k}\right) + \ln(P_r^k) \quad (4-28)$$

2. With K^k , solve the Rachford-Rice equation (Eq. 4-19) for \mathcal{L} . and use Eqs. 4-17 and 4-19 to determine y^k and x^k .
3. For both phases, determine the fugacities of all components with the Peng and Robinson equation of state, using Eqs 4-21 to 4-27 and Eq. 4-17.
4. Check whether equation 4-16 is satisfied. If the fugacities of all components in both phases are equivalent, the solution converged. Otherwise, update the values of K^k with the ratio of fugacity coefficients calculated in item 3, $\phi_{liq}^k/\phi_{gas}^k$, and go back to item 2.

4.5.2 Stability Test

The iterative solution of the flash calculation described in last section constitutes a significant part of the computational effort demanded by our model. For this reason, it is interesting to also implement a criterion to avoid the flash calculations for the cases when the mixture is more stable as a single phase. With this purpose, the the stability test developed by Michelsen in 1982 [69] was implemented. In this section, the idea behind the adopted stability test is discussed. Details related to its implementation and solution methods can be found in the work of Michelsen [69].

Concisely, this criterion is based on the fact that, in a single-phase system, a new phase is created only if that reduces the Gibbs energy of the system. As a single phase, the Gibbs energy of the mixture can be calculated with Equation 4-29.

$$G_0 = \sum_{k=1}^{n_c} N^k \mu_0^k \quad (4-29)$$

where μ_0^k is the chemical potential of component k in the mixture

Assuming that a new phase is created containing an infinitesimal number of moles ϵ , the change in the Gibbs energy in the new system composed by phases I and II , in relation to the old system, is given by Equation 4-30.

$$\Delta G = G_I + G_{II} - G_0 = G(N - \epsilon) + G(\epsilon) - G_0 \quad (4-30)$$

Following the procedure proposed by Michelsen [69], Equation 4-31 can be found using a Taylor series expansion for G_I and discarding the second order terms of ϵ .

$$G(N - \epsilon) = G_0 - \epsilon \sum_{k=1}^{n_c} y^k \mu_0^k \quad (4-31)$$

Therefore, Equation 4-30 can be rewritten as Equation 4-32. Using the criterion premise, this variation in Gibbs energy must be negative, so that the creation of a second phase takes place.

$$\Delta G = \epsilon \sum_{k=1}^{n_c} y^k (\mu^k(\mathbf{y}) - \mu_0^k) \quad (4-32)$$

Since ϵ represents the number of moles of the created phase and must be positive, the criterion for stability of the system to as a single-phase is given by Equation 4-33, for all trial compositions \mathbf{y} .

$$F(\mathbf{y}) = \sum_{k=1}^{n_c} y^k (\mu^k(\mathbf{y}) - \mu_0^k) \geq 0 \quad (4-33)$$

Therefore, in order to avoid unnecessary flash calculations, during the solution of the system of equations 4-15 for \mathbf{u}^{t+1} the criterion shown in Eq.

4-33 is applied to all nodes in which only one phase was identified at \mathbf{u}^t . Then, if the criterion indicates that a second phase should be formed, the flash calculation routine is performed. Contrarily, if the system remains as a single phase, a criterion for phase identification is used, to verify whether the single phase is gaseous or liquid. For this purpose, the simple criterion for gas phase identification suggested by Pedersen and Christensen [1], shown in Equation, 4-34 was used.

$$c = \frac{V_{mol}}{b} > 1.75 \quad (4-34)$$

In this criterion, the constant c is equal to the ratio between the mixture molar volume and the b parameter of the Peng and Robinson equation (Eq. 4-23). The mixture is gaseous, if $c > 1.75$, and liquid, otherwise.

5 Results

In this chapter, the results obtained with the model described in Chapter 4 are presented. First, the model validation against experimental data from the literature is presented in Section 5.1. Then, potential applications of the model, involving the evaluation of enhanced oil recovery (EOR) methods is presented in Section 5.2.

5.1 Pore-network model validation

The relative permeability (k_r) curves obtained with coreflooding experiments by Jamiolahmady *et al.* [16] were used to validate the proposed model. The selected experiments were performed at three different gas flow rates and two different interfacial tension values, providing comprehensive data to evaluate whether the model is able to reproduce the effects of these parameters on gas and condensate coupled flow. Attempts to reproduce the same experiments with different pore-network models were presented by Jamiolahmady *et al.* [16] and Momeni *et al.* [64]. Their results were also used for comparison in the validation .

The pore-network, fluids and flow parameters used in the validation are presented in Sections 5.1.1 to 5.1.3. The obtained numerical relative permeability curves are compared to the experimental curves in Section 5.1.4. Finally, two additional analysis are presented in Sections 5.1.5 and 5.1.6, in order to verify whether the proposed model is capable of reproducing appropriately the gas blockage by condensate bridge formation and the compositional shift observed during gas-condensate flow in porous media.

The results presented in this section have been published recently in the Journal of Petroleum Science and Engineering, in an article entitled: Pore-Scale Compositional Modeling of Gas-Condensate Flow: Effects of Interfacial Tension and Flow Velocity on Relative Permeability [70].

5.1.1

Pore-network construction

A Berea core sample with porosity $\phi = 18.2\%$, absolute permeability $k = 92mD$ and irreducible water saturation $S_{wc} = 26.4\%$ was used in the experiments [16]. As the model does not account for the presence of water, it was considered that the created pore-network represented only the volume occupied by hydrocarbons in the porous media, and the final saturations were corrected in the results to be based on the total pore volume ($V_{PN}/(1 - S_{wc})$). Additionally, the predicted values of relative permeability were also scaled down to account for the connate water presence. With that, the experimental gas relative permeability of 0.8 at a condensate saturation equal to zero was matched. A Weibull probability distribution function of pore throat sizes was provided [16] and used to define the constriction radius of the capillaries in the network. In this distribution, illustrated in Figure 5.1, R_{min} ranges from $1.28\mu m$ to $19.21\mu m$, with an average value of $8.5\mu m$.

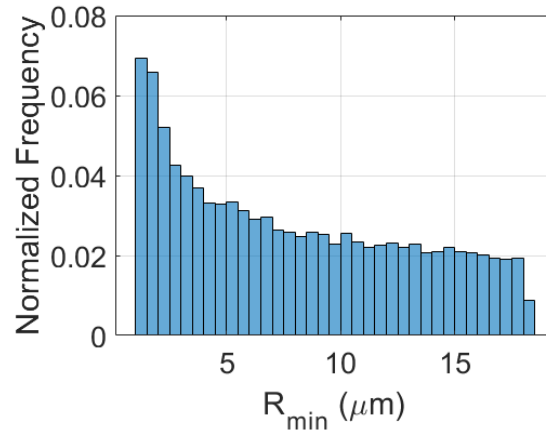


Figure 5.1: Normalized probability distribution function for R_{min}

In their model, Jamiolahmady *et al.* [16] used constricted capillaries with a constant ratio $R_{max}/R_{min} \approx 3.33$. The authors suggested that this value did not reflect the true characteristics of the real porous medium, thus affecting negatively the results. In the proposed model, this limitation was mitigated by calculating R_{max} values based on the aspect ratio between pore body and throat radii, $AR = R_{max}/R_{min}$, of a berea sample. This correction is important since the aspect ratio has a large impact on multi-phase flow simulation [5]. The distribution function the AR values used in the generated pore-network, along with that obtained for a pore-network extracted from a 3D Micro-CT image of a berea sample [5], is presented in Figure 5.2, indicating that the values of AR used in our model are representative of Berea cores.

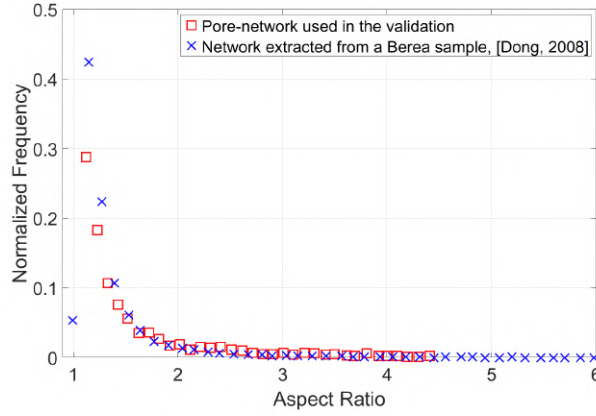


Figure 5.2: Aspect ratio of pore-networks extracted from a 3D image of a berea sandstone sample

A cubic lattice of $20 \times 25 \times 25$ nodes represented the network topology. The coordination number was set to have an average value of 3, and was obtained by randomly removing capillaries from the original cubic lattice, as done in the network models used for comparison in the validation [16, 64]. Additionally, the capillary length was chosen to be constant and equal to $75 \mu m$. This value, which is adequate to represent a berea sample [5], could satisfy the necessity of matching ϕ and k of the core used in the experiments, while using the radii distribution and aspect ratio shown in Figures 5.1 and 5.2.

5.1.2 Injected fluid

Gas-condensate mixtures of methane (C_1) and normal butane (nC_4) were used as the fluid injected in the cores. For a fixed temperature of $37^\circ C$, the experiments were repeated at two levels of pressure, so that two different interfacial tension values were achieved. The pressures used in the simulations to reproduce the experimental conditions, as well as the viscosities of both phases calculated with the Lohrenz-Bray-Clark correlation [28], are presented in Table 5.1.

σ (mN/m)	Pressure (MPa)	μ_g (Pa.s)	μ_l (Pa.s)
0.015	13.04	2.26×10^{-5}	3.51×10^{-5}
0.037	12.78	2.14×10^{-5}	3.71×10^{-5}

Table 5.1: Pressure and viscosities of gas and condensate at $37^\circ C$ and interfacial tension values of 0.015 and $0.037 mN/m$

5.1.3

Flow conditions

The experimental relative permeability curves were calculated using the Darcy's law, during the steady-state gas-condensate flow through the cores. Each point of the k_r curves was measured by injecting the $C_1 - nC_4$ mixture at a different condensate to gas flow ratio (CGR) in the cores. Also, for each CGR, the injected gas flow rate was controlled in order to generate gas flow velocities (v_g) of $9md^{-1}$, $18md^{-1}$ and $36md^{-1}$. This was reproduced with the model by shifting the molar flow rate and molar fraction of the components in the injected composition. At a fixed pressure and temperature, reducing the fraction of methane in the mixture, while increasing appropriately the total molar flow rate, leads to higher CGRs for the same v_g . For the case at $P_{out} = 13.04MPa$, the C_1 molar percentages were 75%, 77%, 78%, 79% and 79.5%, while for the case at $P_{out} = 12.78MPa$ they were 75%, 78%, 79%, 80% and 80.5%. With these compositions, the initial condensate saturation in the networks ranged from 1% to 22% while the values achieved at steady-state flow varied from about 10% to 40%, due to liquid accumulation. The criteria for achieving steady-state in the model were equal injected and produced molar flow rates, and constant average pressure and saturation in the network.

5.1.4

Relative permeability curves

Figure 5.3 presents the relative permeability curves for gas and condensate phases, k_{rg} and k_{rc} , for $\sigma = 0.037mN/m$ and $v_g = 18md^{-1}$. It shows the predictions of the proposed model, the curves obtained with experiments [16] and the curves predicted with the pore-network models presented by Jamiolahmady *et al.* [16] and Momeni *et al.* [64].

As discussed in Section 3.4, the model of Jamiolahmady *et al.* [16] does not consider the fluid composition and uses empirically adjusted coefficients to match the predictions to the measured relative permeabilities. Moreover, it assumes a fixed ratio between the pore body and pore throat radii. As for the model proposed by Momeni *et al.* [64], although flash calculations are used to determine the amount of condensate at each throat, the system of equations is based on mass conservation in each pore and does not enforce molar conservation of each component. Also, in that work, the relative permeability curves are calculated during transient flow. This procedure leads to varying gas and condensate flow rates at the outlet of the network during the simulation and does not represent the experimental procedure [16].

All three models presented in the plot reproduce well the experimental

behavior of the gas relative permeability curve at low condensate saturation, $S_c < 0.20$. While ours and Momeni *et al.*'s results follow the measured k_{rg} curve up to $S_c \approx 0.4$, the predictions presented by Jamiolahmady *et al.* [16] present a sharp decline at $S_c \approx 0.25$, underpredicting the gas permeability beyond this value. As for the condensate curves, our model, while capturing the general behavior of the experimental k_{rc} curve, overestimates its values, particularly in the range $0.15 \leq S_c \leq 0.35$. This may be explained by the fact that the condensate conductance is calculated based on annular flow through smooth circular capillaries. Including the effect of wall roughness and non circular geometry could potentially reduce the mobility of the liquid phase and improve the results. Once again, the results from Jamiolahmady *et al.* [16] are accurate up to $S_c = 0.25$, above which they over predict the experimentally measured k_{rc} . The curve presented by Momeni *et al.* [64] does not capture the experimental curve behavior, with $k_{rc} \approx 0$ for $S_c < 0.17$ and a k_{rc} plateau for $S_c > 0.30$.

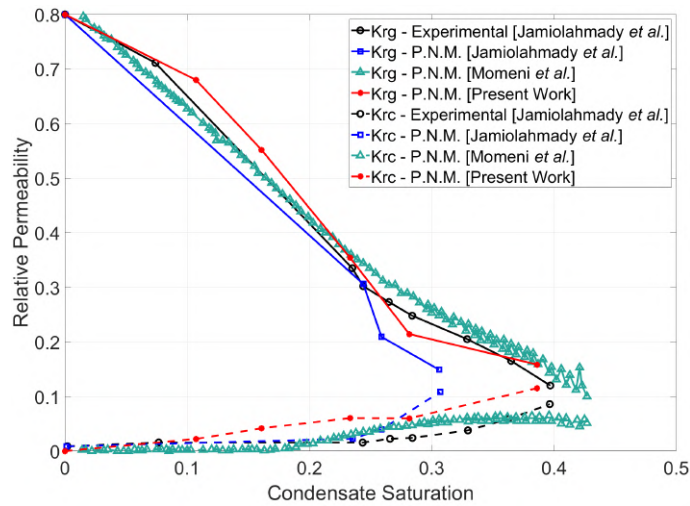


Figure 5.3: k_{rg} and k_{rc} , at $\sigma = 0.037mN/m$ and $v_g = 18md^{-1}$

The effect of gas velocity on the relative permeability curves is shown in Figures 5.4 and 5.5. They represent the k_r curves for $\sigma = 0.037mN/m$ and v_g equal to $9md^{-1}$ and $36md^{-1}$, respectively. The proposed model is able to predict accurately the positive effect of flow rate on the relative permeability curves. For both gas velocities, our model produced results that more closely reproduce the experimental data than those presented by Jamiolahmady *et al.* [16]. Momeni *et al.* [64] did not present results for v_g other than $18md^{-1}$ or for different values of interfacial tension in their model validation.

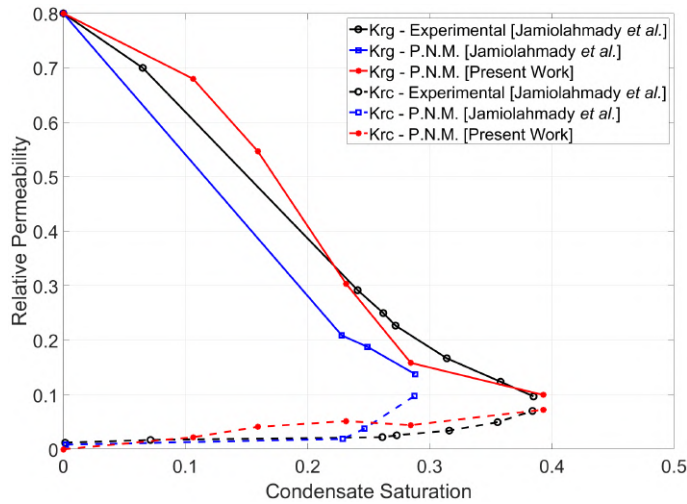


Figure 5.4: k_{rg} and k_{rc} , at $\sigma = 0.037mN/m$ and $v_g = 9md^{-1}$

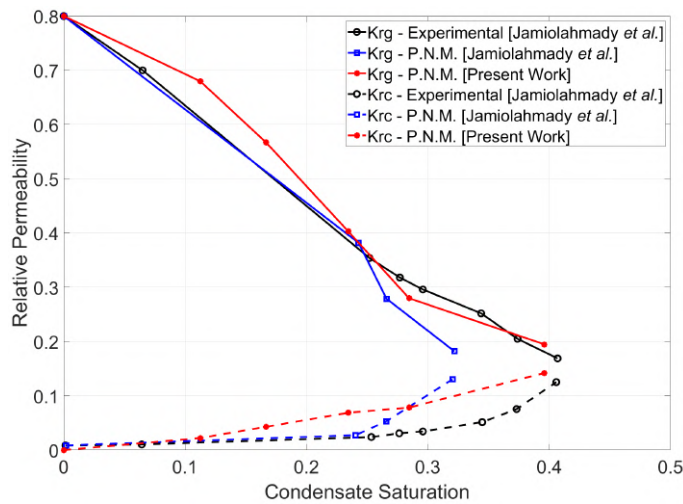


Figure 5.5: k_{rg} and k_{rc} , at $\sigma = 0.037mN/m$ and $v_g = 36md^{-1}$

The effect of interfacial tension on the flow behavior can be inferred in Figures 5.6, 5.7 and 5.8, which show the relative permeability curves at lower interfacial tension, $\sigma = 0.015mN/m$, and the same gas velocities as Figures 5.4, 5.3 and 5.5, respectively. Higher k_r are expected at lower interfacial tension levels, as the phase trapping mechanism is weakened with reduced capillary pressure. This effect was both verified experimentally and predicted with the proposed model. For the three analyzed gas flow velocities, the predicted k_r curves agreed reasonably well with the measured data. While the model proposed by Jamiolahmady *et al.* [16] represented better the experimental k_r curves at $v_g = 9md^{-1}$ and $v_g = 18md^{-1}$, their model had coefficients adjusted specifically to match the case at $\sigma = 0.015mN/m$ and $v_g = 9md^{-1}$, leading to the almost perfect fit. The proposed model does not have any adjustable parameter to fit experimental data.

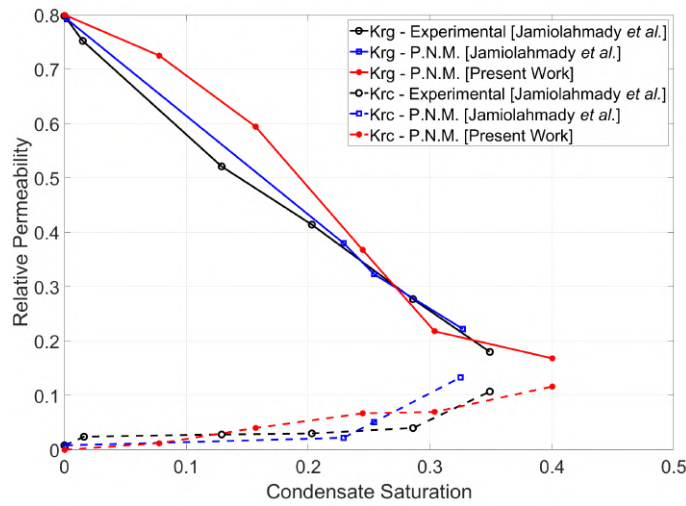


Figure 5.6: k_{rg} and k_{rc} , at $\sigma = 0.015mN/m$ and $v_g = 9md^{-1}$

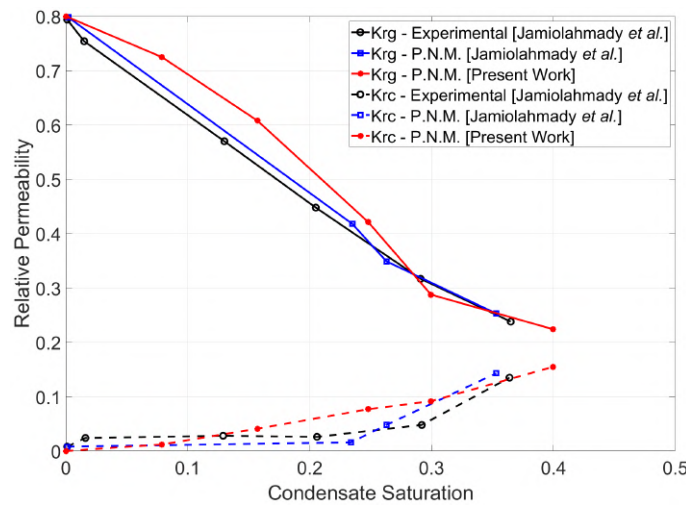


Figure 5.7: k_{rg} and k_{rc} , at $\sigma = 0.015mN/m$ and $v_g = 18md^{-1}$

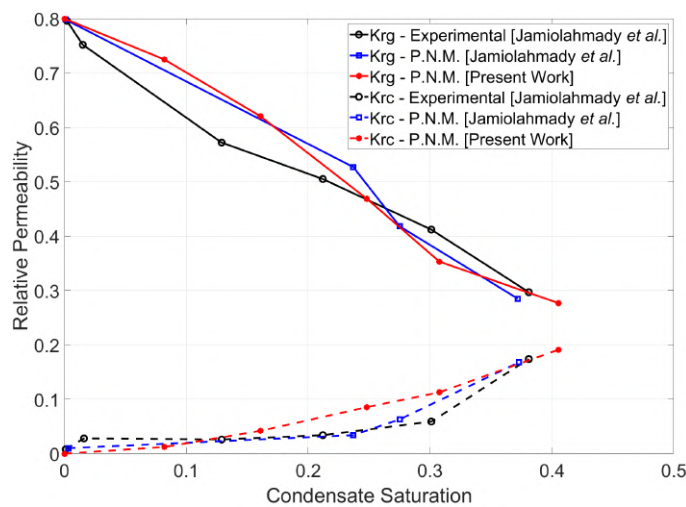


Figure 5.8: k_{rg} and k_{rc} , at $\sigma = 0.015mN/m$ and $v_g = 36md^{-1}$

5.1.5 Visualization of blocked capillaries

The sharp decline in k_{rg} with condensate saturation buildup in porous media has been attributed to the formation of condensate bridges that obstruct the gas flow in pore throats [21, 2, 4, 16]. This phenomenon was well captured by our model, as illustrated in Figure 5.9. Figures 5.9 (a) to (e) show the opened and blocked capillaries of the network at the conditions used to construct the k_r curves at $\sigma = 0.037mN/m$ and $v_g = 18md^{-1}$, displayed in Figure 5.3. For the two lowest S_c values, only a small fraction of capillaries is obstructed with condensate, 0.5% and 3.64%, for (a) and (b) respectively, meaning that k_{rg} is not significantly reduced. Also, at those saturation levels, the blocked capillaries not only are not numerous, but also are the most constricted ones, which implies that they provided a weak contribution to flow. For the three highest S_c values, the percentage of blocked capillaries rose to (c) 14.36%, (d) 43.50% and (e) 64.73%, which reduces significantly the available gas flowing paths, leading to a substantial decrease in k_{rg} .

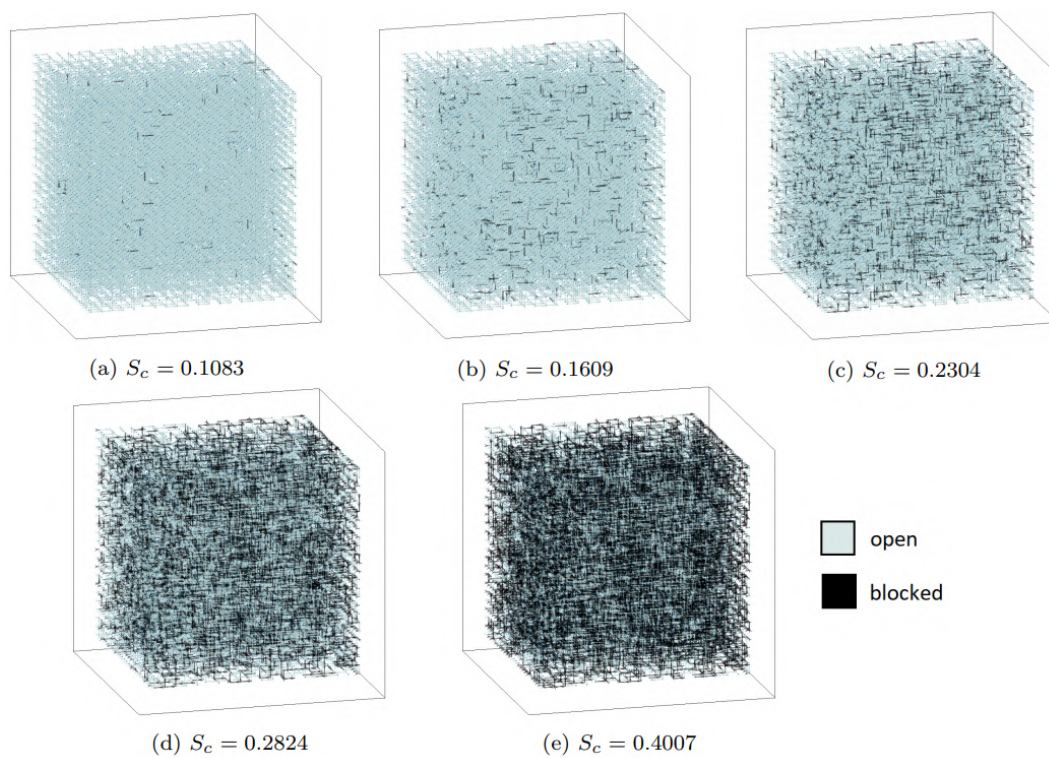


Figure 5.9: Blocked Capillaries, at $\sigma = 0.037mN/m$ and $v_g = 18md^{-1}$

5.1.6 Compositional shift during gas-condensate flow

Another phenomenon that could be analyzed in the results obtained with the proposed model is the compositional shift observed in gas-condensate reservoirs below the dew point pressure. The different mobilities displayed by gas and condensate during flow in porous media, associated with their different compositions, lead to liquid accumulation and buildup of heavy components, following condensation. By using a compositional formulation, this shift in local composition could be quantified in the results used for the model validation, as exemplified in Table 5.2. It contains the molar percentage of n-butane in the fluid injected in the network, and the molar percentage of the same component found in the network at steady-state condition, at $\sigma = 0.037mN/m$ and $v_g = 18md^{-1}$.

Injected $nC_4\%$	$nC_4\%$ in the Network
19.5	22.14
20.0	23.51
21.0	25.29
22.0	26.52
25.0	29.19

Table 5.2: Compositional shift in the network at $\sigma = 0.037mN/m$ and $v_g = 18md^{-1}$. The values presented in this table represent molar percentages.

For all injection scenarios, the fraction of nC_4 , the heavier component in the studied binary mixture, was higher in the network than in the injected fluid. Consequently, the $C_1 - nC_4$ phase envelopes are displaced to the right, as illustrated in Figure 5.10, for the case where the nC_4 raised from 25% to 29.19%. This shift not only impacts the liquid dropout prediction, but also may lead to a transition in the general behavior of the mixture. It can be seen in the phase envelopes that the critical point, marked as a Δ , was dislocated from $T=33^\circ\text{C}$ to $T=49^\circ\text{C}$. Given that the network temperature was 37°C , this makes the behavior of the fluid mixture change from gas-condensate to volatile oil. This phenomenon, known to take place in gas condensate reservoirs near the wellbore region [26, 27], impacts significantly the response of the fluid system to changes in pressure and temperature, and can only be appropriately predicted with compositional modeling, such as the one proposed here.

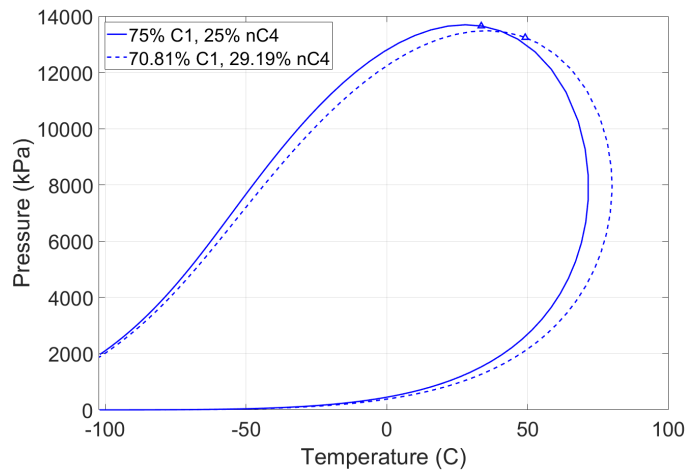


Figure 5.10: Phase Envelopes of C1-nC4 binary mixtures, obtained with the CMG software Winprop

5.1.7 Discussion

The results indicate that the proposed model is capable of producing data appertaining to gas-condensate flow in porous media at a good level of reliability, without using any adjustable parameters to fit experimental data. Relative permeability curves under different flow conditions agreed reasonably well with experimental data, while the findings regarding capillary blockage and compositional shift in the porous medium are in line with gas-condensate literature. Therefore, the data obtainable with the model could contribute to a better understanding of flowing conditions leading to liquid blockage in specific gas-condensate reservoirs. By implementing in the model pore-networks extracted from reservoir rock pore-scale imaging, along with injected compositions based on real fluid samples, bespoke relative permeabilities curves could be generated as inputs to reservoir-scale simulations, supporting improved production estimates. Additionally, the analysis of the liquid content evolution in the pore-networks during the two-phase transient flow provides insights into how fast condensate blockage should develop under different flowing conditions, which components of the reservoir fluids are more likely to be trapped in the liquid accumulation, and whether the mixture undergoes the transition from a gas-condensate to a volatile-oil system.

The generalizability of the presented results, however, is bounded by some modeling limitations. Starting with the fluid properties determination, the Lohrenz-Bray-Clark correlation [28] for viscosity may not be ideal to characterize gas-condensate fluids, and that may impact negatively the model's predictions. Concerning the representation of real porous media, the use

of symmetric constricted capillaries could impair an optimal pore-network generation based on pore-scale imaging, as this shape could be ill-fitted to represent throats connected to bodies with very different radii. As for the two-phase flow modeling, the conductances presented in eq. 4-2 were derived from the solution of the Navier-Stokes equations for laminar steady-state annular flow in cylindrical tubes, considering the same pressure for both phases at the tube extremities. Therefore, the flow between pore bodies in annular configuration is modeled as mainly governed by pressure difference and viscous forces. This could result in inaccuracies in flow prediction, especially at lower pressures. Surface-tension driven flow is addressed in the model by establishing the conditions for flow from pore bodies to pore throats, which lead to the snap-off of the gas. After this event, the liquid accommodated at the throats blocks the flow, unless the pressure difference overcomes capillary forces, as discussed in Section 4.3. Besides, the model does not incorporate an aqueous phase in the fluids system. Thus, the effects of the presence of water in gas-condensate flow in both oil and water-wet porous media should be further evaluated. Lastly, regarding the flow modeling simplifications, the effect of pore wall roughness was not taken into account. This may explain the slight overestimation of the predicted liquid relative permeabilities.

5.2

Pore-network model applications

In Section 5.1, the capability of the proposed model to represent gas and condensate flow in porous media and generate suitable relative permeability curves for macro-scale simulation was verified. In this section, additional applications for the pore-network model for gas-condensate flow are proposed, involving the evaluation of enhanced recovery methods. The evaluation of wettability alteration in gas-condensate reservoirs is presented in Section 5.2.1. The results presented in this section have been published in the journal *Energies*, in an article entitled: "Pore-Scale Analysis of Condensate Blockage Mitigation by Wettability Alteration" [71]. Section 5.2.2.7 presents the evaluation of possible scenarios for condensate bank removal by gas injection. These results are currently being prepared for publication.

5.2.1

Wettability alteration in gas-condensate reservoirs

As discussed in Section 2.3.2 and showed in Section 5.1.6, liquid accumulation in porous media during gas-condensate flow can impact severely gas productivity. When the reservoir pressure is reduced below the dew point, even

lean gas-condensate mixtures can lead to sharp declines in production, as long as condensate saturations buildup due to the liquid reduced mobility [31].

This issue could be mitigated by altering the reservoir rock wettability to intermediate or preferential gas-wet. Reducing the tendency of liquid to spread on the rock porous surface could improve condensate mobility and reduce its accumulation after condensate dropout. In the past two decades, plentiful research effort has been directed to developing gas wettability inducing chemicals and testing their suitability for application in reservoir rocks [72, 73, 74]. Strong indicatives of improved gas-liquid flow performance have been reported [75, 76, 77], with minimal impact on the medium absolute permeability [78, 79], effectiveness at high temperatures [80, 81, 82] and permanent results [83, 30].

Works investigating the effects of wettability change on gas-liquid flow in porous media conventionally resort to spontaneous imbibition and forced flow in cores, using water/oil as the liquid phase and air as the gaseous phase. While these experiments may be adequate to analyze the tendency of well fluid invasion in the reservoir, they do not represent properly condensate dropout and accumulation [84]. Only a few studies include flooding experiments in wettability altered cores using model fluids that flash into two phases under experimental conditions [85, 86, 87, 79, 84]. Their results suggest that the beneficial effects of wettability alteration on gas-condensate flow in porous media are dependent on interfacial tension and flow rate. Hence, generating data regarding condensation and two-phase flow under reservoir conditions is essential for predicting the outcome of wettability alteration for condensate blockage prevention.

With this purpose, pore-network modeling could be employed, as a way of avoiding flow experiments of complex fluids under high pressure and high temperature conditions. As of today, only the model proposed by Li and Firoozabadi [61] presented an analysis of the effect of wettability on critical condensate saturation (S_{cc}) and relative permeability curves. They noticed significant increase in the relative permeability of both phases and reduced S_{cc} , when switching from strongly liquid-wet to intermediate gas-wet. Their model, however, employs a very simplistic condensation mechanism, based solely on a pore throat radius threshold, and unrealistic phases configuration in the porous medium, without the formation of wetting films. Therefore, in order to improve the numerical analysis of wettability alteration in gas-condensate reservoirs, we propose to expand the pore-network model presented in Chapter 4 to encompass condensation and two-phase flow in intermediate and preferential gas-wet media. As a theoretical basis for the model expansion, next section presents a review of condensation and gas-liquid flow in gas-wet

microchannels.

5.2.1.1

Condensation and gas-liquid flow in gas-wet microchannels

Modeling condensate dropout and gas-condensate flow in porous media after wettability alteration relies on the identification of physical phenomena involved in condensation and two-phase flow in gas-wet microchannels. Yet, the impact of wall hydrophobicity on condensation flow has received very little attention in the literature [88]. Chen and Cheng [89] investigated condensation of steam in silicon microchannels. They observed dropwise condensation at hydrophobic channel walls, followed by droplet coalescence and blockage of the channel. Formed liquid slugs were then advected by vapor, developing an intermittent flow. Similarly, Fang *et al.* [88] studied steam condensation on microchannels with different hydrophobicity degrees. They observed dropwise condensation on hydrophobic walls, while hydrophilic microchannels were covered by a stable thin liquid film during phase change. As condensation on gas-wet walls progressed, liquid droplets either grew enough to be dragged by the gas flow or, more commonly, were swept by bigger liquid slugs moving from upstream. Cubaud *et al.* [90] analyzed two-phase flow in microchannels with surface modifications and verified that liquid-gas flows in hydrophobic channels were very different than the ones observed in hydrophilic channels. In gas-wet channels, both phases flowed in slugs that spanned the entire cross section of the channels, exhibiting the same superficial velocity. Liquid films were absent during flow in hydrophobic channel walls, regardless of the observed void fraction. Wu and Djilali [91] investigated water droplet dynamics in a hydrophobic air flowing microchannel. It was identified that, at low Reynolds number ($Re \approx 60$) air flow, drag force on water droplets is minimal, allowing droplets to grow until the channel is obstructed and subsequently be convected by air flow. Santos and Kawaji [92] investigated numerically wetting effects in microfluidic slug flow. They verified that the significant velocity slip developed in hydrophilic microchannels [93, 94, 95] is absent when the channel walls are hydrophobic, since gas slugs completely fill the channel cross section.

5.2.1.2

Conductances for flow in gas-wet media

Based on the works presented in Section 5.2.1.1, dropwise condensation is presumed in the capillaries representing gas-wet porous media, as illustrated in Figure 5.11 (a). Due to the lack of affinity between the solid walls and the liquid, dropped out condensate is collected at droplets that do not spread to

establish a film. Also, since the drag force exerted by the gas flow is insignificant at low Reynolds numbers [91], they do not flow. As the liquid saturation increases, droplets grow and form liquid slugs (Fig. 5.11 (b)) which are either advected by the gas, developing a slug flow pattern (Fig. 5.11 (c)), or block the flow through the capillary, if the pressure difference is not high enough to overcome the capillary pressure.

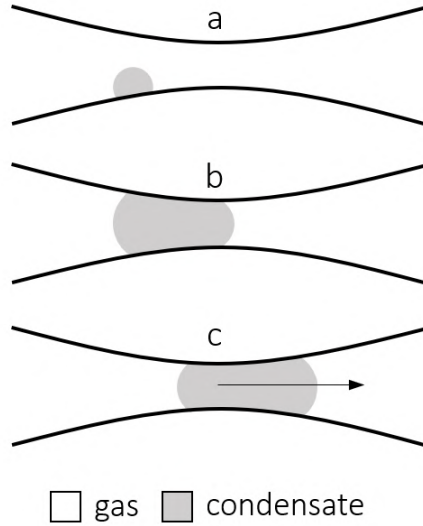


Figure 5.11: Stages of condensation and flow in a gas-wet capillary

In order to simplify the implementation of this condensation mode and flow pattern in the model, it was assumed that slug flow in gas-wet capillaries is established at any non-null value of condensate saturation, i.e. slugs are formed at early condensation stages, where $S_g \approx 1$. The conductances for this flow pattern were calculated based on the pressure drop model proposed by Kashid and Agar [96]. Their model, presented in Equation 5-1, was developed for slug flow in a cylindrical microchannel in the absence of wetting films.

$$\Delta P^{sf} = \frac{8v\mu_w\alpha}{R^2} \frac{L}{l_u} + \frac{8v\mu_{nw}(1-\alpha)}{R^2} \frac{L}{l_u} + \Delta P^{int} \frac{2L-l_u}{l_u} \quad (5-1)$$

where v is the flow superficial velocity, μ_w and μ_{nw} are the viscosities of the wetting and non-wetting phases, α is the wetting phase fraction, l_u is the slug unit length, which comprises the length of one slug plus the length of the space in between slugs, L is the capillary total length, R is the equivalent capillary radius and ΔP^{int} is the interface pressure drop.

Using Eq. 4-5 for the calculation of the interface pressure drop, Eq. 4-3 for the equivalent capillary radius, Eq. 5-1 for the total capillary pressure drop, and considering that only one liquid slug occupies a capillary at a time ($l_u = L$), the conductances for gas and liquid during slug flow are given by Equations 5-2a and 5-2b.

$$g_g^{sf} = \frac{\pi R^4}{8L} \left(\frac{S_g}{S_g(\mu_g - \mu_l) + \mu_l} \right) \quad (5-2a)$$

$$g_l^{sf} = \frac{\pi R^4}{8L} \left(\frac{1 - S_g}{S_g(\mu_g - \mu_l) + \mu_l} \right) \quad (5-2b)$$

In the analyses presented next, gas-wet behavior will be assigned to contact angles $\theta \geq 90^\circ$, using Eq. 5-2, and liquid-wet behavior to $\theta < 90^\circ$, using the conductances previously devised for annular flow, shown in Eq. 3-1.

5.2.1.3

Pore-network description

A pore-network representing a sandstone was used to generate the following results. It was adapted from a network presented by Dong [5], based on micro-CT imaging of a sandstone sample (Figure 5.13(a)). This network, shown in Figure 5.13(b), has a permeability of 169 mD, a porosity of 17.1%, and a total volume of 2.67 mm³. A cubic subsection of 1.75 mm³ from the original network was selected, as shown in Figure 5.13(b) and (c), in order to reduce the computational effort of the flow analyses. In the excerpt from original network, pore body radii and spatial coordinates were maintained, and pore throat radii were used as the R_{min} of the adapted network, as indicated in Figure 5.12. For the definition of R_{max} , the radius of the largest pore body connected to each pore throat was used. Pore throat lengths were set to match the original network porosity and permeability. Histograms of the resulting R_{min} and R_{max} distributions are shown in Figure 5.14.

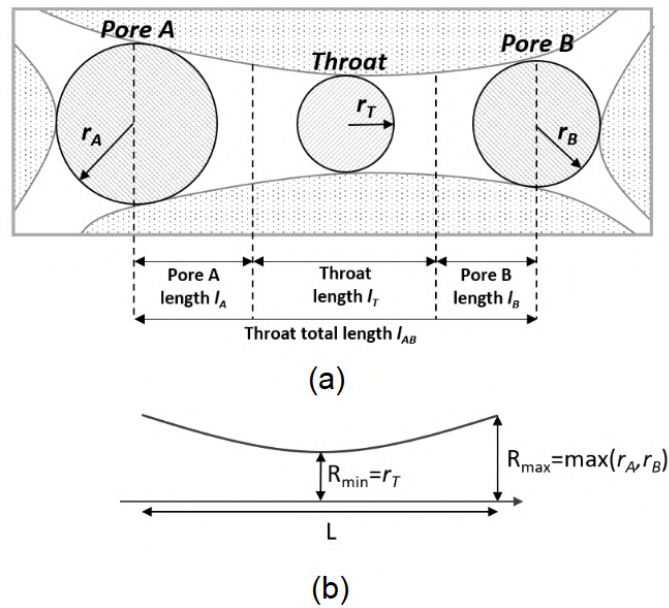


Figure 5.12: (a) Pore body and throat dimensions following the pore-network extraction method proposed by Dong [5]. (b) Pore throat dimensions for the adapted pore-network, based on pore body and throat radii in (a)

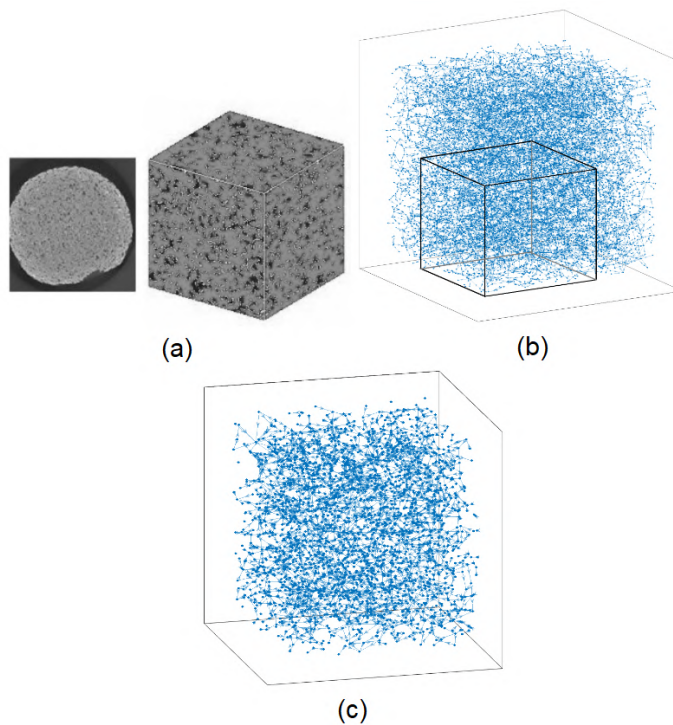


Figure 5.13: (a) Sandstone sample and micro-CT image used to extract the pore-network. Images available on [12]. (b) Pore-network generated with data extracted from the sandstone sample on (a), with used subsection delineated. Data available on [12]. (c) Subsection of the pore-network in (b), adapted for the proposed model.

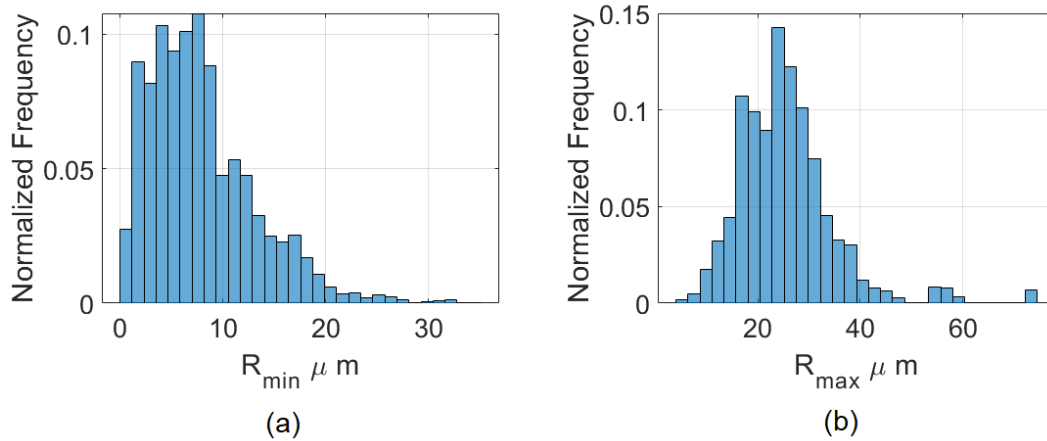


Figure 5.14: Histograms for the radii used in the adapted network. (a) R_{min} . (b) R_{max} .

5.2.1.4 Injected fluid

The composition of the fluid mixture used in the flow analyses is presented in Table 5.3. We devised this composition to represent a typical mixture found in gas-condensate reservoirs, composed by carbon dioxide, light, intermediate and heavy hydrocarbons. This mixture exhibits retrograde condensation behavior in the temperature range from $15^{\circ}C$ to $207^{\circ}C$, as shown in the phase diagram in Figure 5.15, obtained with the CMG software Winprop.

Table 5.3: Fluid mixture composition

Component	Molar Fraction
CO ₂	0.07
C ₁	0.65
C ₂	0.13
C ₃	0.07
C ₆	0.05
C ₁₀	0.025
C ₁₆	0.005

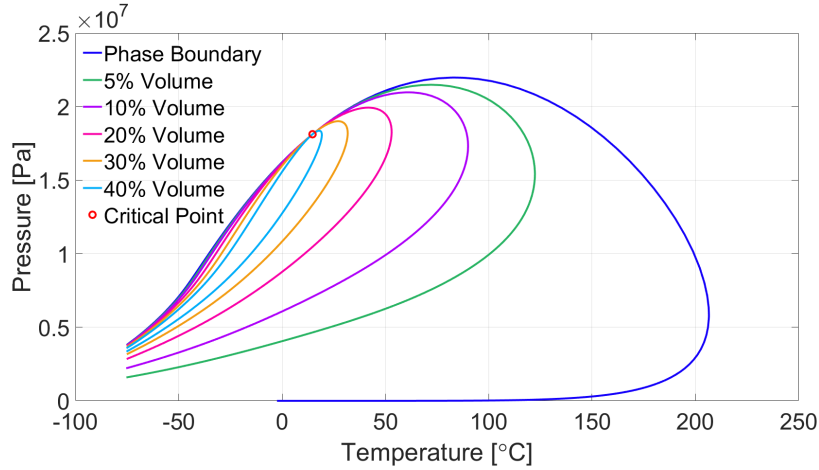


Figure 5.15: Fluid mixture used during the wettability alteration analyses.

5.2.1.5

Flow conditions

In all cases analyzed here, the prescribed boundary conditions were molar flow rate at the network inlet and pressure at the outlet. Different flow rates were used so that gas velocities from $7.5m/day$ to $150m/day$ were achieved in the networks. The positive effect of velocity on gas-condensate flow has been widely reported in the literature [19, 18, 16, 97, 43] for strongly liquid-wet media. By analyzing a wide range of gas flow velocities, we intend to evaluate whether wettability influences the flow rate effect on flow performance.

For each studied flow velocity, different levels of liquid saturation were obtained by changing the pressure at the network outlet. At the temperature of $80^{\circ}C$, chosen for the presented analyses, the fluid properties are presented in Table 5.4. The phases viscosities were calculated with the Lohrenz-Bray-Clark correlation [28], while the interfacial tension was calculated with the Weinaug and Katz correlation [29].

Table 5.4: Fluid properties at the chosen flowing conditions

Label	Pressure [MPa]	Liquid Dropout [%]	μ_g [Pa.s]	μ_l [Pa.s]	σ [mN/m]
P6	21.57	1.17	3.27×10^{-5}	5.58×10^{-5}	0.0196
P5	21.33	3.51	3.2×10^{-5}	5.7×10^{-5}	0.0271
P4	21.84	5.31	3.12×10^{-5}	5.81×10^{-5}	0.0359
P3	20.59	7.86	2.99×10^{-5}	6.04×10^{-5}	0.058
P2	19.61	10.6	2.76×10^{-5}	6.46×10^{-5}	0.1221
P1	17.5	12.12	2.4×10^{-5}	7.29×10^{-5}	0.3501

The effect of wettability alteration was assessed by performing all flow analyses with variable contact angle values. For the evaluation of flow in a rock sample with unaltered wettability and perfectly wetted by the liquid phase, $\theta = 0^\circ$ was used. For wettability altered media, the contact angle range of $45^\circ \leq \theta \leq 135^\circ$ was explored.

Local Reynolds numbers were calculated for all flow conditions and varied between 2.25×10^{-2} and 4.5×10^{-1} . Therefore, even at the highest tested gas flow velocity, inertial effects were not significant.

5.2.1.6 Relative permeability curves

Relative permeabilities were calculated with the Darcy's law for the flow conditions presented in Section 5.2.1.5 under steady-state flow conditions. Figures 5.16, 5.17 and 5.18 show the relative permeability curves obtained with different contact angles at gas velocities of 7.5m/day , 45m/day and 150m/day , respectively.

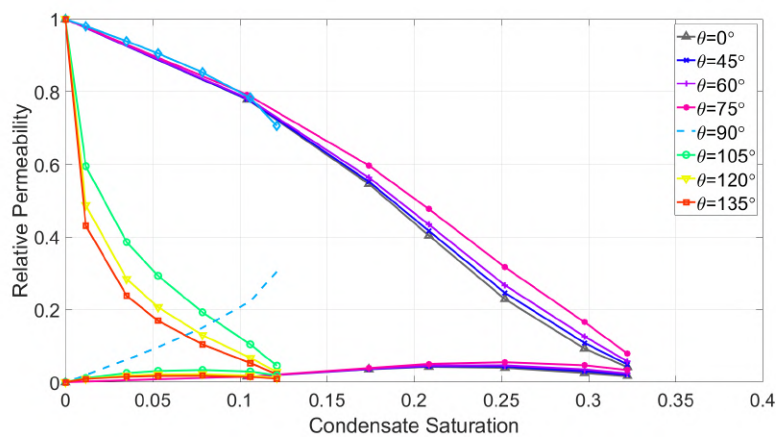
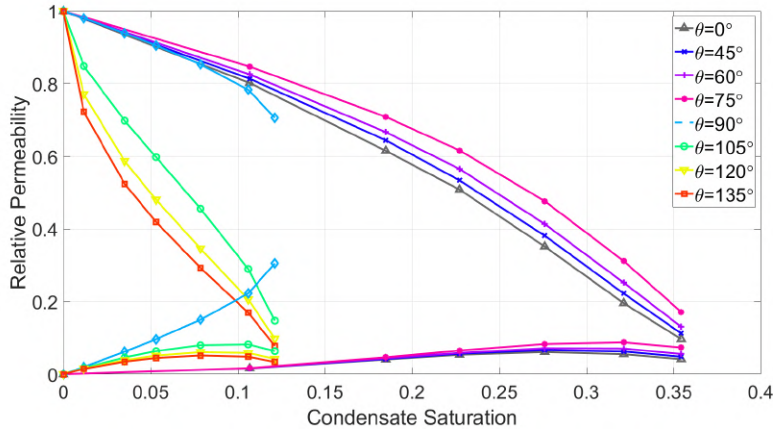
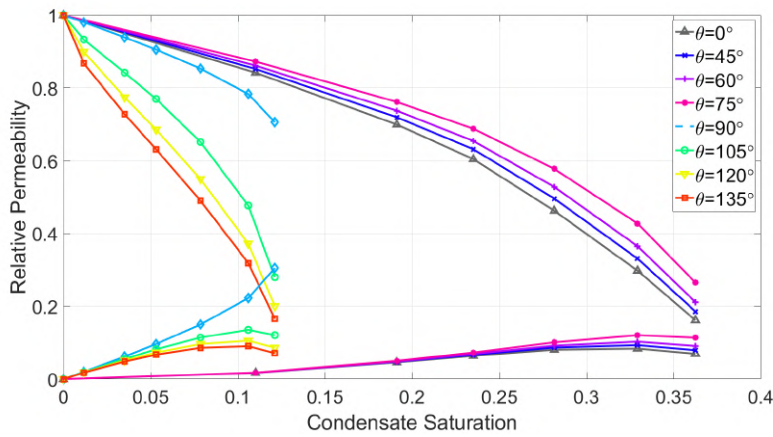


Figure 5.16: Relative permeability curves for $v_g = 7.5\text{m/day}$

Figure 5.17: Relative permeability curves for $v_g = 45\text{m/day}$ Figure 5.18: Relative permeability curves for $v_g = 150\text{m/day}$

Very distinct curves were obtained for flow through porous media with contrasting wettability, due to the different condensation modes and flow patterns attributed to gas and liquid-wet cases. For $0^\circ \leq \theta < 90^\circ$, which corresponds to preferentially liquid-wet media, condensate accumulation occurs. In these cases, the liquid tends to flow adjacent to pore walls, while the gas flows in channel cores. As a consequence, a significant velocity slip is developed between the phases and liquid saturation builds up. This effect is noticeable in Figures 5.16 to 5.18: while the maximum liquid dropout for the flowing conditions is 12.12%, the maximum condensate saturation in the networks, at steady-state flow, is approximately 35%. A notably dissimilar behavior is exhibited by the curves obtained for the gas-wet cases, $90^\circ \leq \theta \leq 180^\circ$. Since it is considered that liquid and gas flow at the same superficial velocity during slug flow, no liquid accumulation occurs. For this reason, the range of condensate saturations covered by these curves is equivalent to the mixture

liquid dropout. Significant differences in condensate saturation for the same flow conditions and different wettabilities, consistent with the results obtained with the proposed model, were also observed experimentally by Fahimpour *et al.* [84].

When compared to the base case with unaltered wettability, $\theta = 0^\circ$, the flow with contact angles of 45° , 60° and 75° led to improvements in both gas and condensate relative permeabilities, for all analyzed pressure levels and flow rates. Even though condensate accumulation still took place in those cases, the interface pressure drop (eq. 4-5) was reduced, lowering the pressure drop between the inlet and outlet of the networks. Similar trends of increase in relative permeability for both phases were reported by Zhang *et al.* [98] and Fahimpour *et al.* [79]. On the contrary, at fixed saturation levels, the values of gas relative permeability obtained in gas-wet media are significantly lower than the ones obtained in the base case, especially at the low flowing velocities. For these cases, only liquid relative permeabilities are higher than the ones achieved in strongly liquid-wet media. This translation of relative permeability curves to the left has been repeatedly reported in the literature for two-phase flow in cores with wettability altered from liquid to gas-wet [14].

Curves for $\theta = 90^\circ$ were also included in Figures 5.16 to 5.18. The condensation and flow behavior for gas-wet media was assigned for this case, so no liquid accumulation took place. For fixed saturations, improvement in gas relative permeability was only noticed at low flow rates, while liquid relative permeability increased significantly for all tested flow conditions.

The positive effect of flow rate in relative permeability was observed for all contact angles used in the analyses, except for the neutral wettability case. This effect is a result of the interplay between viscous forces and capillary forces in gas-condensate flow. As the flow rate is increased, viscous forces gain significance when compared to capillary forces, and fewer flowing paths remain blocked with liquid. Hence, since the capillary pressure for $\theta = 90^\circ$ is equal to zero, this gradual effect does not happen. Another aspect noticed in the curves related to all cases other than $\theta = 90^\circ$ is the negative effect of interfacial tension rise as the pressure is depleted. This effect is particularly apparent in liquid relative permeability curves, which can decline even at increasing liquid saturations, if the interfacial tension increment is high enough.

Further analyses of the parameters affecting gas and condensate relative permeabilities in wettability altered porous media are presented in Section 5.2.1.7.

5.2.1.7

Improvement factor

Very few experimental studies assessing the effect of wettability alteration on condensate banking provide relative permeability curves as a function of saturation. During coreflooding experiments, the fluid mixture undergoes phase transitions and compositional shifts that make saturation determination highly challenging. As a result, the effect of wettability alteration is commonly evaluated by calculating improvement factors.

The improvement factor (IF) is the ratio between gas relative permeabilities after and before wettability change, for the same injection flow conditions. Kumar *et al.* [85] presented results for flow of mixtures that flashed into two phases in sandstone cores. At experimental conditions, the interfacial tension was approximately $4mN/m$ and IFs varied between 2 and 3. Bang *et al.* [86] evaluated the effect of wettability alteration in a sandstone core at higher interfacial tension conditions ($\approx 12mN/m$) and reached IFs between 3 and 4. Other authors reported IF in the range 1-2, for both sandstone and carbonate cores [99, 100, 101], but no details of the fluid properties were discussed.

Those works focus primarily on evaluating the effects of different wettability altering treatments and core properties, and rarely correlate improvement factors with fluid properties and flowing conditions. Fahimpour *et al.* [84] evaluated the effect of interfacial tension and flow rate on the flow improvement measured in wettability altered carbonate cores. Under the experimental conditions, contact angles decreased monotonically with interfacial tension, and corresponded to 65° , 44° and 30° for $\sigma = 10$, 3 and $1mN/m$, respectively. They measured averaged IFs of 3 for tests at $\sigma = 10.8mN/m$, 1.3 for $\sigma = 2.7mN/m$ and 1.1 for $\sigma = 0.77mN/m$, which indicates a significant effect of fluid properties on flow improvement via wettability alteration.

To evaluate thoroughly the effects of wettability, fluid properties and flow velocity on improvement factor, a wide range of flow conditions and contact angle values was examined with the proposed model. Improvement factors calculated for all analyses are shown in Figure 5.19. Gas flow velocities of 7.5, 15, 30, 45, 60, 90 and 150 m/day are denoted as $Q1$ to $Q7$, while the pressures represented in Table 5.4 are labeled, in ascending order, as $P1$ to $P6$.

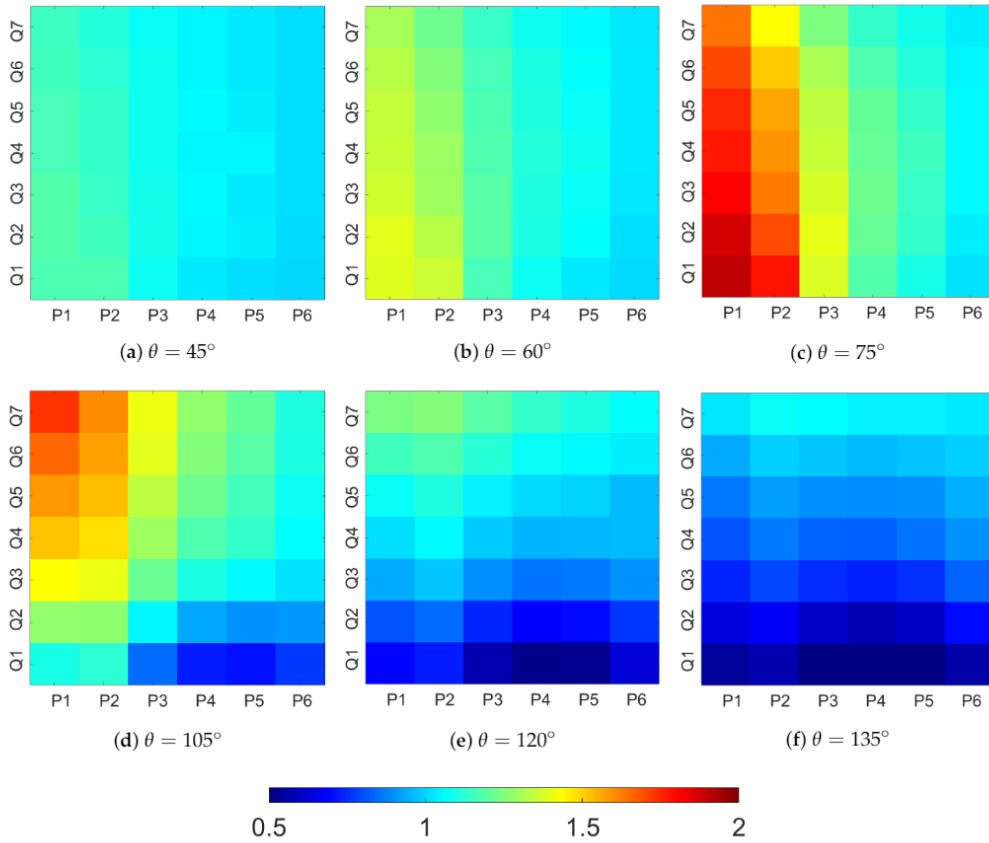


Figure 5.19: Improvement factors for all tested flowing conditions

The impact of liquid saturation and interfacial tension reported by Fahimpour *et al.* [84] is apparent in Figure 5.19. At lower pressures, which are associated with higher interfacial tensions and liquid saturations, higher improvement factors were achieved. This happens because an important effect related to wettability alteration is the reduction of interface pressure drop (eq. 4-5). Thus, if interfacial tension and liquid saturation are negligible, this effect becomes less prominent and IFs tend to be lower.

Also evident in Figure 5.19 is the influence of the degree of wettability alteration on IFs. For both gas and liquid-wet cases, contact angles closer to 90° produced more significant improvements, since the reduction of interface pressure drop is greater. Besides, it is noticeable that, for $\theta > 90^\circ$, IFs may be lower than one, especially at high pressures and low flowing rates. This is related to the different condensation modes and flow patterns observed in gas-wet and liquid-wet media. At low liquid saturations, condensate tends to be collected on films on pore walls, if the medium is liquid-wet. In this configuration, the negative effect of liquid accumulation on gas flow is less severe, as gas flowing paths are reduced, but not blocked. For the gas-wet

case, however, we consider that even at low liquid saturations, liquid slugs are formed. Therefore, by altering the wettability, a negative effect may occur. This effect is more pronounced at low flow rates, as even small liquid slugs can obstruct the flow under weak acting viscous forces.

The fact that more pore throats contain liquid slugs in gas-wet media also intensifies the impact of flow rate on improvement factors, as seen in Figures 5.19 (d) to (f). Since the positive coupling between flow velocity and relative permeability is linked to the ability of viscous forces to overcome capillary forces, more liquid collected on slugs amplifies the effect. As for liquid-wet media, the flow rate effect is not only weaker, but also non monotonic. At low pressure levels improvement factors tend to decrease with flow rate, while at high pressures the effect can be either positive or negative. Independently of wettability preference, for high flow rates occurring in the near wellbore region, all tested contact angles led to improvement factors higher than one, indicating flow enhancement.

5.2.1.8

Liquid accumulation and compositional shift

Apart from improvement factors, an important aspect related to wettability alteration for gas-condensate enhanced production involves the fluid phase behavior in the near wellbore region. In liquid-wet porous media, gas develops superior superficial velocities than condensate, leading to liquid accumulation. As a result, valuable heavier hydrocarbon components from the fluid mixture are trapped in the subsurface and the fluid phase behavior is altered. Figure 5.20, obtained with the CMG software Winprop, shows the phase boundaries and critical points for the original injected composition (table 5.3) and for the mixtures contained in the liquid-wet networks during steady-state flow at pressures $P1$ to $P6$ (table 5.4).

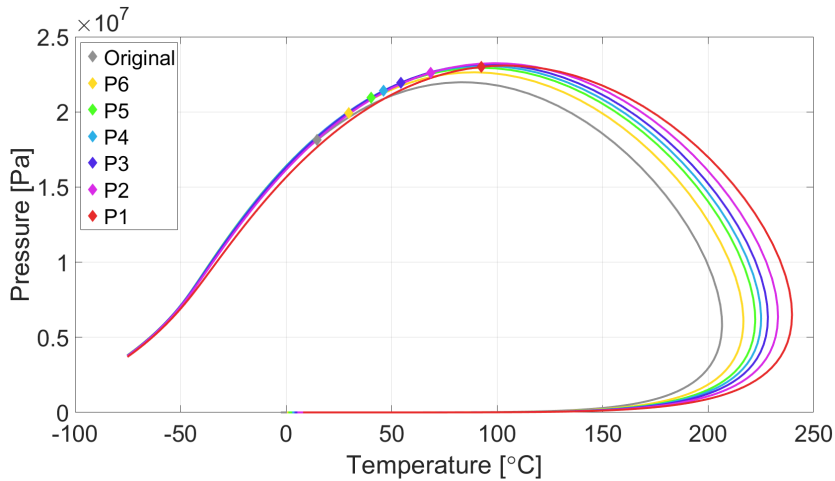


Figure 5.20: Phase envelope shift due to liquid accumulation

As the pressure is lowered, the fluid mixture becomes richer in heavier components and the phase envelope is shifted to the right. Consequently, not only the liquid saturation builds up, but the fluid mixture tends to turn into volatile oil. Such a transition is observed in the envelope related to pressure P_1 in Figure 5.20, where the critical temperature is 92°C , higher than the test temperature of 80°C . This affects negatively long-term well deliverability, since further depletion in the reservoir will not vaporize the deposited condensate, as predicted by the phase diagram related to the original composition (fig. 5.15).

For gas-wet media, the tendency of gas and condensate to flow at the same superficial velocity can preserve the original reservoir fluid composition around producing wells. Therefore, depletion beyond the pressure related to maximum liquid dropout, $P_6 = 17.5\text{MPa}$ for the tested composition, will lead to progressively lower liquid saturations and possibly more favorable producing scenarios.

5.2.1.9

Discussion

For the evaluation of wettability effects on gas-condensate flow in porous media, two different condensation modes and flow regimes were associated to preferentially liquid wet media ($\theta < 90^\circ$) and preferentially gas-wet media ($\theta \geq 90^\circ$). The implemented flow patterns are consistent with experiments involving condensation and two-phase flow visualization in hydrophilic [93, 94, 95] and hydrophobic [89, 88, 90, 91] microchannels. To the best of our knowledge, this is the first pore-network model for thermodynamically consistent condensation flow that takes into account the effect of wettability on flow pattern.

We believe, however, that the sharp transition in flow behavior observed at $\theta = 90^\circ$ in the model is not entirely realistic. For instance, the formation of wetting films on preferentially liquid-wet media with contact angles close to 90° may not take place at very low liquid saturations. Moreover, condensation in preferentially gas-wet media may not form liquid slugs that span the entire flowing channels cross-sections at low liquid saturations. Therefore, implementing a transitional flow behavior for neutral wettability [89], as well as a minimum saturation for liquid slug formation in gas-wet media, could potentially further improve the results and should be considered for future work.

Finally, we consider that the gas-condensate fluid system adopted in Section 5.2.1.4 may not be ideal to realistically represent gas-condensate fluid mixtures naturally occurring in reservoirs. Therefore, conducting the presented analyses with a more realistic composition, using fluid properties tuned based on real PVT laboratory data, should also be considered for future work.

5.2.2

Gas injection in gas-condensate reservoirs

Enhanced recovery methods involving gas injection in gas-condensate reservoirs have also been largely investigated in the past two decades. For such methods, the main objectives comprise full or partial pressure maintenance in the reservoir, as well as re-evaporation of accumulated condensate.

In full pressure maintenance, the reservoir pressure is kept above the dew point pressure and liquid dropout is prevented. If feasible, this method can maximize condensate recovery, as no liquid phase is deposited in the porous medium and heavy components are produced in the gas. Luo *et al.* [102] conducted long-core flooding experiments with lean gas injection to compare recoveries above and below the dew point pressure. While injection below the dew point managed to re-vaporize a fraction of both intermediate and heavy hydrocarbons in the core, condensate recovery was considerably higher for the case above the dew point. Implementing a full pressure maintenance scheme, however, requires large amounts of injected gas and can be unpractical for cases in which the initial reservoir pressure is close to the fluids dew point [102]. Also, special attention has to be directed to the injected gas composition. Certain gases, such as nitrogen [102] and methane [103], have a tendency to increase gas-condensate mixtures dew point and can lead to early condensation in the reservoir.

For the case of partial pressure maintenance, gas can be injected following liquid dropout in the reservoir. In this approach, the objectives are both slowing

down pressure depletion and re-vaporizing the accumulated condensate, so that gas flowing paths are cleared and valuable heavy components are recovered. Numerous studies have investigated the ability of different gas compositions to support reservoir pressure and reduce liquid banking. Al-Anazi *et al.* [104] evaluated the effectiveness of methane to recover condensate using coreflooding experiments. They concluded that methane is able to re-vaporize the liquid phase and restore the core's original permeability, but that tens to hundreds of injected pore volumes can be required for the method's success. High injection pressures and flow rates were pointed out as means to accelerate the method's outcomes. Gachuz-Muro *et al.* [105] performed core flooding experiments to investigate the recovery obtained with gas injection in naturally fractured gas-condensate reservoirs. A small gap was allowed around the core to simulate a fracture and, after the core was depleted below the dew point pressure, N_2 , CO_2 and lean gas were injected. The results indicated a condensate recovery of 51.7% with the lean gas injection, 34.78% with CO_2 and only 18.7% with the N_2 injection case. Al-Abri *et al.* [106] evaluated condensate recovery by the injection of super-critical CO_2 , methane, and their mixtures. They performed gas injection in a sandstone core following condensate flooding, meaning that the liquid content was not established in the porous medium by condensation. Unsteady-state relative permeability and recovery measurements demonstrated that the injection of pure CO_2 delayed the gas breakthrough and provided higher recovery of condensate when compared to the injection of mixtures of CO_2 and pure methane, at the same operating conditions. Besides conventional gas flooding, huff-n-puff gas injection has also been investigated experimentally, for application in shale gas-condensate reservoirs. Due to shale ultra low permeabilities, this technique could be beneficial to expedite both pressure boost and re-evaporation of condensate in the producing wellbore vicinity [107]. Core flooding experiments in shale cores displayed promising results for the huff-n-puff injection of produced gas [108], methane [109] and CO_2 [110].

Additionally to core flooding tests, several reservoir-scale numerical studies have been conducted to assess gas injection as an enhanced gas-condensate recovery method. Marokane *et al.* [111] used a full-field compositional reservoir simulation model to investigate the efficacy of a one-time lean gas injection scheme to remove the condensate banking around producing wells. Results indicated that, for a lean gas reservoir, maximum recovery was obtained for injection at pressures below the maximum liquid dropout. For a rich gas reservoir, however, starting gas injection before reaching the maximum liquid dropout pressure produced better results. Linderman *et al.* [112] used a similar

approach to evaluate the feasibility of injecting nitrogen in a gas-condensate reservoir. Their model predicted superior net gas production with the injection of nitrogen than with the injection of produced gas, while the condensate net recovery was virtually identical for the two scenarios. They also compared the injection of CO_2 with N_2 , finding no significant differences in the achieved recoveries. Taheri *et al.* [113] modeled enhanced condensate recovery in fractured gas-condensate reservoirs using stock tank gas, methane, N_2 and CO_2 injection. Results suggested that CO_2 injection could generate considerably better results than the other tested gases, and that no appreciable difference is obtained between the injections of methane, nitrogen and stock-tank gas. It was also concluded that injection at higher pressures boosted condensate recovery. Another numerical study evaluating gas injection in fractured gas-condensate reservoirs was conducted by Fath *et al.* [114]. After testing four different injected gas compositions, they obtained the highest recovery with CO_2 , followed by methane, produced gas and nitrogen. Their model also predicted that, for the same injected volumes of the tested gases, nitrogen led to a significant higher pressure average in the reservoir, while produced gas led to the lowest. Recent numerical works also investigated the efficacy of ethane injection for condensate recovery, with very favorable results. Sharma and Sheng [115] evaluated the performance of huff-n-puff gas and solvent injection in shale gas-condensate reservoirs. They concluded that ethane was the best injection fluid on accounts of higher and much faster recovery, when compared to methane, methanol and isopropanol. The positive results were attributed to ethane's ability to greatly reduce the gas-condensate mixture's dew point pressure, ensuring relatively low injecting volumes for condensate re-vaporization. Zhang *et al.* [116] investigated the injection of ethane, methane, CO_2 and N_2 in a five-spot scheme for condensate enhanced recovery. In their study, ethane also led to the best condensate recovery, of 56.8% after the injection of 0.85 pore volumes, closely followed by CO_2 , with a recovery of 50.7%. Methane and nitrogen displayed considerably worse performances, with 22.8% and 21.3% of condensate recovery, respectively, for the same injected volume.

Although both experimental and numerical research indicate that gas injection is an advantageous approach for condensate enhanced recovery, no pore-scale analysis of the method has been reported in the literature. This represents a significant gap in data for gas injection performance evaluation, especially considering that pore-scale events are essential to understanding macro-scale transport properties in porous media. During gas injection, local changes in composition can alter significantly both bulk and interfacial properties of gas and liquid phases, which in turn affect their flow, characterized

by the relative permeability curves.

In order to address this gap, we employed the compositional pore-network model proposed in Chapter 4 to evaluate gas injection in porous media after condensate accumulation. For this study, no alterations had to be implemented in the presented mathematical formulation. Sections 5.2.2.1 to 5.2.2.3 contain the description of the pore-network, fluids and flow conditions used in the study. In the subsequent result sections (5.2.2.4 to 5.2.2.6), final saturations, recovery of heavy hydrocarbon components and gas relative permeabilities were quantified to compare the efficacy of each gas injection scenario.

5.2.2.1

Pore-network description

The pore-network used to to evaluate gas injection as a gas-condensate enhanced recovery method was the same presented in Section 5.2.1.3. It represents a sandstone sample, with permeability of 169 mD and porosity of 17.1%.

5.2.2.2

Injected fluids

A series of fluid mixtures was used in the present study in order to represent condensate buildup in porous medium followed by gas injection and condensate re-vaporization. The composition of the fluid used during the condensate accumulation process in the porous medium is presented in Table 5.5. This mixture represents a typical fluid found in gas-condensate reservoirs, composed by carbon dioxide, nitrogen, light, intermediate and heavy hydrocarbons. It exhibits a large window of retrograde condensation behavior in the temperature range from $12^{\circ}C$ to $207^{\circ}C$, as shown in the phase diagram in Figure 5.21. For our analyses, a temperature of $60^{\circ}C$ was chosen as the reservoir temperature.

Table 5.5: Gas-condensate mixture composition.

Component	Molar Fraction
CO_2	0.05
N_2	0.02
C_1	0.65
C_2	0.13
C_3	0.07
C_6	0.05
C_{10}	0.025
C_{16}	0.005

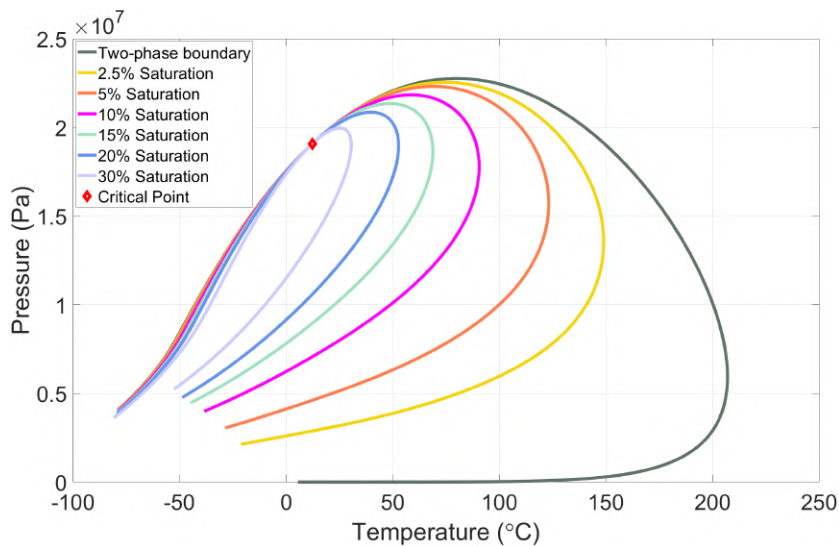


Figure 5.21: Fluid mixture phase envelope

Gas mixtures rich in methane (C_1), ethane (C_2), carbon dioxide (CO_2) and nitrogen (N_2) were chosen as the candidates for condensate enhanced recovery. For the sake of appraising preliminarily the ability of these gases to re-vaporize condensate, Figures 5.22 to 5.24 illustrate the liquid dropout as a function of pressure obtained by mixing pure C_1 , C_2 , CO_2 or N_2 with the composition presented in Table 5.5, at different molar fractions and a temperature of $60^\circ C$. It can be noticed from Figure 5.22 that the addition of 25% in moles of the tested gases to the reservoir composition leads to a substantial reduction in maximum liquid dropout, varying from 31.8%, in the case of C_2 , to 49.6%, in the case of C_1 . It is also noticeable that the effects of the tested gases on the mixture's dew point pressure are very distinct. C_2 and CO_2 reduce the saturation pressure, thus allowing the mixture to remain as a single gas phase at lower pressures. The opposite is verified as the reservoir

fluid is mixed with C_1 and N_2 . While the negative effect of C_1 on the dew point pressure is mild, N_2 increases significantly its value, and can lead to very early condensation in porous media. The same trend of effects is observed as the content of the tested gases is increased to 50%, Figure 5.23, and 75%, Figure 5.24. The maximum liquid dropout is progressively reduced, with C_1 and CO_2 being the most, and C_2 and N_2 the least effective gases to lower the maximum volume of liquid formed. As for the effects on the dew point pressure, at higher molar fractions C_2 and CO_2 gradually reduce it, while N_2 increases it. C_1 , on the other hand, slightly augments and then reduces the mixture's dew point pressure, at the molar proportions of 50% and 75%, respectively. These results suggest that mixtures rich in C_1 , C_2 , CO_2 and N_2 have a positive prospect to work as condensate re-vaporization agents and, consequently, improve gas flow in porous media. Nonetheless, the negative effect of C_1 and N_2 on the mixture dew point pressure must be carefully examined, as it can lead to an early, and more extensive, formation of a condensate bank in the near wellbore region.

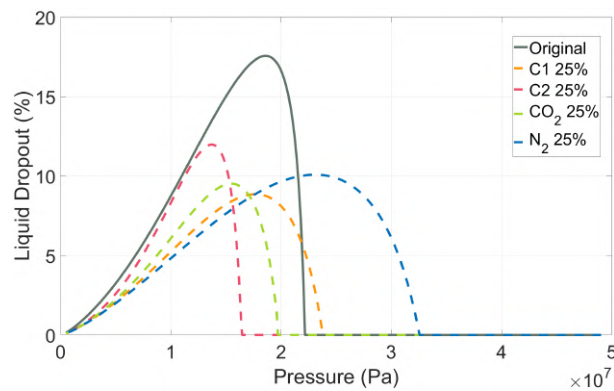


Figure 5.22: Liquid dropout at 60°C, with 75% of the gas-condensate mixture and 25% of the injected gases, in moles

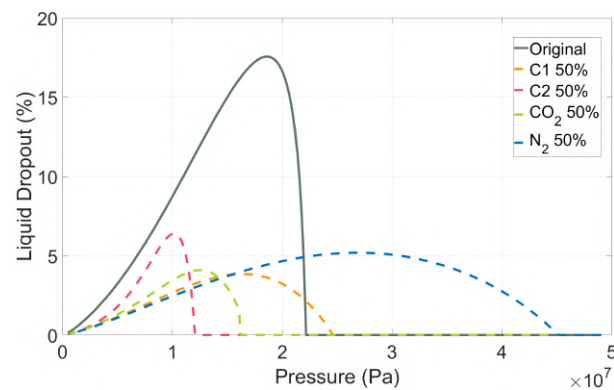


Figure 5.23: Liquid dropout at 60°C, with 50% of the gas-condensate mixture and 50% of the injected gases, in moles

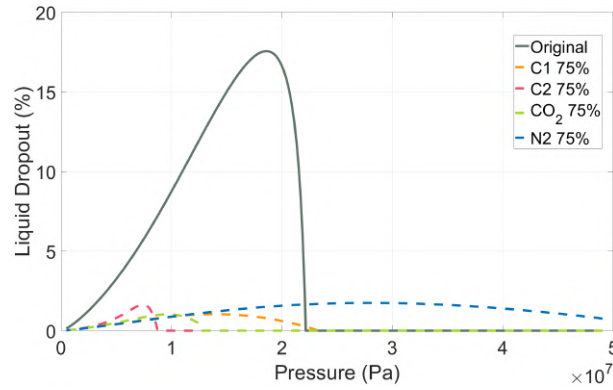


Figure 5.24: Liquid dropout at 60°C, with 25% of the gas-condensate mixture and 75% of the injected gases, in moles

For the gas injection analyses presented next, mixtures of C_1 , C_2 , CO_2 and N_2 with the reservoir fluid, at molar proportions of 50% and 99%, were injected in the networks after condensate accumulation. The gas injection at a molar percentage of 99% was used to represent, to an acceptable degree, the injection of pure gases in the reservoir, while avoiding numerical issues in the model. Attempts to inject gases at a molar percentage of 100% in the networks led to continuously declining concentrations of the components previously accumulated in the pores, which eventually compromised the solution of the governing equations presented in Section 4.4.4. This issue was avoided by adding 1% of the original reservoir composition in the injection mixture. The tests of gas injection at a molar proportion of 50% were performed considering two different scenarios. First, to take advantage of the produced gas availability, we wanted to test whether injecting mixtures of the produced gas with C_1 , C_2 , CO_2 or N_2 could enhance condensate recovery. As seen in Figure 5.23, these mixtures, on average, reduced to a third the maximum liquid dropout obtained with the reservoir composition and could, as a consequence, be suitable to improve gas flow. Secondly, even during the injection of pure gases, the flow of mixtures of injected and reservoir fluids will take place, especially at regions far from the injection wells and/or at small injection volumes. These cases, therefore, serve also to appraise the effects of dilution in the performance of C_1 , C_2 , CO_2 or N_2 to recover condensate.

5.2.2.3

Flow conditions

Two steps of injection were performed in the network for every evaluated case. First, the reservoir fluid was injected so that condensate accumulated in the porous medium, mimicking the process of condensate banking in the near

wellbore regions. Then, the injected composition in the networks was altered, so that the liquid buildup was followed by gas injection and condensate recovery.

The process of condensate accumulation was reproduced by injecting the mixture presented in Table 5.5 in the networks at different pressures. As the timing for gas injection is one of the most relevant parameters for the method's success [111], we wanted to test its performance at various reservoir depletion stages. Six pressure values were used, 22, 21.5, 21, 19.5, 17.75 and 14.75 MPa, which corresponded to liquid dropout saturations of 2.3%, 9.7%, 13.3%, 17.1%, 17.3% and 14.7%, respectively. Therefore, at the beginning of the step of reservoir fluid injection, these were the initial condensate saturations in the network, which increased during the liquid accumulation process. With that, a broad range of depletion scenarios could be covered, from the early stages of condensate formation to pressures below the maximum liquid dropout.

After liquid accumulation, the mixtures containing C_1 , C_2 , CO_2 or N_2 were injected in the the networks. This step lasted until the recovery reached a steady-state, or until the time of injection reached $t_{inj}^{max} = 300s$. Under certain conditions, the recovery of heavy components by gas injection can be a very slow process, requiring tens to hundreds of pore volumes injected [104]. For this reason, we set a maximum time for injection, restraining each studied case within a reasonable running time.

The prescribed boundary conditions for both steps were molar flow rate at the network inlet and pressure at the outlet. For all tested injection scenarios, a molar flow rate of 10^{-6} moles/s was imposed. It has been reported in the literature [104] that injection rate does not influence significantly the performance of gas injection as a gas-condensate EOR method and we chose, therefore, not to explore the effects of this parameter.

5.2.2.4

Condensate saturation reduction

Figures 5.25 to 5.30 illustrate the evolution of the condensate saturation in the networks with time during both steps of injection, i.e. the injection of the reservoir fluid and the injection of tested gases, for the cases with molar proportion of 99% at the different evaluated pressures. Therefore, these curves represent both the condensate buildup during the injection of the reservoir fluids and the condensate recovery during gas injection.

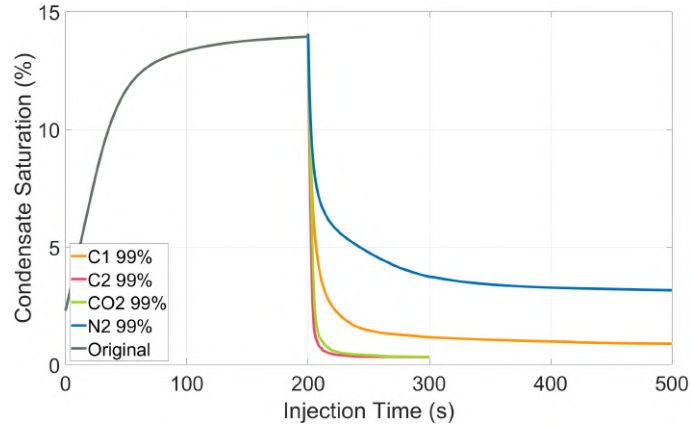


Figure 5.25: Condensate saturation during the injection of gases with 99% molar concentration, at $P=22$ MPa

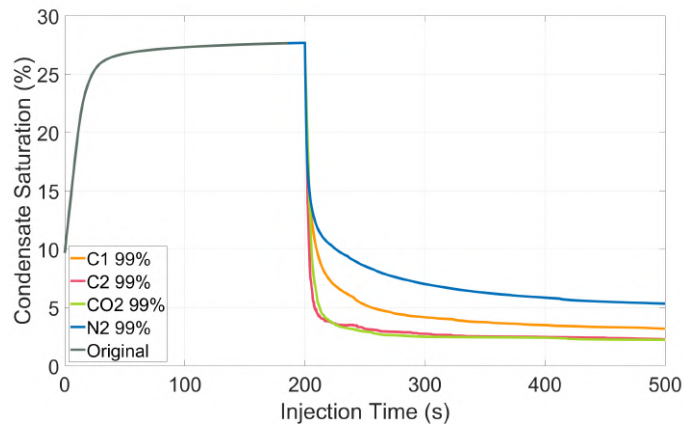


Figure 5.26: Condensate saturation during the injection of gases with 99% molar concentration, at $P=21.5$ MPa

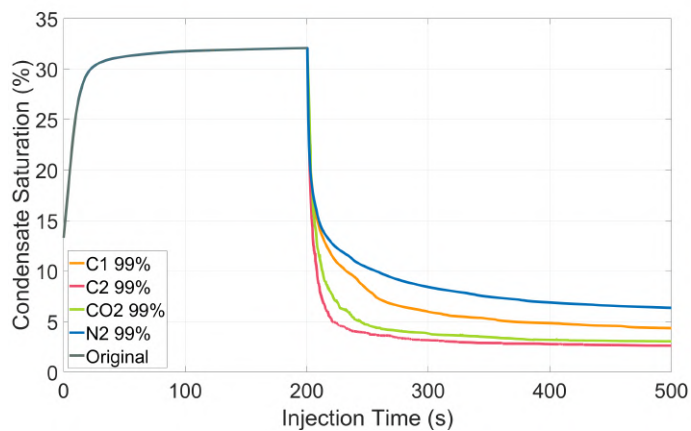


Figure 5.27: Condensate saturation during the injection at of gases with 99% molar concentration, $P=21$ MPa

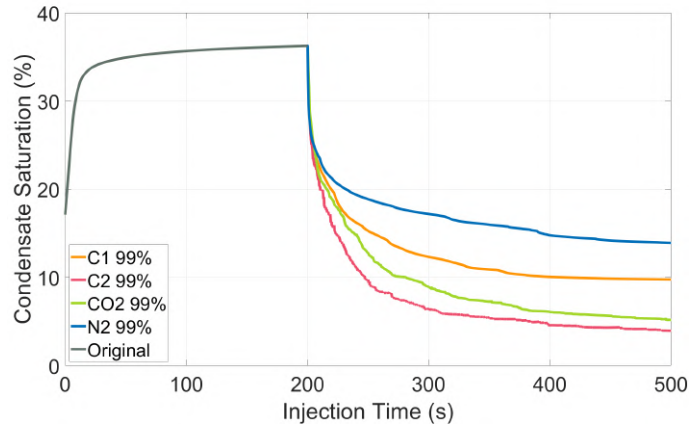


Figure 5.28: Condensate saturation during the injection at of gases with 99% molar concentration, $P=19.5$ MPa

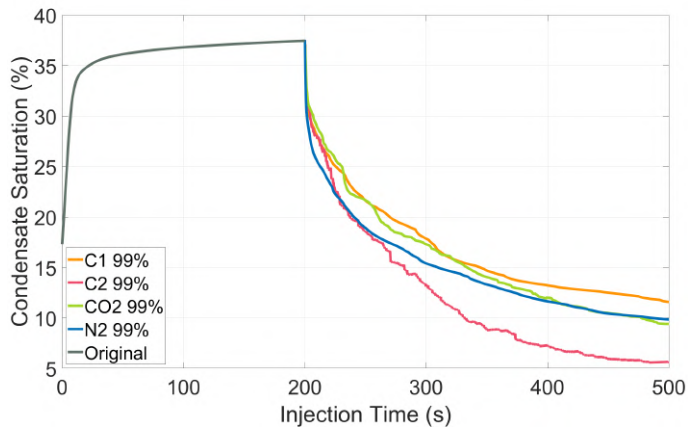


Figure 5.29: Condensate saturation during the injection at of gases with 99% molar concentration, $P=17.75$ MPa

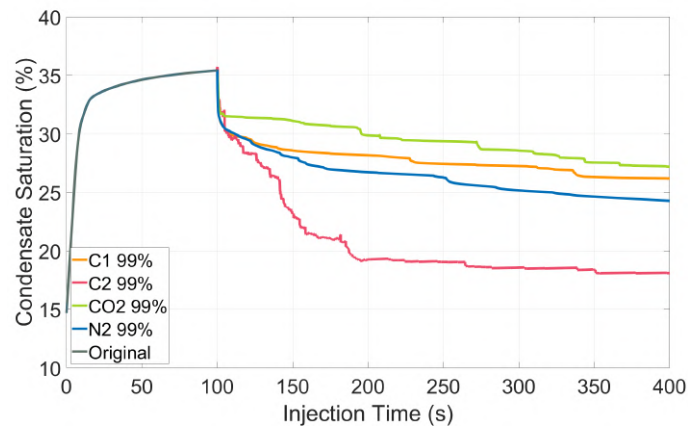


Figure 5.30: Condensate saturation during the injection at of gases with 99% molar concentration, $P=14.75$ MPa

At the pressure of 22MPa , just below the dew point pressure, C_2 and CO_2 produce almost identical effects on the accumulated condensate. Both reduced the liquid content faster and to a lower saturation than the other tested gases. C_1 also reduced significantly the condensate saturation, from 13.93% to 0.9%, while N_2 displayed the lowest capacity to recover condensate, leaving 3.16% of liquid in the network. Similar results were obtained with gas injection at the pressures of 21.5 and 21MPa . Even though the amount of accumulated condensate in the networks increased significantly, corresponding to 27.65% at 21.5MPa , and 32.06% at 21MPa , the injected gases cleared the liquid damage efficiently. This is a good indicative that, at high pressures, all tested gases could be used to support reservoir pressure and re-vaporize accumulated liquid. As the injection pressure is lowered below 20MPa , however, the ability of the gases to recover condensate is clearly reduced, as shown in Figures 5.28 to 5.30. The rate of liquid re-vaporization is progressively slowed down during the injection of all tested gases, indicating that more injected volume is required for the same volume of recovered condensate, as the reservoir becomes more depleted. These findings support the hypothesis that the timing for injection of gases in gas-condensate reservoirs is crucial for effective condensate recovery and gas flow improvement. As a complement to the analyses of condensate saturation reduction after gas injection, Figures 5.31, 5.32, 5.33 and 5.34 illustrate the molar content of C_1 , C_2 , CO_2 and N_2 , respectively, in the networks after the injection of the mixtures rich in the same components, at all tested pressures. In can be seen in these figures that, at the lowest tested pressure, all injected gases flow through a reduced portion of the porous medium, bypassing most of the deposited condensate.

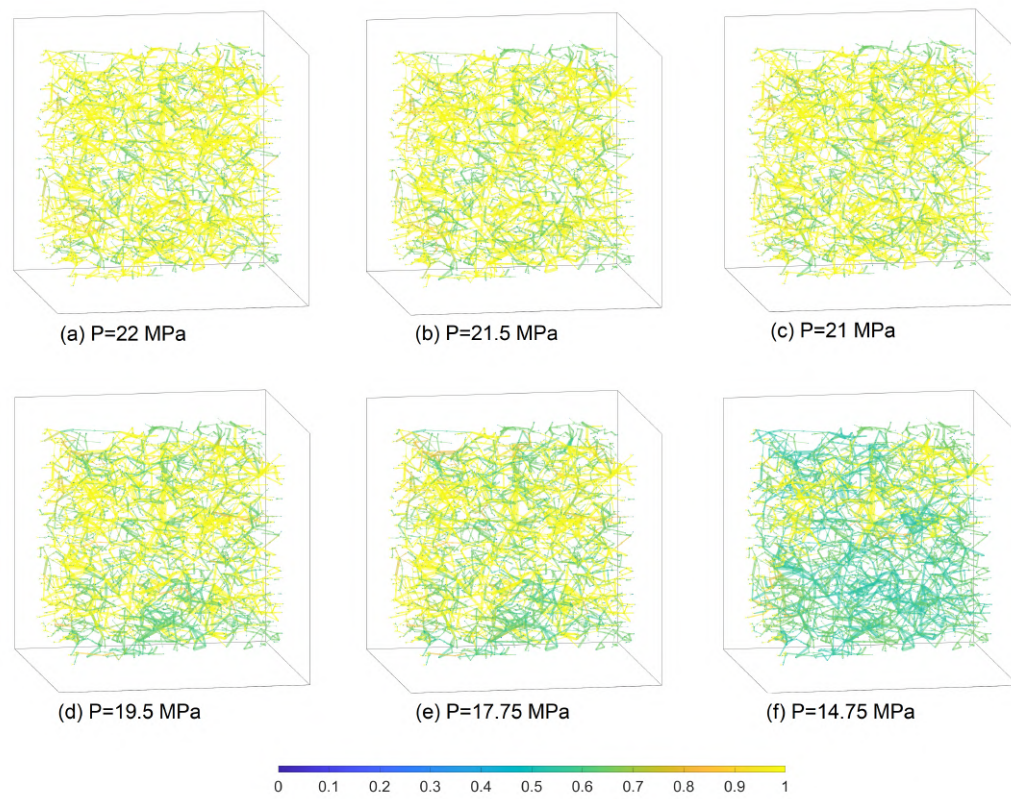


Figure 5.31: Molar content of C_1 in the pore-network after injection of the mixture containing 99% of C_1 .

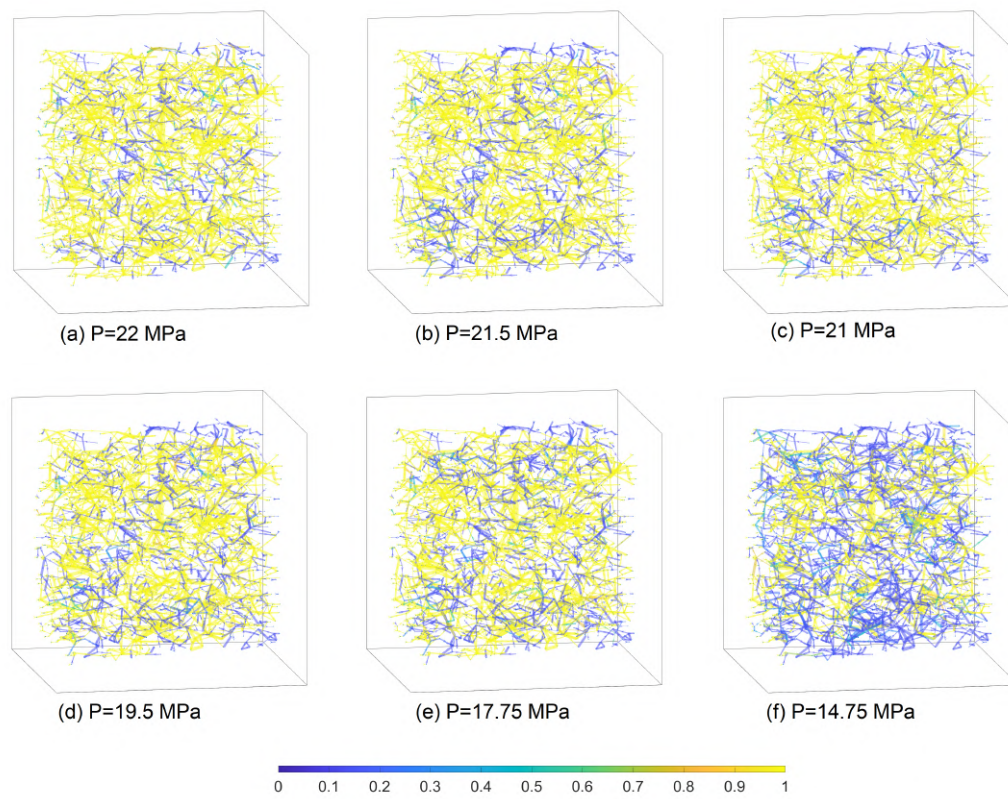


Figure 5.32: Molar content of C_2 in the pore-network after injection of the mixture containing 99% of C_2 .

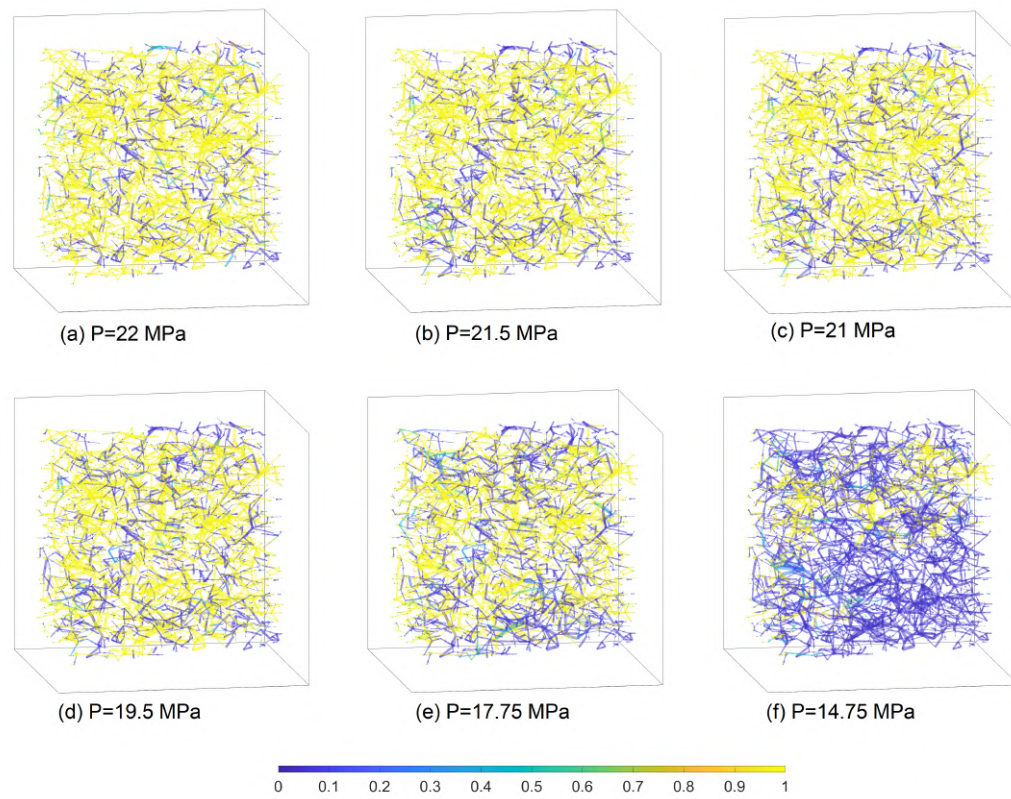


Figure 5.33: Molar content of CO_2 in the pore-network after injection of the mixture containing 99% of CO_2 .

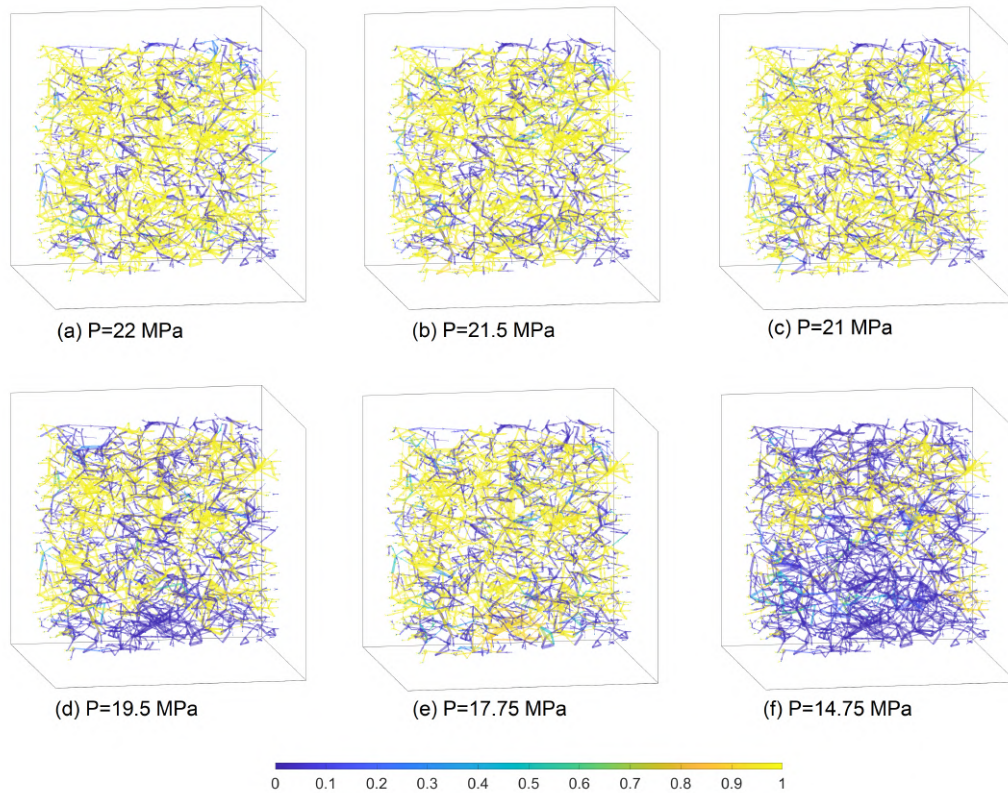


Figure 5.34: Molar content of N_2 in the pore-network after injection of the mixture containing 99% of N_2 .

The condensate saturation evolution during the injection of the gas mixtures containing 50% reservoir fluid and 50% C_1 , C_2 , CO_2 or N_2 is presented in Figures 5.35 to 5.40.

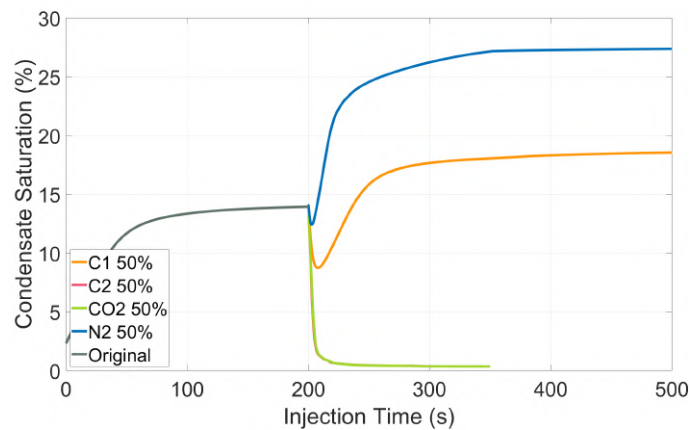


Figure 5.35: Condensate saturation during the injection of gases with 50% molar concentration, at P=22 MPa

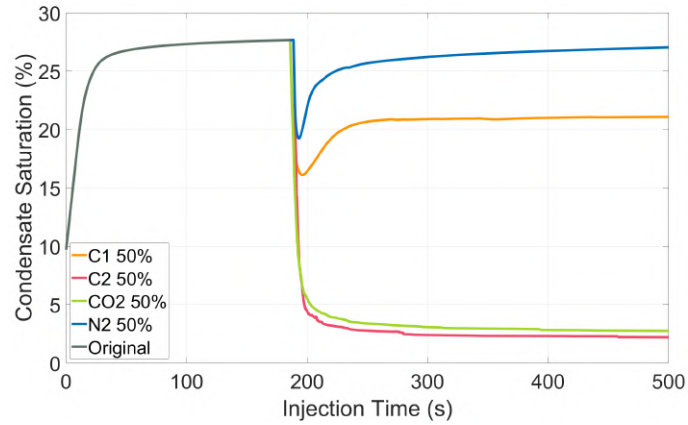


Figure 5.36: Condensate saturation during the injection of gases with 50% molar concentration, at $P=21.5$ MPa

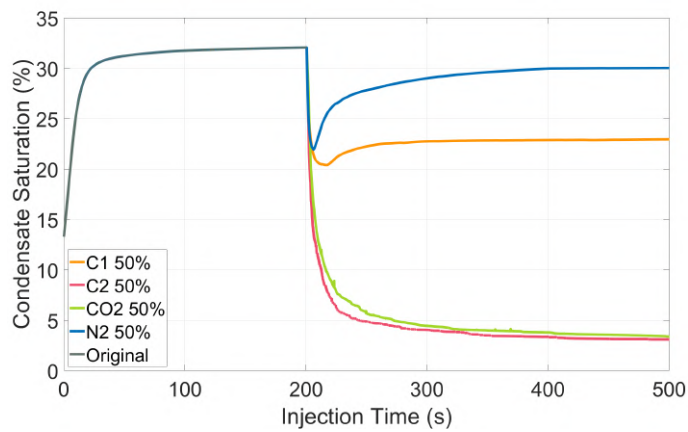


Figure 5.37: Condensate saturation during the injection at of gases with 50% molar concentration, $P=21$ MPa

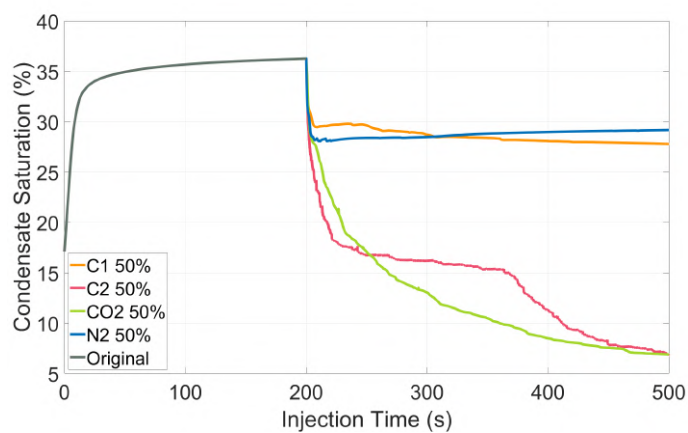


Figure 5.38: Condensate saturation during the injection at of gases with 50% molar concentration, $P=19.5$ MPa

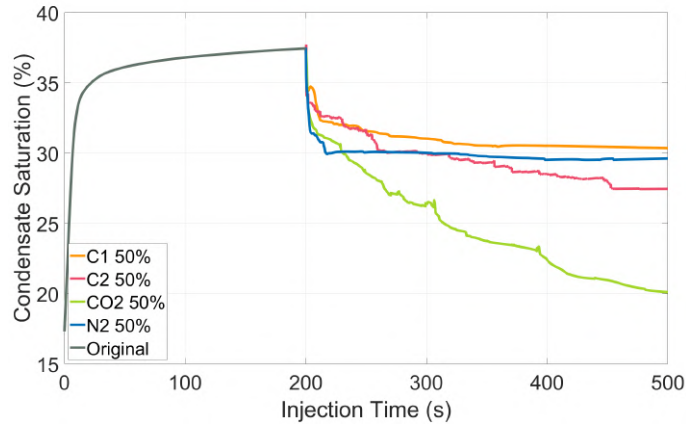


Figure 5.39: Condensate saturation during the injection of gases with 50% molar concentration, $P=17.75$ MPa

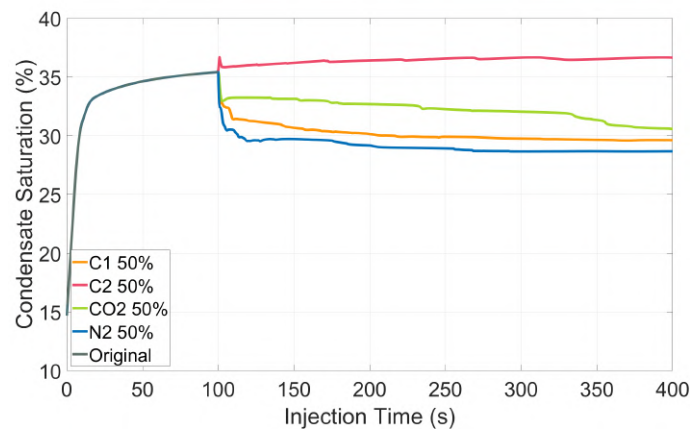


Figure 5.40: Condensate saturation during the injection of gases with 50% molar concentration, $P=14.75$ MPa

When injected mixed with the reservoir fluid, C_1 and N_2 were very ineffective to reduce the accumulated condensate in the porous medium, especially at high pressures. At the highest evaluated pressure of 22MPa , both gases even enlarged the liquid content in the networks, as seen in Figure 5.35. While the injection of the mixture rich in C_1 led to an increase of 33% in the liquid saturation in the network, the N_2 mixture almost doubled it. This result is related to the negative effect of C_1 and N_2 on the reservoir mixture's liquid dropout at high pressures, as shown in Figure 5.23. Yet, even at lower pressures, where the effects of C_1 and N_2 on condensate dropout become positive, very high liquid saturations remained in the networks after gas injection. This suggests that, to be successful as a condensate recovery method, the concentration of C_1 and N_2 flowing in porous media should be kept high, as the effects of dilution with the reservoir fluids can significantly

reduce their ability to re-vaporize liquid. On the other hand, the injection of diluted C_2 and CO_2 was notably effective at high pressures. To compare the different injection scenarios, Fig. 5.41 presents the liquid saturation reduction for all the cases tested. The efficiency of condensate recovery with the injection of C_1 and N_2 strongly depends on the dilution of the injected gas, as it is clear in Fig. 5.41 (a) and (d). Contrarily, the results obtained with the injection of the mixtures rich in C_2 and CO_2 showed very little sensitivity to the dilution from 99% to 50%, at high pressures. From 22MPa to 19.5MPa, the liquid reduction in the porous medium after injection at both molar fractions was very similar, as indicated in Figures 5.41(b) and (c). At lower pressures, however, the liquid recovery obtained with the injection of C_2 and CO_2 mixed with the reservoir fluid at a molar proportion of 50% declined rapidly. Interestingly, at the lowest tested pressure of $P = 14.75MPa$, less liquid was re-vaporized with the injection of C_2 and CO_2 than with the injection of C_1 and N_2 , reversing the trend observed at higher pressures.

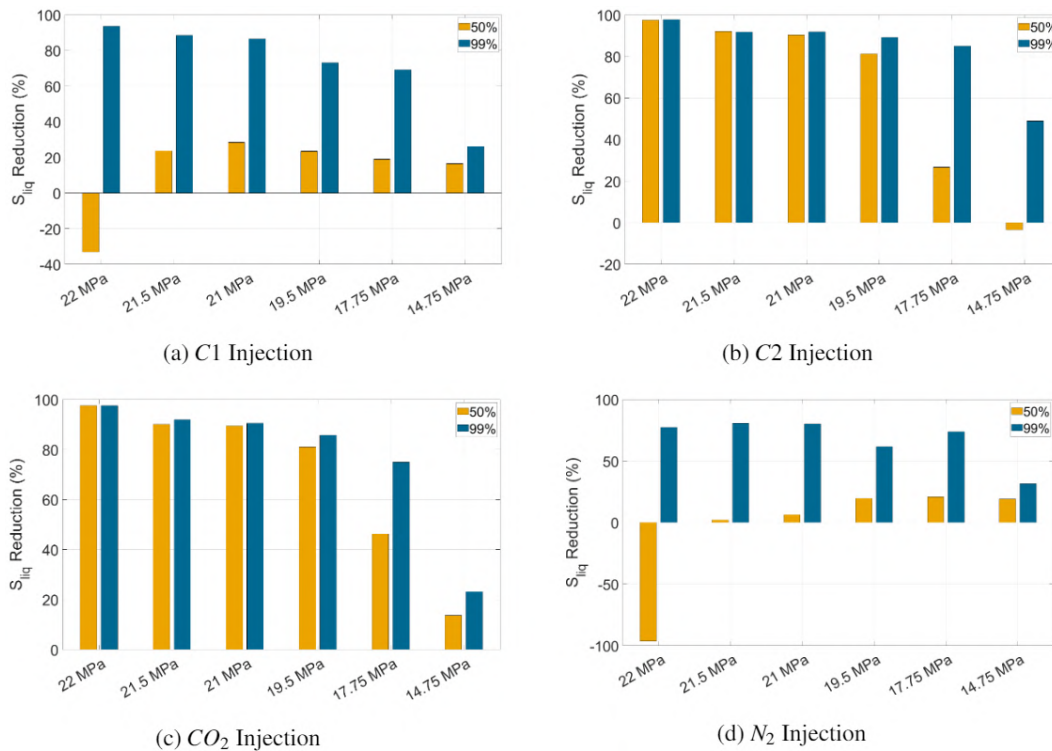


Figure 5.41: Condensate saturation reductions, for the different injected gases with molar concentrations of 50% (yellow) and 99% (blue).

5.2.2.5 Recovery of heavy components

Ideally, a gas mixture injected in a gas-condensate reservoir should be able to re-vaporize not only light, but also medium and heavy components accumulated in the porous medium during condensate banking. For this reason, the recoveries of the three heaviest components of the gas-condensate fluid used in this study, namely hexane, C_6 , decane, C_{10} and hexadecane, C_{16} , were quantified. These recoveries, presented in Figures 5.42 to 5.47, were calculated by evaluating the percentage decrease, in moles, of the contents of C_6 , C_{10} and C_{16} in the network after all tested gas injection scenarios.

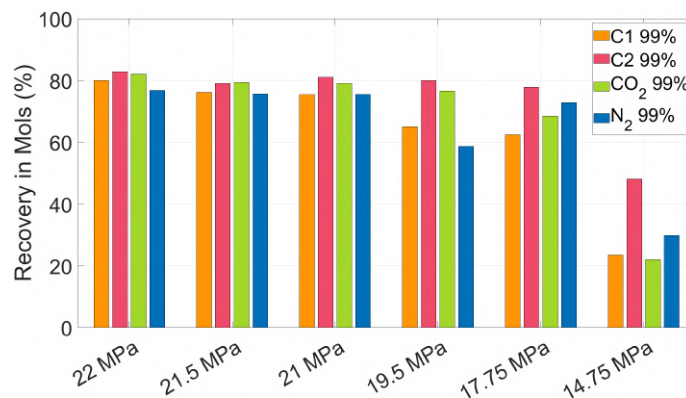


Figure 5.42: Hexane recovery after the injection of gases with 99% molar fraction of C_1 , C_2 , CO_2 or N_2 .

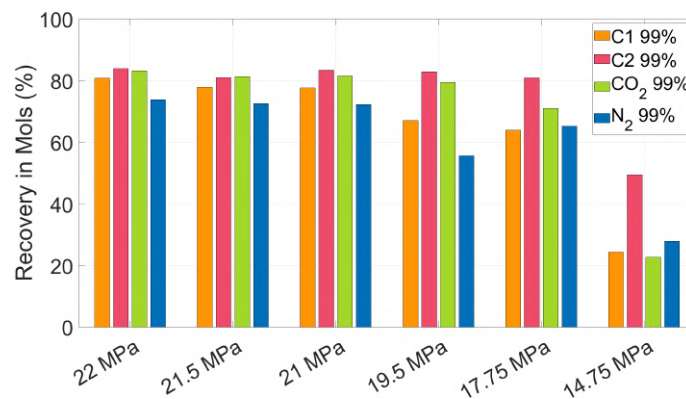


Figure 5.43: Decane recovery after the injection of gases with 99% molar fraction of C_1 , C_2 , CO_2 or N_2 .

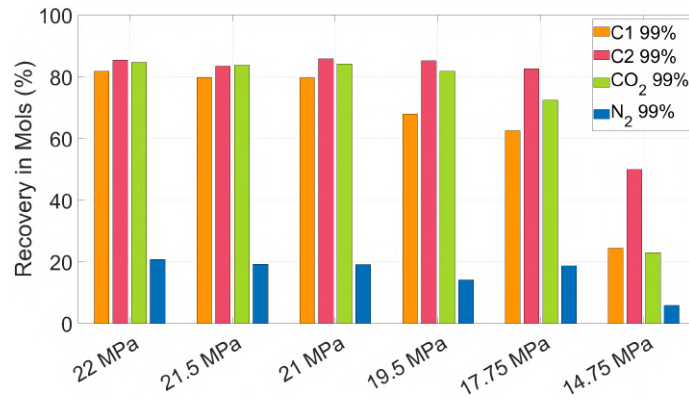


Figure 5.44: Hexadecane recovery after the injection of gases with 99% molar fraction of C_1 , C_2 , CO_2 or N_2 .

The results in Figures 5.42, 5.43 and 5.44 suggest that, when flowing at sufficiently high concentrations, C_1 , C_2 and CO_2 are able to recover the three heaviest components evenly. For these cases, the recoveries of each analyzed component can be directly related to the reduction in liquid saturation shown in Figure 5.41. During the injection of the mixture rich in N_2 , however, the recovery of hexadecane was considerably lower than the recoveries of hexane and decane. Therefore, in this case, during the re-vaporization of condensate, the remaining liquid in the porous medium becomes particularly rich in C_{16} , impeding its recovery. This indicates that, even when flowing at high concentrations, nitrogen may be unable to retrieve the heaviest components accumulated in gas-condensate reservoirs.

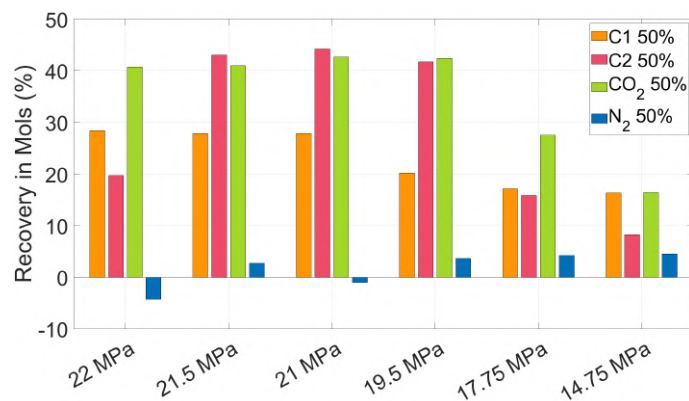


Figure 5.45: Hexane recovery after the injection of gases with 50% molar fraction of C_1 , C_2 , CO_2 or N_2 .

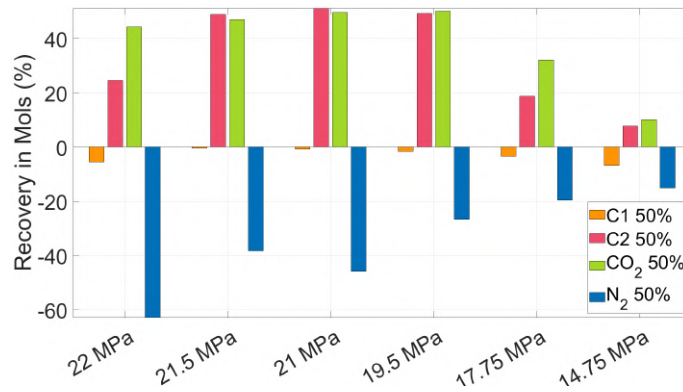


Figure 5.46: Decane recovery after the injection of gases with 50% molar fraction of C_1 , C_2 , CO_2 or N_2 .

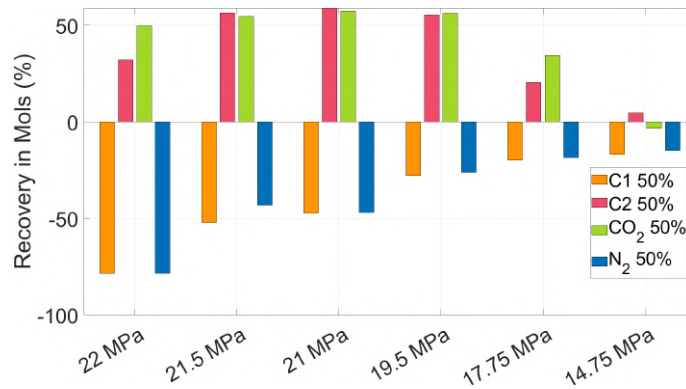


Figure 5.47: Hexadecane recovery after the injection of gases with 50% molar fraction of C_1 , C_2 , CO_2 or N_2 .

Mixing C_1 , C_2 , CO_2 or N_2 with the reservoir fluid at equal molar fractions before injection impacted significantly the recovery of heavy components, as shown in Figures 5.45, 5.46 and 5.47. The injection of the mixture with C_1 was able to recover a considerable amount of hexane, but could not recover decane nor hexadecane. In fact, when flowing mixed with the reservoir fluid, C_1 induced an increase in the fractions of C_{10} and C_{16} in the liquid accumulated in the porous medium. For this reason, even for the cases where the liquid saturation was lowered ($P \geq 21.5 MPa$), the amount of these components increased in the pore-space. A similar effect was observed in the flow of nitrogen mixed with the reservoir fluid. For these cases, however, the recovery of C_6 was insignificant, and large amounts of C_{10} and C_{16} migrated from the gas to the liquid phase. As an example of this effect, the molar contents of the phases contained in the networks at $P = 21.5 MPa$ were analyzed, before and after the injection of the nitrogen rich mixture. In this case, even though the liquid saturations before and after the gas injection are very similar, as shown in

Figures 5.36 and 5.41, the amount of C_{10} in the network increased 38%. This happened because the average fractions of decane in the gas and liquid phases changed from 2.14% and 5.76% to 0.93% and 16.78%, respectively. Similar effects took place at the other evaluated injection pressures, for the fractions of C_{10} and C_{16} . The injection of the gas mixtures with C_2 and CO_2 displayed overall the best results among the tested cases. With the exception of the CO_2 injection at the lowest tested pressure, CO_2 and C_2 were able to increase the recovery of the heavier components accumulated in the network, even after mixing with the reservoir fluid. These positive results are attributed not only to the reduction in liquid saturation in the porous medium, indicated in Figures 5.35 to 5.40 and 5.41, but also to a reduction in the heavier components molar fractions in the condensate. C_2 is particularly efficient in turning the composition of the accumulated condensate lighter. During the injection of the C_2 mixture at $P = 14.75\text{MPa}$, for instance, the recoveries of C_6 , C_{10} and C_{16} were positive, even considering that the liquid saturation increased slightly.

The results presented in Figures 5.42 to 5.47 reinforce the hypothesis arisen in section 5.2.2.4 that C_2 and CO_2 are more suitable candidates for condensate enhanced recovery than C_1 and N_2 . Injecting CO_2 and C_2 not only reduced more effectively the liquid content in the porous medium, but also, once mixed with the reservoir fluid, tended to shift favorably the phases contents, assisting the production of heavier components.

5.2.2.6

Gas relative permeability improvement

As a way of quantifying the gas flow improvement with gas injection, in this section, the gas relative permeabilities before and after the treatment were compared. As introduced in Section 2.3.2 and discussed throughout this thesis, gas relative permeabilities during gas-condensate flow depend not only on the phases saturations, but also on flowing velocity and interfacial tension. Nonetheless, the effects of these parameters on recovery have been neglected in the literature concerning gas injection in gas-condensate reservoirs.

Injecting gas on the reservoir after condensate accumulation affects not only the phases bulk properties, but also interfacial properties. Considering the potential impacts on relative permeability curves [117, 118, 106], these effects should be taken into account when choosing a gas mixture composition for injection in gas-condensate reservoirs. Figure 5.48 presents the interfacial tension for the mixtures containing 50% C_1 , C_2 , CO_2 or N_2 and 50% the reservoir fluid, in moles, calculated with the correlation proposed by Weinaug and Katz [29]. The results obtained with the correlation indicate that, for

all evaluated pressures, mixing C_1 or N_2 with the reservoir fluid leads to an increase in the interfacial tension between gas and condensate. C_2 , on the other hand, reduces the interfacial tension, while CO_2 has little effect on it.

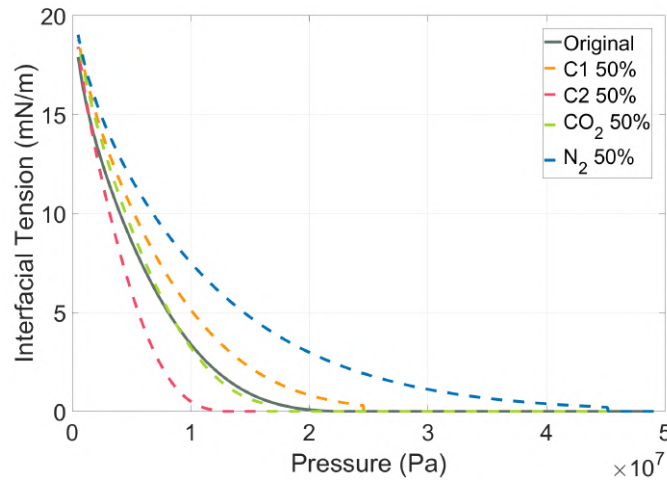


Figure 5.48: Calculated interfacial tension for mixtures of the reservoir fluid with C_1 , C_2 , CO_2 or N_2 .

Figures 5.49 and 5.50 present the gas relative permeabilities before and after gas injection. It is important to note that, in these figures, the liquid saturation is different for each case. For all tested scenarios, the injection of the mixtures enriched with C_2 or CO_2 led to an increase in the gas relative permeability. During the injection of the mixtures enriched with C_1 or N_2 , however, some conditions led to a negative effect on the gas relative permeability. The reduction in k_{rg} took place even for cases in which the gas saturation increased, as seen in Figure 5.50, for the C_1 injection at $P=21.5$ MPa, and N_2 injection at $17.75 \leq P \leq 21.5$ MPa. This outcome can be directly linked to the increase in interfacial tension stemmed from mixing C_1 and N_2 with the reservoir fluid, seen in Figure 5.48. It suggests that, while the injection of C_1 or N_2 can improve the gas flow, providing that the condensate saturation is substantially reduced, at a fixed condensate saturation, the gas flow may be impaired.

These results are particularly relevant considering that most field scale numerical studies neglect the possible effects of the injected gas composition on the micro-scale gas-condensate displacement and, consequently, on the relative permeability curves. With this oversight, estimated recoveries obtained with C_1 and, especially, N_2 injection in gas-condensate reservoirs [112, 113, 114] might have been overestimated. For this reason, further studies concerning the effects of interfacial tension alteration during gas injection for condensate enhanced recovery are highly recommended.

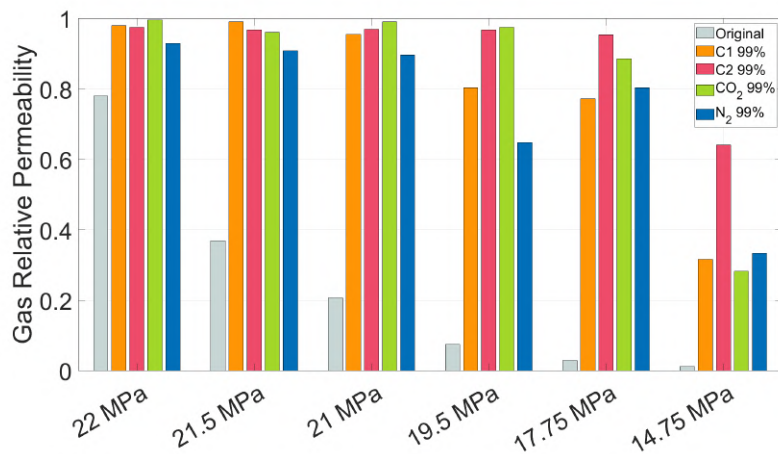


Figure 5.49: Gas relative permeabilities before and after the injection of the gas mixtures containing 99% of C_1 , C_2 , CO_2 or N_2 .

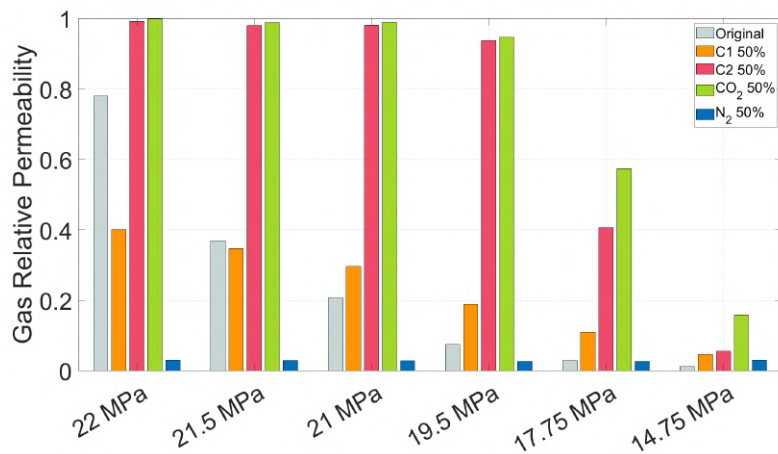


Figure 5.50: Gas relative permeabilities before and after the injection of the gas mixtures containing 50% of C_1 , C_2 , CO_2 or N_2 .

5.2.2.7 Discussion

The presented results emphasize the relevance of the injected gas composition and depletion stage in the reservoir for the success of gas injection as a condensate enhanced method. The findings suggest that CO_2 and C_2 are promising candidates for the studied method. Both gases displayed the overall highest liquid reduction potential, recovered efficiently heavy components and induced improvement in the gas-condensate relative permeability curves. Therefore, the use of CO_2 and C_2 , either pure or mixed with another compo-

nents due to cost and availability restrictions, should be further investigated for applications in partial pressure maintenance or huff-n-puff injection schemes. Pure C_1 injection also presented rather positive results and should be considered for injection aiming full or partial pressure maintenance. Relatively slow re-vaporization rate of condensate and potential increase in both interfacial tension and dew point pressure could, however, be a concern for its application. As for N_2 , given the feeble condensate re-vaporization tendency, low ability to recover heavy components and significant increase in interfacial tension, it does not emerge as a favorable candidate for gas injection in gas-condensate reservoirs. The relatively low injection costs [112] might be canceled out by early condensation, poor two-phase flow performance and entrapment of heavy components in the porous medium. The level of depletion in the reservoir previous to the gas injection also affected notably the results. For the evaluated gas-condensate fluid, performing gas injection below the pressure associated with the maximum liquid dropout in the reservoir could not enhance significantly the flow, for any tested gas composition. For this reason, the implementation of the EOR method in reservoirs at advanced stages of production may result in limited improvements and should be carefully planned.

The generalizability of the presented results is, however, bounded by some modeling limitations and particularities of the studied cases. First, the observed recoveries stemmed from mixing injected and reservoir fluids may depend upon the composition chosen to represent gas-condensate fluids. The extension of the analyses to different gas-condensate compositions could lead to variation in the results and, therefore, should be carried out. Additionally, porous media morphology can impact the performance of gas injection for condensate recovery, especially at low pressures, where the injected gas miscibility is limited. More heterogeneous media than the evaluated sandstone, for instance, may provide preferential paths for gas flow that deter the method's success, while very regular media could lead to increased recoveries. Finally, further studies should be performed to investigate the effects of injection rate on condensate recovery. Due to the tested gases different compressibilities, by imposing equal molar flow rates and pressures, we produced different flow velocities during the gas injection analyses, and that may influence the results. As for the model limitations, the used compositional pore network model does not take into account molecular diffusion. It has been pointed out in the literature [113, 119] that the effects of molecular diffusion during gas injection in gas-condensate reservoirs are not significant. Yet, for the analyses at low pressures, in which condensate recovery was low, implementing molecular diffusion in the model could produce more favorable results. Also, the implemented

compositional formulation assumes thermodynamic equilibrium in each pore at every simulation time step. For this reason, non-equilibrium effects in the gas-condensate flow are not taken into consideration. Further investigation should be carried out on gas injection parameters, e.g. high flow rates, that may call for the incorporation of non-equilibrium effects in the model. Lastly, the ability of the implemented phase equilibrium calculations to realistically represent gas mixtures with high contents of non hydrocarbon components should also be evaluated.

6 Conclusions

In the final Chapter of this thesis, the general conclusions drawn from the development of a pore-network model for gas-condensate flow are presented in Section 6.1. Then, the conclusions drawn from the studies regarding wettability alteration and gas injection as prospect enhanced gas and condensate recovery methods are presented in Sections 6.2 and 6.3, respectively. Finally, possible improvements for the current work are suggested in Section 6.4.

6.1 Pore-network model for gas-condensate flow

A new compositional dynamic pore-network model was presented to study gas and condensate coupled flow in porous media. The network comprised a 3D structure of constricted circular capillaries with hyperbolic profile. Gas and condensate conductances in the capillaries were calculated based on annular flow pattern, with liquid wetting capillary walls. Interruption of annular flow in the capillaries by the formation of condensate bridges was predicted, based on geometry and local liquid saturation. Once blocked, a capillary could be reopened if the pressure difference between its extremities exceeded a critical capillary pressure. Molar content and pressure distribution in the networks were calculated through the solution of a system of non-linear equations with Newton-Raphson method, while the phases saturations were determined with a PT flash.

The model was validated by comparing predictions of steady-state gas and condensate relative permeability curves with experimental data available in the literature. Results demonstrated that the model represented well the effect of condensate saturation, interfacial tension and velocity on gas-condensate flow. Predicted k_r curves for flow at two different interfacial tension values and three different gas velocities demonstrated reasonable quantitative agreement with experimental data. Also, analyses of the fraction of blocked capillaries in the networks, for different condensate saturations, indicated that the formation and retention of condensate slugs in pore throats could constitute the main mechanism related to condensate banking.

The model also proved to be capable of predicting the buildup of heavy

components in porous media during gas and condensate flow. For the $C1-nC4$ binary mixture used in the validation, at all tested injection conditions, an increase of n-butane molar fraction was verified in the network. For the cases at high S_l , a transition in behavior from gas-condensate to volatile oil was observed.

With the provided evidence of predictive capability, we believe that the proposed model has potential to produce tailored data to large-scale gas-condensate reservoir simulation, based on specific reservoir rock, fluid composition, and flow conditions. This could lead to more realistic production estimations and benefit gas-condensate fields development planning.

6.2

Pore-scale analysis of wettability alteration in gas-condensate reservoirs

The pore-network model presented in Chapter 4 was then expanded to evaluate gas-condensate flow under variable wetting conditions, in Section 5.2.1. The distinction between media with different wettabilities was established by implementing gas and condensate conductances based on filmwise condensation followed by annular flow in liquid-wet media, and dropwise condensation followed by slug flow in gas-wet media.

With the expanded model, the flow of a multi-component mixture that experiences retrograde condensation under typical reservoir conditions was analyzed in a sandstone based network with different degrees of wettability alteration. Relative permeabilities and improvement factors were calculated for several flow rates and pressures below the dew point, representing different conditions occurring in the near wellbore region.

Relative permeability curves for liquid and gas-wet media exhibited very different profiles, due to different flow patterns and fluid accumulation propensities. For all tested cases, except for $\theta = 90^\circ$, flow rate impacted positively on relative permeabilities, while interface tension impacted negatively. Improvement factors were calculated so that the gas flow performances in altered and unaltered wettability media were compared. Significant effects of contact angle, flow rate and depletion stage on IFs were identified. The dependency of improvement factors on flow conditions predicted by the model agreed qualitatively with experimental results reported in the literature, as higher interfacial tension values led to higher improvement factors. Also, for analogous contact angle and interfacial tension values, the results were quantitatively similar. For $\theta = 45^\circ$ and 60° , and low interfacial tension, the improvement factors for both experiments [84] and numerical modeling were in the range between 1 and 1.5. Contact angles closer to $\theta = 90^\circ$ led to higher improvement factors

in both gas and liquid-wet media. The impact of wettability alteration was more pronounced at lower pressures, in which higher interfacial tension and liquid saturation occur. For gas-wet media, low flow rates and high pressures could lead to $IF < 1$, which indicates gas flow impairment. These conditions, however, are not predominant in the near wellbore region.

Fluid phase behavior during depletion was also assessed with the pore-network model. In liquid-wet media, the tendency of condensate buildup led to the transition from gas-condensate to volatile-oil behavior, at the pressure associated with the maximum liquid dropout. This can impact long term gas productivity and should also be taken into account when designing a wettability alteration treatment for field application.

We believe that the presented model could serve as a fast and economical tool for the appraisal of wettability alteration as a condensate blockage mitigation method.

6.3

Pore-scale analysis of gas injection in gas-condensate reservoirs

Finally, the model presented in Chapter 4 was used to evaluate gas injection as a condensate enhanced recovery method. The effects of the injected gas composition and the injection pressure were investigated by quantifying liquid saturation reduction, heavy component recovery and the impact on gas relative permeabilities. During this study, the performances of injecting C_1 , C_2 , CO_2 or N_2 to recover the condensate accumulated in a sandstone based pore-network were compared.

The results indicated that gas injection can produce substantial flow improvement in damaged gas-condensate reservoirs, given that the injected gas composition and pressure for the treatment are adequately determined. Injecting C_2 or CO_2 produced the most favorable results among the tested gases, while C_1 exhibited moderate positive effects on flow and N_2 displayed overall a significantly worse performance for condensate recovery.

As a preliminary investigation of gas injection in gas-condensate reservoirs at the pore-scale, this work exposed how changing the phases bulk and interfacial properties can impact significantly the two-phase flow during condensate recovery and, consequently, the method's efficiency. Interfacial tension effects, often overlooked in the field literature, showed particularly relevance in gas flow performance after gas injection. By neglecting the potential negative effects of increase in interfacial tension during the injection of C_1 or N_2 , condensate recovery predictions obtained with reservoir-scale models may be overestimated.

6.4

Future work

Regarding the development of the pore-network model for gas-condensate flow, future work could encompass the implementation of wall roughness effects on condensate flow and the construction of pore-networks constituted by elements other than the currently used constricted circular capillaries. As noticed in the results presented in the Validation Section, condensate relative permeabilities were overestimated, and accounting for the effects of roughness and/or using pore elements with polygonal cross-section could reduce condensate mobility. Additionally to adopting angular cross-sections for the capillaries, adapting the model to use asymmetric capillaries could favor a better representation of real geological porous media. These alterations, on their turn, would generate the necessity of adapting the currently implemented snap-off criterion. More realistic predictions of gas-condensate flow in geologic porous media could also be obtained by including the presence of an aqueous phase in the networks prior to condensation.

Future work on the model adaptation to evaluate gas-condensate flow in porous media with altered wettability could involve devising a correlation to determine the contact-angle as a function of the system thermodynamic state. As observed experimentally [81], the condensate repellency strength of wettability modifiers devised for gas-condensate reservoirs is affected by the gas-condensate composition and interfacial tension. Therefore, modeling these effects could lead to more realistic estimates of how effectively altering the near wellbore region wettability could prevent condensate banking. Moreover, implementing a more gradual flow pattern transition between liquid and gas-wet states could improve the fidelity of flow analyses for near intermediate-wet conditions. Lastly, defining a minimum condensate saturation for slug formation in gas-wet media could also benefit the analyses of flow at low liquid saturations.

As for the analyses of gas injection as a potential EOR method, future work could encompass carrying out a more systematic pore-scale investigation of the parameters affecting condensate recovery with gas injection, as flow rate, gas-condensate fluid composition and porous media heterogeneity. With that, data for up-scaling pore-scale effects pertaining to particular gas injection scenarios could be generated for reservoir-scale modeling. This could lead to more realistic recovery estimations and benefit gas-condensate fields development planning.

Bibliography

- [1] PEDERSEN, K. S.; CHRISTENSEN, P. L. ; SHAIKH, J. A.. **Phase behavior of petroleum reservoir fluids**. CRC press, 2014.
- [2] COŞKUNER, G.. **Microvisual study of multiphase gas condensate flow in porous media**. *Transport in Porous Media*, 28(1):1–18, 7 1997.
- [3] DAWE, R. A.; GRATTONI, C. A.. **Fluid flow behaviour of gas-condensate and near-miscible fluids at the pore scale**. *Journal of Petroleum Science and Engineering*, 55(3-4):228–236, 2007.
- [4] JAMIOLAHMADY, M.; DANESH, A.; TEHRANI, D. H. ; DUNCAN, D. B.. **A mechanistic model of gas-condensate flow in pores**. *Transport in porous media*, 41(1):17–46, 2000.
- [5] DONG, H.. **Micro-CT imaging and pore network extraction**. PhD thesis, Department of Earth Science and Engineering, Imperial College London, 2008.
- [6] MOHAMMADI, S.; SORBIE, K.; DANESH, A.; PEDEN, J. ; OTHERS. **Pore-level modelling of gas-condensate flow through horizontal porous media**. In: SPE ANNUAL TECHNICAL CONFERENCE AND EXHIBITION. Society of Petroleum Engineers, 1990.
- [7] FANG, F.; FIROOZABADI, A.; ABBASZADEH, M.; RADKE, C. ; OTHERS. **A phenomenological modeling of critical condensate saturation**. In: SPE ANNUAL TECHNICAL CONFERENCE AND EXHIBITION. Society of Petroleum Engineers, 1996.
- [8] WANG, X.; MOHANTY, K.. **Critical condensate saturation in porous media**. *Journal of colloid and interface science*, 214(2):416–426, 1999.
- [9] WANG, X.; MOHANTY, K. K. ; OTHERS. **Pore-network model of flow in gas/condensate reservoirs**. *SPE Journal*, 5(04):426–434, 2000.
- [10] BUSTOS, C. I.; TOLEDO, P. G.. **Pore-level modeling of gas and condensate flow in two-and three-dimensional pore networks:**

- Pore size distribution effects on the relative permeability of gas and condensate. *Transport in Porous Media*, 53(3):281–315, 2003.
- [11] SANTOS, M.; CARVALHO, M.. **Pore network model for retrograde gas flow in porous media.** *Journal of Petroleum Science and Engineering*, 185:106635, 2020.
- [12] Imperial college london. perm - petroleum engineering rock mechanics group. **micro-ct images and networks: Sandstone s4.** <http://www.imperial.ac.uk/earth-science/research/research-groups/perm/research/pore-scale-modelling/micro-ct-images-and-networks/sandstone-s4/>, 2007. Accessed on 25/08/2020.
- [13] SAYED, M. A.; AL-MUNTASHERI, G. A. ; OTHERS. **Mitigation of the effects of condensate banking: a critical review.** *SPE Production & Operations*, 31(02):85–102, 2016.
- [14] GANIE, K.; IDRIS, A. K.; MOHSHIM, D. F.; SULAIMAN, W. R. W.; SAAID, I. M. ; MALIK, A. A.. **A review on the wettability alteration mechanism in condensate banking removal.** *Journal of Petroleum Science and Engineering*, 183:106431, 2019.
- [15] HASSAN, A. M.; MAHMOUD, M. A.; AL-MAJED, A. A.; AL-SHEHRI, D.; AL-NAKHLI, A. R. ; BATAWEEL, M. A.. **Gas production from gas condensate reservoirs using sustainable environmentally friendly chemicals.** *Sustainability*, 11(10):2838, 2019.
- [16] JAMIOLAHMADY, M.; DANESH, A.; TEHRANI, D. H. ; DUNCAN, D. B.. **Positive effect of flow velocity on gas–condensate relative permeability: network modelling and comparison with experimental results.** *Transport in Porous Media*, 52(2):159–183, 2003.
- [17] CHEN, H. L.; WILSON, S. D. ; MONGER-MCCLURE, T. G.. **Determination of relative permeability and recovery for north sea gas condensate reservoirs.** In: *SPE ANNUAL TECHNICAL CONFERENCE AND EXHIBITION.* Society of Petroleum Engineers, 1995.
- [18] HENDERSON, G. D.; DANESH, A.; TEHRANI, D. H.; AL-SHAIDI, S.; PEDEN, J. M. ; OTHERS. **Measurement and correlation of gas condensate relative permeability by the steady-state method.** *SPE Reservoir Evaluation & Engineering*, 1(02):134–140, 1998.

- [19] JAMIOLAHMADY, M.; DANESH, A.; HENDERSON, G.; TEHRANI, D. ; OTHERS. **Variations of gas-condensate relative permeability with production rate at near wellbore conditions: a general correlation.** In: OFFSHORE EUROPE. Society of Petroleum Engineers, 2003.
- [20] MOTT, R.; CABLE, A.; SPEARING, M. ; OTHERS. **Measurements and simulation of inertial and high capillary number flow phenomena in gas-condensate relative permeability.** In: SPE ANNUAL TECHNICAL CONFERENCE AND EXHIBITION. Society of Petroleum Engineers, 2000.
- [21] AL HARRASI, M.; GRATTONI, C.; FISHER, Q. ; AL-HINAI, S.. **Condensate displacement mechanisms in low permeability rocks.** In: PROCEEDINGS, p. 15. Society of Core Analysts, 2009.
- [22] NAGARAJAN, N.; HONARPOUR, M.; SAMPATH, K. ; MCMICHAEL, D.. **Comparison of gas-condensate relative permeability using live fluid vs. model fluids.** SCA2004-09, 2004.
- [23] BLUNT, M. J.; BIJELJIC, B.; DONG, H.; GHARBI, O.; IGLAUER, S.; MOSTAGHIMI, P.; PALUSZNY, A. ; PENTLAND, C.. **Pore-scale imaging and modelling.** *Advances in Water resources*, 51:197–216, 2013.
- [24] JOEKAR-NIASAR, V.; HASSANIZADEH, S.. **Analysis of fundamentals of two-phase flow in porous media using dynamic pore-network models: A review.** *Critical reviews in environmental science and technology*, 42(18):1895–1976, 2012.
- [25] PENG, D.-Y.; ROBINSON, D. B.. **A new two-constant equation of state.** *Industrial & Engineering Chemistry Fundamentals*, 15(1):59–64, 1976.
- [26] ROUSSENAC, B.. **Gas condensate well test analysis.** Master's thesis, Stanford University, Stanford, 6 2001.
- [27] VO, H. X.. **Composition variation during flow of gas-condensate wells.** A report submitted to the Department of energy resources engineering of Stanford University.—2010.—441 p, 2010.
- [28] LOHRENZ, J.; BRAY, B. G.; CLARK, C. R. ; OTHERS. **Calculating viscosities of reservoir fluids from their compositions.** *Journal of Petroleum Technology*, 16(10):1–171, 1964.

- [29] WEINAUG, C. F.; KATZ, D. L.. **Surface tensions of methane-propane mixtures.** *Industrial & Engineering Chemistry*, 35(2):239–246, 1943.
- [30] WU, S.; FIROOZABADI, A.. **Permanent alteration of porous media wettability from liquid-wetting to intermediate gas-wetting.** *Transport in Porous Media*, 85(1):189–213, 2010.
- [31] AFIDICK, D.; KACZOROWSKI, N.; BETTE, S. ; OTHERS. **Production performance of a retrograde gas reservoir: a case study of the arun field.** In: SPE ASIA PACIFIC OIL AND GAS CONFERENCE. Society of Petroleum Engineers, 1994.
- [32] BARNUM, R.; BRINKMAN, F.; RICHARDSON, T.; SPILLETTE, A. ; OTHERS. **Gas condensate reservoir behaviour: productivity and recovery reduction due to condensation.** In: SPE ANNUAL TECHNICAL CONFERENCE AND EXHIBITION. Society of Petroleum Engineers, 1995.
- [33] EL-BANBI, A. H.; MCCAIN JR, W.; SEMMELBECK, M. ; OTHERS. **Investigation of well productivity in gas-condensate reservoirs.** In: SPE/CERI GAS TECHNOLOGY SYMPOSIUM. Society of Petroleum Engineers, 2000.
- [34] HENDERSON, G. D.; DANESH, A.; TEHRANI, D. ; PEDEN, J.. **The effect of velocity and interfacial tension on relative permeability of gas condensate fluids in the wellbore region.** *Journal of Petroleum Science and Engineering*, 17(3-4):265–273, 1997.
- [35] ARMSTRONG, R. T.; MCCLURE, J. E.; BERRILL, M. A.; RÜCKER, M.; SCHLÜTER, S. ; BERG, S.. **Beyond darcy's law: The role of phase topology and ganglion dynamics for two-fluid flow.** *Physical Review E*, 94(4):043113, 2016.
- [36] HENDERSON, G. D.; DANESH, A.; TEHRANI, D.; AL-SHAIDI, S.; PEDEN, J. ; OTHERS. **Measurement and correlation of gas condensate relative permeability by the steady-state method.** *SPE Reservoir Evaluation & Engineering*, 1(02):134–140, 1998.
- [37] BLOM, S.; HAGOORT, J. ; OTHERS. **How to include the capillary number in gas condensate relative permeability functions?** In: SPE ANNUAL TECHNICAL CONFERENCE AND EXHIBITION. Society of Petroleum Engineers, 1998.

- [38] COATS, K. H.; OTHERS. **An equation of state compositional model.** Society of Petroleum Engineers Journal, 20(05):363–376, 1980.
- [39] BROOKS, R. H.; COREY, A. T.. **Properties of porous media affecting fluid flow.** Journal of the irrigation and drainage division, 92(2):61–88, 1966.
- [40] WHITSON, C. H.; FEVANG, Ø.. **Generalized pseudopressure well treatment in reservoir simulation.** In: PROC. IBC CONFERENCE ON OPTIMISATION OF GAS CONDENSATE FIELDS, p. 26–27, 1997.
- [41] POPE, G.; WU, W.; NARAYANASWAMY, G.; DELSHAD, M.; SHARMA, M.; WANG, P. ; OTHERS. **Modeling relative permeability effects in gas-condensate reservoirs with a new trapping model.** SPE Reservoir Evaluation & Engineering, 3(02):171–178, 2000.
- [42] HENDERSON, G. D.; DANESH, A. ; TEHRANI, D.. **Effect of positive rate sensitivity and inertia on gas condensate permeability at high velocity.** Petroleum Geoscience, 7(1):45–50, 2001.
- [43] WHITSON, C. H.; FEVANG, Ø. ; SÆVAREID, A.. **Gas condensate relative permeability for well calculations.** Transport in porous media, 52(2):279–311, 2003.
- [44] JAMIOLAHMADY, M.; DANESH, A.; TEHRANI, D. ; SOHRABI, M.. **Variations of gas/condensate relative permeability with production rate at near-wellbore conditions: A general correlation.** SPE Reservoir Evaluation & Engineering, 9(06):688–697, 2006.
- [45] JAMIOLAHMADY, M.; SOHRABI, M.; IRELAND, S. ; GHAHRI, P.. **A generalized correlation for predicting gas–condensate relative permeability at near wellbore conditions.** Journal of Petroleum Science and Engineering, 66(3-4):98–110, 2009.
- [46] JAMIOLAHMADY, M.; SOHRABI, M.; IRELAND, S. ; OTHERS. **Gas-condensate relative permeabilities in propped-fracture porous media: coupling vs. inertia.** SPE Journal, 15(01):208–222, 2010.
- [47] GHOLAMPOUR, F.; MAHDIYAR, H.. **A new correlation for relative permeability in gas-condensate reservoirs.** Journal of Petroleum Science and Engineering, 172:831–838, 2019.

- [48] MAHDAVIARA, M.; MENAD, N. A.; GHAZANFARI, M. H. ; HEMMATI-SARAPARDEH, A.. **Modeling relative permeability of gas condensate reservoirs: Advanced computational frameworks.** *Journal of Petroleum Science and Engineering*, 189:106929, 2020.
- [49] KALLA, S.; LEONARDI, S. A.; BERRY, D. W.; POORE, L. D.; SAHOO, H.; KUDVA, R. A. ; BRAUN, E. M.. **Factors that affect gas-condensate relative permeability.** *SPE Reservoir Evaluation & Engineering*, 18(01):5–10, 2015.
- [50] BULTREYS, T.; DE BOEVER, W. ; CNUUDE, V.. **Imaging and image-based fluid transport modeling at the pore scale in geological materials: A practical introduction to the current state-of-the-art.** *Earth-Science Reviews*, 155:93–128, 2016.
- [51] RAEINI, A. Q.; BIJELJIC, B. ; BLUNT, M. J.. **Generalized network modeling of capillary-dominated two-phase flow.** *Physical Review E*, 97(2):023308, 2018.
- [52] JIANG, Z.; VAN DIJKE, M.; WU, K.; COUPLES, G. D.; SORBIE, K. S. ; MA, J.. **Stochastic pore network generation from 3d rock images.** *Transport in porous media*, 94(2):571–593, 2012.
- [53] HYMAN, J. D.; WINTER, C. L.. **Stochastic generation of explicit pore structures by thresholding gaussian random fields.** *Journal of Computational Physics*, 277:16–31, 2014.
- [54] WANG, X.; SHENG, J. J.. **Multi-scaled pore network modeling of gas-water flow in shale formations.** *Journal of Petroleum Science and Engineering*, 177:899–908, 2019.
- [55] BAYCHEV, T. G.; JIVKOV, A. P.; RABBANI, A.; RAEINI, A. Q.; XIONG, Q.; LOWE, T. ; WITHERS, P. J.. **Reliability of algorithms interpreting topological and geometric properties of porous media for pore network modelling.** *Transport in Porous Media*, 128(1):271–301, 2019.
- [56] RYAZANOV, A. V.; VAN DIJKE, M. I. J. ; SORBIE, K. S.. **Two-phase pore-network modelling: existence of oil layers during water invasion.** *Transport in Porous Media*, 80(1):79–99, 2009.
- [57] JOEKAR-NIASAR, V.; HASSANIZADEH, S. M.. **Effect of fluids properties on non-equilibrium capillarity effects: Dynamic pore-**

- network modeling. *International Journal of Multiphase Flow*, 37(2):198–214, 2011.
- [58] VALAVANIDES, M.; CONSTANTINIDES, G. ; PAYATAKES, A.. **Mechanistic model of steady-state two-phase flow in porous media based on ganglion dynamics.** *Transport in Porous Media*, 30(3):267–299, 1998.
- [59] AL-GHARBI, M. S.; BLUNT, M. J.. **Dynamic network modeling of two-phase drainage in porous media.** *Physical Review E*, 71(1):016308, 2005.
- [60] BLUNT, M. J.. **Flow in porous media—pore-network models and multiphase flow.** *Current opinion in colloid & interface science*, 6(3):197–207, 2001.
- [61] LI, K.; FIROOZABADI, A. ; OTHERS. **Phenomenological modeling of critical condensate saturation and relative permeabilities in gas/condensate systems.** *Spe Journal*, 5(02):138–147, 2000.
- [62] BLUNT, M. J.; OTHERS. **Effects of heterogeneity and wetting on relative permeability using pore level modeling.** *SPE journal*, 2(01):70–87, 1997.
- [63] HUGHES, R. G.; BLUNT, M. J.. **Pore scale modeling of rate effects in imbibition.** *Transport in Porous Media*, 40(3):295–322, 2000.
- [64] MOMENI, A.; DADVAR, M.; HEKMATZADEH, M. ; DABIR, B.. **3d pore network modeling and simulation for dynamic displacement of gas and condensate in wellbore region.** *International Journal of Multiphase Flow*, 97:147–156, 2017.
- [65] COLLINS, D.; NGHIEM, L.; LI, Y.; GRABONSTOTTER, J. ; OTHERS. **An efficient approach to adaptive-implicit compositional simulation with an equation of state.** *SPE reservoir engineering*, 7(02):259–264, 1992.
- [66] SOCHI, T.. **Newtonian flow in converging-diverging capillaries.** *International Journal of Modeling, Simulation, and Scientific Computing*, 4(03):1350011, 2013.
- [67] BERESNEV, I. A.; LI, W. ; VIGIL, R. D.. **Condition for break-up of non-wetting fluids in sinusoidally constricted capillary channels.** *Transport in porous media*, 80(3):581, 2009.

- [68] WILSON, G. M.. **A modified redlich-kwong equation of state, application to general physical data calculations.** In: 65TH NATIONAL AICHE MEETING, CLEVELAND, OH, volumen 15, 1969.
- [69] MICHELSEN, M. L.. **The isothermal flash problem. part i. stability.** Fluid phase equilibria, 9(1):1–19, 1982.
- [70] REIS, P.; CARVALHO, M.. **Pore-scale compositional modeling of gas-condensate flow: Effects of interfacial tension and flow velocity on relative permeability.** Journal of Petroleum Science and Engineering, p. 108454, 2021.
- [71] REIS, P. K.; CARVALHO, M. S.. **Pore-scale analysis of condensate blockage mitigation by wettability alteration.** Energies, 13(18):4673, 2020.
- [72] KEWEN, L.; ABBAS, F. ; OTHERS. **Experimental study of wettability alteration to preferential gas-wetting in porous media and its effects.** SPE Reservoir Evaluation & Engineering, 3(02):139–149, 2000.
- [73] ALI, N. E. C.; ZOGHBI, B.; FAHES, M.; NASRABADI, H. ; RETNANTO, A.. **The impact of near-wellbore wettability on the production of gas and condensate: Insights from experiments and simulations.** Journal of Petroleum Science and Engineering, 175:215–223, 2019.
- [74] FRANCO-AGUIRRE, M.; ZABALA, R. D.; LOPERA, S. H.; FRANCO, C. A. ; CORTÉS, F. B.. **Interaction of anionic surfactant-nanoparticles for gas-wettability alteration of sandstone in tight gas-condensate reservoirs.** Journal of Natural Gas Science and Engineering, 51:53–64, 2018.
- [75] LI, K.; LIU, Y.; ZHENG, H.; HUANG, G. ; LI, G.. **Enhanced gas-condensate production by wettability alteration to gas wetness.** Journal of Petroleum Science and Engineering, 78(2):505–509, 2011.
- [76] GAHROOEI, H. R. E.; GHAZANFARI, M. H.. **Toward a hydrocarbon-based chemical for wettability alteration of reservoir rocks to gas wetting condition: Implications to gas condensate reservoirs.** Journal of Molecular Liquids, 248:100–111, 2017.
- [77] HOSEINPOUR, S.-A.; MADHI, M.; NOROUZI, H.; SOULGANI, B. S. ; MOHAMMADI, A. H.. **Condensate blockage alleviation around gas-condensate producing wells using wettability alteration.** Journal of Natural Gas Science and Engineering, 62:214–223, 2019.

- [78] NOH, M. H.; FIROOZABADI, A. ; OTHERS. **Wettability alteration in gas-condensate reservoirs to mitigate well deliverability loss by water blocking.** SPE Reservoir Evaluation & Engineering, 11(04):676–685, 2008.
- [79] FAHIMPOUR, J.; JAMIOLAHMADY, M. ; OTHERS. **Optimization of fluorinated wettability modifiers for gas/condensate carbonate reservoirs.** SPE Journal, 20(04):729–742, 2015.
- [80] TANG, G.-Q.; FIROOZABADI, A.. **Wettability alteration to intermediate gas-wetting in porous media at elevated temperatures.** Transport in Porous Media, 52(2):185–211, 2003.
- [81] FAHIMPOUR, J.; JAMIOLAHMADY, M.. **Impact of gas–condensate composition and interfacial tension on oil-repellency strength of wettability modifiers.** Energy & fuels, 28(11):6714–6722, 2014.
- [82] WANG, Y.; JIN, J.; MA, L.; LI, L. ; ZHAO, X.. **Influence of wettability alteration to preferential gas-wetting on displacement efficiency at elevated temperatures.** Journal of Dispersion Science and Technology, 36(9):1274–1281, 2015.
- [83] FAHES, M. M.; FIROOZABADI, A. ; OTHERS. **Wettability alteration to intermediate gas-wetting in gas-condensate reservoirs at high temperatures.** SPE Journal, 12(04):397–407, 2007.
- [84] FAHIMPOUR, J.; JAMIOLAHMADY, M. ; OTHERS. **An improved understanding of performance of wettability alteration for condensate banking removal under steady-state flow conditions.** In: ABU DHABI INTERNATIONAL PETROLEUM EXHIBITION AND CONFERENCE. Society of Petroleum Engineers, 2015.
- [85] KUMAR, V.; POPE, G. A.; SHARMA, M. M. ; OTHERS. **Improving the gas and condensate relative permeability using chemical treatments.** In: SPE GAS TECHNOLOGY SYMPOSIUM. Society of Petroleum Engineers, 2006.
- [86] BANG, V. S. S.; POPE, G. A.; SHARMA, M. M.; BARAN JR, J. R. ; OTHERS. **Development of a successful chemical treatment for gas wells with liquid blocking.** In: SPE ANNUAL TECHNICAL CONFERENCE AND EXHIBITION. Society of Petroleum Engineers, 2009.
- [87] BANG, V. S. S.; POPE, G.; SHARMA, M. M.; BARAN, J.; AHMADI, M. ; OTHERS. **A new solution to restore productivity of gas wells**

- with condensate and water blocks. *SPE Reservoir Evaluation & Engineering*, 13(02):323–331, 2010.
- [88] FANG, C.; STEINBRENNER, J. E.; WANG, F.-M. ; GOODSON, K. E.. **Impact of wall hydrophobicity on condensation flow and heat transfer in silicon microchannels.** *Journal of Micromechanics and Microengineering*, 20(4):045018, 2010.
- [89] CHEN, Y.; CHENG, P.. **Condensation of steam in silicon microchannels.** *International Communications in Heat and Mass Transfer*, 32(1-2):175–183, 2005.
- [90] CUBAUD, T.; ULMANELLA, U. ; HO, C.-M.. **Two-phase flow in microchannels with surface modifications.** *Fluid Dynamics Research*, 38(11):772, 2006.
- [91] WU, T.; DJILALI, N.. **Experimental investigation of water droplet emergence in a model polymer electrolyte membrane fuel cell microchannel.** *Journal of Power Sources*, 208:248–256, 2012.
- [92] SANTOS, R. M.; KAWAJI, M.. **Developments on wetting effects in microfluidic slug flow.** *Chemical Engineering Communications*, 199(12):1626–1641, 2012.
- [93] KAWAHARA, A.; CHUNG, P.-Y. ; KAWAJI, M.. **Investigation of two-phase flow pattern, void fraction and pressure drop in a microchannel.** *International journal of multiphase flow*, 28(9):1411–1435, 2002.
- [94] CHUNG, P.-Y.; KAWAJI, M.. **The effect of channel diameter on adiabatic two-phase flow characteristics in microchannels.** *International journal of multiphase flow*, 30(7-8):735–761, 2004.
- [95] KAWAJI, M.; CHUNG, P.-Y.. **Adiabatic gas–liquid flow in microchannels.** *Microscale Thermophysical Engineering*, 8(3):239–257, 2004.
- [96] KASHID, M. N.; AGAR, D. W.. **Hydrodynamics of liquid–liquid slug flow capillary microreactor: flow regimes, slug size and pressure drop.** *Chemical Engineering Journal*, 131(1-3):1–13, 2007.
- [97] FEVANG, Ø.; WHITSON, C. ; OTHERS. **Modeling gas-condensate well deliverability.** *SPE Reservoir Engineering*, 11(04):221–230, 1996.

- [98] ZHANG, S.; JIANG, G.-C.; WANG, L.; QING, W.; GUO, H.-T.; TANG, X.-G.; BAI, D.-G.. **Wettability alteration to intermediate gas-wetting in low-permeability gas-condensate reservoirs**. *Journal of Petroleum Exploration and Production Technology*, 4(3):301–308, 2014.
- [99] AL-ANAZI, H. A.; XIAO, J.; AL-EIDAN, A. A.; BUHIDMA, I. M.; AHMED, M. S.; AL-FAIFI, M.; ASSIRI, W. J. ; OTHERS. **Gas productivity enhancement by wettability alteration of gas-condensate reservoirs**. In: EUROPEAN FORMATION DAMAGE CONFERENCE. Society of Petroleum Engineers, 2007.
- [100] GILANI, S. F. H.; SHARMA, M. M.; TORRES, D. E.; AHMADI, M.; POPE, G. A.; LINNEMEYER, H. C. ; OTHERS. **Correlating wettability alteration with changes in gas relative permeability in gas condensate/volatile oil reservoirs**. In: SPE INTERNATIONAL SYMPOSIUM ON OILFIELD CHEMISTRY. Society of Petroleum Engineers, 2011.
- [101] KARANDISH, G.; RAHIMPOUR, M.; SHARIFZADEH, S. ; DADKHAH, A.. **Wettability alteration in gas-condensate carbonate reservoir using anionic fluorinated treatment**. *Chemical Engineering Research and Design*, 93:554–564, 2015.
- [102] LUO, K.; LI, S.; ZHENG, X.; CHEN, G.; DAI, Z.; LIU, N. ; OTHERS. **Experimental investigation into revaporization of retrograde condensate by lean gas injection**. In: SPE ASIA PACIFIC OIL AND GAS CONFERENCE AND EXHIBITION. Society of Petroleum Engineers, 2001.
- [103] AHMED, T.; EVANS, J.; KWAN, R.; VIVIAN, T. ; OTHERS. **Wellbore liquid blockage in gas-condensate reservoirs**. In: SPE EASTERN REGIONAL MEETING. Society of Petroleum Engineers, 1998.
- [104] AL-ANAZI, H. A.; SHARMA, M. M.; POPE, G. A. ; OTHERS. **Revaporization of condensate with methane flood**. In: SPE ANNUAL TECHNICAL CONFERENCE AND EXHIBITION. Society of Petroleum Engineers, 2004.
- [105] GACHUZ-MURO, H.; GONZALEZ VALTIERRA, B. E.; LUNA, E. E.; AGUILAR LOPEZ, B. ; OTHERS. **Laboratory tests with co₂, n₂ and lean natural gas in a naturally fractured gas-condensate reservoir under hp/ht conditions**. In: SPE ENHANCED OIL RECOVERY CONFERENCE. Society of Petroleum Engineers, 2011.

- [106] AL-ABRI, A.; SIDIQ, H. ; AMIN, R.. **Mobility ratio, relative permeability and sweep efficiency of supercritical co₂ and methane injection to enhance natural gas and condensate recovery: Core-flooding experimentation.** *Journal of Natural Gas Science and Engineering*, 9:166–171, 2012.
- [107] SHENG, J. J.. **Increase liquid oil production by huff-n-puff of produced gas in shale gas condensate reservoirs.** *Journal of Unconventional Oil and Gas Resources*, 11:19–26, 2015.
- [108] MENG, X.; SHENG, J. J. ; OTHERS. **Experimental study on re-vaporization mechanism of huff-n-puff gas injection to enhance condensate recovery in shale gas condensate reservoirs.** In: *SPE IMPROVED OIL RECOVERY CONFERENCE*. Society of Petroleum Engineers, 2016.
- [109] SHARMA, S.; SHENG, J. J. ; SHEN, Z.. **A comparative experimental study of huff-n-puff gas injection and surfactant treatment in shale gas-condensate cores.** *Energy & fuels*, 32(9):9121–9131, 2018.
- [110] MENG, X.; MENG, Z.; MA, J.; WANG, T. ; OTHERS. **Performance evaluation of co₂ huff-n-puff gas injection in shale gas condensate reservoirs.** *Energies*, 12(1):1–18, 2018.
- [111] MAROKANE, D.; LOGMO-NGOG, A.; SARKAR, R. ; OTHERS. **Applicability of timely gas injection in gas condensate fields to improve well productivity.** In: *SPE/DOE IMPROVED OIL RECOVERY SYMPOSIUM*. Society of Petroleum Engineers, 2002.
- [112] LINDERMAN, J. T.; AL-JENAIBI, F. S.; GHORI, S. G.; PUTNEY, K.; LAWRENCE, J.; GALLAT, M.; HOHENSEE, K. ; OTHERS. **Feasibility study of substituting nitrogen for hydrocarbon in a gas recycle condensate reservoir.** In: *ABU DHABI INTERNATIONAL PETROLEUM EXHIBITION AND CONFERENCE*. Society of Petroleum Engineers, 2008.
- [113] TAHERI, A.; HOIER, L.; TORSÆTER, O. ; OTHERS. **Miscible and immiscible gas injection for enhancing of condensate recovery in fractured gas condensate reservoirs.** In: *EAGE ANNUAL CONFERENCE & EXHIBITION INCORPORATING SPE EUROPEC*. Society of Petroleum Engineers, 2013.

- [114] FATH, A. H.; POURANFARD, A.-R.; PARANDVAR, R. ; POURHADI, S.. **An investigation of different gas injection scenarios as enhanced condensate recovery method in a naturally fractured gas-condensate reservoir.** *Petroleum Science and Technology*, 34(3):295–301, 2016.
- [115] SHARMA, S.; SHENG, J. J.. **A comparative study of huff-n-puff gas and solvent injection in a shale gas condensate core.** *Journal of Natural Gas Science and Engineering*, 38:549–565, 2017.
- [116] ZHANG, A.; FAN, Z. ; ZHAO, L.. **An investigation on phase behaviors and displacement mechanisms of gas injection in gas condensate reservoir.** *Fuel*, 268:117373, 2020.
- [117] AL-ABRI, A.; AMIN, R.. **Phase behaviour, fluid properties and recovery efficiency of immiscible and miscible condensate displacements by scco 2 injection: experimental investigation.** *Transport in porous media*, 85(3):743–756, 2010.
- [118] AL-ABRI, A.; AMIN, R.. **Effect of hydrocarbon and non-hydrocarbon gas injection on the interfacial tension of a gas condensate system.** *Chemical engineering & technology*, 34(1):127–133, 2011.
- [119] SHTEPANI, E.; OTHERS. **Co2 sequestration in depleted gas/condensate reservoirs.** In: *SPE ANNUAL TECHNICAL CONFERENCE AND EXHIBITION*. Society of Petroleum Engineers, 2006.